Coupling Single Molecules to Cryogenic Optical Fibre Microcavities

Kyle D. Major

Department of Physics

Imperial College London

Report submitted in partial fulfillment

of the requirements of the degree of Doctor of Philosophy

FEBRUARY 2016

ABSTRACT

Placing single emitters inside optical cavities provides a way of drastically modifying their interaction with the electric field. Such systems can be used to test our fundamental understanding of quantum electrodynamics and to develop devices that exploit this new found knowledge.

This thesis describes work towards coupling single dye molecules to optical fibre microcavities at cryogenic temperatures. I present the design of an oven growth chamber and develop a method to grow cosublimated crystals of anthracene doped with dibenzoterrylene. I then describe the characterisation of these samples using a confocal microscope setup both at ambient and cryogenic temperatures.

The samples grown show bright, stable, single emitters in a defined orientation in the anthracene crystals. By varying the growth parameters of the homebuilt crystal growing chamber, we can control the density of dibenzoterrylene molecules and grow at an optimum density to use these crystals in conjunction with optical fibre microcavities.

I show how optical fibre microcavities have been developed that can be cooled to the liquid helium temperatures required to take advantage of the lifetime-limited emission from single dibenzoterrylene molecules, that only occurs below 4K. I also present cavity quantum electrodynamic simulations of the cavities, showing what we expect to see when we take reflection spectra of single molecules coupled to these cavities. In addition, I describe the optical setup that has been developed to take these measurements.

I conclude with proposed improvements to the cavity setup that will enable these reflection spectra to be more easily taken. This will allow these molecule-cavity systems to be used as infrared single photon sources for quantum optics experiments.

CONTENTS

Abstract **1**

Declaration **4**

Acknowledgement **5**

List of Figures **6**

List of Tables **11**

Abbreviations **12**

Symbols **13**

1 Introduction **15**
1.1 Single Photon Sources . . . 15
1.2 Single Molecules as Single Photon Sources . . . 19
1.3 Dibenzoterrylene in Anthracene . . . 21
1.4 Optical Cavities . . . 22
1.5 Experimental Cavity Quantum Electrodynamics . . . 25
1.6 Thesis Guide . . . 27

2 The Molecules **28**
2.1 Polycyclic Aromatic Hydrocarbons . . . 28
2.2 Dibenzoterrylene: Chemical Structure . . . 29
2.3 Optical Transitions . . . 31
2.4 Anthracene Crystals . . . 33
2.5 Insertion of Dibenzoterrylene into Anthracene Crystals . . . 35

3 Growing Crystals **37**
3.1 Crystals . . . 37
3.2 Growing Anthracene . . . 37
3.3 Cosublimation . . . 41
3.3.1 Comparison of previous sublimation methods . . . 41
3.3.2 Vapour Pressure of Anthracene . . . 43
3.3.3 Initial Sublimation of Anthracene . . . 43
3.3.4 Growing Doped Crystals . . . 44
3.3.5 Vapour Pressure of DBT . . . 44
3.3.6 Oven Design . . . 48
3.3.7 Growth Parameters . . . 51

3.4 Crystal Protection . . . 52
3.5 Confocal Microscopy . . . 54
3.6 Sample Characterisation . . . 57

4 Cryogenic Microcavities **75**
4.1 Theory . . . 75
4.2 Cavity Characterisation . . . 80
4.3 Cryogenic Cavity . . . 84
4.4 Mirror Improvements . . . 93

5 Cavity QED **97**
5.1 Introduction . . . 97
5.2 Jaynes-Cummings Hamiltonian . . . 97
5.3 Decays . . . 100
5.4 Simulations . . . 103

6 Experimental Setup **106**
6.1 Reflectance Measurements . . . 106
6.2 Optical Setup . . . 106

7 Summary and Outlook **115**
7.1 Summary . . . 115
7.2 Outlook . . . 116

Appendices **120**

Appendix A Cavity Overlap Integral **121**

Bibliography **131**

DECLARATION

I declare that all the material in this thesis is my own unless otherwise stated and referenced.

The copyright of this thesis rests with the author and is made available under a Creative Commons Attribution Non-Commercial No Derivatives licence. Researchers are free to copy, distribute or transmit the thesis on the condition that they attribute it, that they do not use it for commercial purposes and that they do not alter, transform or build upon it. For any reuse or redistribution, researchers must make clear to others the licence terms of this work.

ACKNOWLEDGEMENT

I would like to thank my examiners, Prof. Michel Orrit and Prof. Stefan Maier, for taking the time to read and assess this thesis. I would like to thank Prof. Ed Hinds for his supervision, advice and wisdom. Thank you to Jaesuk Hwang for his knowledge and guidance in the first stages of this work. Thank you to Alex Clark for being often my first port of call with problems and the first to look over much of this thesis. For the many discussions, arguments, shared problems and shared solutions, I would like to thank my fellow students: Claudio Polisseni, Sam Grandi and Sebastien Boissier. For their lab expertise and generally making the whole experience mostly painless, I thank Yu-Hung Lien, Ben Sauer and every other member of the Centre for Cold Matter. Also, thank you to Jon Dyne, Steve Maine and Val Gerulis for their invaluable technical expertise and thank you to Sanja Maricic, Judith Baylis and Marcia Salviato for greasing the wheels of academia. Finally, thank you to my parents, brothers, friends and family for not moaning too much when I start talking about physics. And Cesca, thank you.

LIST OF FIGURES

1.1 The predicted $g^{(2)}(\tau)$ curve for a single emitter showing antibunching at short times ($\tau_1 = 4\,\text{ns}$). 16

2.1 A stick and ball model of dibenzoterrylene ($C_{38}H_{20}$). Grey atoms are carbon and white are hydrogen. DBT is shown in its lowest energy free space conformation. Image was generated using Molekel visualisation software [73]. 28

2.2 DBT orbital electron density: a) The highest occupied molecular orbital (HOMO). b) The lowest unoccupied molecular orbital (LUMO). The orbitals were calculated using DFT in the ORCA package. 30

2.3 An energy level diagram of DBT. Straight arrows show optical transitions and wavy arrows represent nonradiative transitions. Details in the text. . 31

2.4 Left: A stick and ball model of the unit cell of anthracene. Only carbon bonds are shown for clarity. The angle between the a and c axis is $\beta = 124.7°$. Right: A top view looking down on the unit cell to show the herringbone packing structure. The molecules on the bottom of the unit cell are shown grayed out to distinguish them from those on the top. . . . 33

2.5 A diagram of a crystal of anthracene showing the crystal habit. The crystal axes a, b, and c and the indices of refraction n_x, n_y, and n_z are also shown 34

3.1 A crystal of anthracene grown between two coverslips viewed under crossed polarisers. The sample on the left was not annealed, the sample on the right was. Regions of the same colour are the same crystalline region. . . . 38

3.2 The sublimation vessel used for initial growth of anthracene crystals. . . . 43

3.3 The fit of heat of fusion (left) and heat of vaporisation (right) against molecular connectivity, the line shown is the linear fit to the data with the error shown as the shaded band. 46

3.4 Different estimates of the vapour pressure of DBT. The dashed lines are vapour pressures estimated from two different group contribution models [125, 126]. The upper band (blue) is obtained by correlating the Antoine coefficients with connectivity. The lower band (orange) is the estimate obtained from connectivity-correlated heats of vaporisation and fusion, together with the measured melting point and the estimated boiling point. . 47

3.5 The vapour pressure of a various different PAHs at 160°C against their molecular connectivity. Also shown is the predicted vapour pressure at 160°C as a function of the molecular connectivity. The dashed red line shows the molecular connectivity of DBT. 47
3.6 Cross-section of the oven design showing the main body with crucible and collection plate assemblies. A: anthracene Crucible. B: DBT Crucible. C: Collection plate. D: View port. E: Vacuum port. 49
3.7 Exploded view of the collection plate heating/cooling assembly. F: Water-cooled nut. G: PEEK spacers. H: Cartridge heater holder. I: High temperature O-rings. J: TEC heater/cooler. K: Collection plate. 50
3.8 The 'cling film' method of overcoating anthracene crystals with PMMA. A: Spin coating a thin film of PMMA onto a coverslip. B: Floating the PMMA film on water. C: Fishing out the film. D Drying procedure. E: Using the film to cover an anthracene crystal. 53
3.9 The layout of the room temperature oil objective confocal microscope showing the effect of displacing the galvo mirrors to vary the position of the focal spot. 54
3.10 The layout of the cold confocal air objective microscope showing the effect of displacing the galvo mirrors to vary the position of the focal spot. . . . 55
3.11 Left: A white light optical image using a CCD camera of the crystal that is imaged in the confocal microscope. The scan area is highlighted by a dark square. The attenuated laser spot can be seen in the bottom right hand corner of the square. Right: A room temperature confocal scan in x, y and z of $16 \times 16 \times 16\,\mu\mathrm{m}^3$ volume of anthracene crystal doped with DBT. The xy scan was taken at z= 7.5, the xz scan was taken at y= 0 and the yz scan was taken at x= 15. The inset shows the area highlighted on the x and y scan showing a dark streak left by a molecule that has blinked off indicated with an arrow. 57
3.12 DBT concentration versus temperature. Blue circles show the measured concentrations. Lines show predictions from the various sources mentioned in section 3.3.2 (with prediction from heats and, boiling and melting points omitted). 58
3.13 A trace of the fluorescence from a single molecule as the excitation polarisation is varied. 60
3.14 Scatter plot of the normalised maximum intensity and the orientation relative to anthracene b axis for 113 DBT molecules. Histograms of each parameter are shown on the edges of the plot. 61
3.15 A saturation curve for a single molecule at room temperature, $I_{sat} = 170 \pm 20\,\mathrm{kW/cm^2}$. 62
3.16 A simplified energy level diagram of DBT for the three level model of $g^{(2)}(\tau)$. 63

3.17 The predicted $g^{(2)}(\tau)$ curve for a single molecule with multiple levels shown in figure 3.16. The short-dashed orange curve shows the molecule being driven resonantly with the ZPL at a high rate and demonstrates Rabi oscillations at short times and photon bunching due to the triplet state at longer times. The dashed red line shows the observed second order correlation at room temperature at the same saturation, at room temperature the dephasing rate, Γ_2 is greatly increased. The solid red curve shows the response from a single molecule being driven resonantly at low pump powers. The dot-dashed yellow line shows the second order correlation function for a molecule that is driven at low power at room temperature. The blue line shows the molecule being driven from the ground state, $|1\rangle$, to level $|3\rangle$. More details in the text. 66
3.18 A $g^{(2)}(\tau)$ curve for short times showing antibunching for zero time delay. The fitted line is equation 3.38 which yields visibility of 91% and lifetime $\frac{1}{\Gamma} = \tau_1 = 3.11\,\text{ns}$ 67
3.19 A graph showing the combination of short and longer timescale autocorrelation measurements. 69
3.20 A graph showing the longer timescale autocorrelation measurements. The fit is of the form of equation 3.40. 69
3.21 The emission spectrum of a single DBT molecule. The edge of the 800 nm longpass filter can be seen and the peak at 786.0 nm is the residual excitation laser light. Other emission lines are labelled with their wavelength. It should be noted this molecule is in the wings of the inhomogeneous distribution. 71
3.22 The lineshape of the zero phonon line transition of a DBT molecule at 390 nW. The fitted function is a Lorentzian with FWHM of 56 ± 8 GHz. . 72
3.23 The summed counts of multiple images at different laser frequencies showing the distribution of the zero phonon lines of individual DBT molecules. The images are taken at the frequencies indicated by the red points. 73
3.24 The linewidth of a single cold DBT molecule. The fitted curve is a Lorentzian with a FWHM of 55 ± 2 MHz. 73

4.1 The optical fibre v-groove array with attached Bragg reflector brought up to the array of round mirrors to create an optical microcavity 75
4.2 The radius of curvature of a Gaussian beam expanding in free space with the mirror radius shown as a dotted line. 76
4.3 The theoretical modes of a cavity with the fibre misaligned by 0.7 beamwidths of the input mode in each direction. The higher order radial modes are seen as smaller peaks beside the fundamental modes. 79

4.4 The graph of the overlap integral of the first eight modes of the cavity with a displaced Gaussian function as the cavity is misaligned in the x direction. At $x = 0$ only the fundamental mode has any overlap, as x increases the higher order radial modes have a significant overlap, thus higher order radial modes are excited in the cavity. 80
4.5 Two scans of the length of the cavity with the polarisation controller set at horizontal and vertical polarisations (shown in different colours). The peaks of one polarisation are visible as attenuated peaks in the other. The split modes due to the mirror asymmetry and higher order Hermite-Gaussian modes are also visible. 81
4.6 The predicted visibility from overlap integral (lines) and measurement (points) of the visibility of the fundamental traverse and first two higher order radial mode reflection resonances as the cavity is misaligned along one axis. . . . 82
4.7 Cavity length as determined by two different methods. 83
4.8 A simplified cavity design demonstrating the various components. 85
4.9 The insert design of the cavity showing removable inserts with adjustment threads. Inset: Detail of symmetrical v-groove arrays mounted on piezo stacks. The micromirror array is mounted to the face of one of the v-groove arrays. 86
4.10 A single round mirror photographed from the top and in section. 87
4.11 The assembled Nylon-12 prototype cavity mount. 87
4.12 Top view of the aligned cavity. The top section of the photograph shows the dummy v-groove with mirror chip attached to the end face. The individual round mirrors are the dark circles on the mirror chip face. The lower section shows the v-groove array with 12 fibres seen as white lines running down the lower half of the image. 88
4.13 The hysteresis of the two piezo stacks measured using the transmission peaks of the cavity. This scan was taken with a triangular ramp with the direction of movement shown on the plot. Each dot represents the peak of a fundamental mode found during the scan. The fits are separate cubic polynomial functions for each direction. This is shown from room temperature down to liquid nitrogen temperatures. 89
4.14 The flexure design which manages $\approx 11\mu m$ travel along each axis but presents a significant hysteresis ($\approx 4\mu m$). 91
4.15 A cutaway of the cavity showing the attocube attached to the attocube block mount with piezo block on top. 91

4.16 The effect of many thermal cycles on the state of the mirror coated on the v-groove array face. The top image is after only a few thermal cycles The laser spot is visible on the right side of the image. The lower image is after more than a dozen cycles. The flaking is seen predominantly on the lower silicon half of the assembly. 93
4.17 The reflectance spectrum of one of the new mirror designs over the relevant range. This has a reflectance of 98.5% at 785 nm and a reflectance of 1.6% at 766 nm. 95

5.1 A graph showing the expected ratio of reflected power to that incident on the cavity as the laser is detuned across resonance of the cavity and molecule. The coupling factor is $2^s\, g_0$ where from top to bottom $s = 2, 1, 0, -1, -2$ (Plots are offset for clarity). 104

6.1 Laser locking setup with FP cavity for locking the ECDL laser with a normalisation detector (DET100A/M). The frequency of the ECDL laser can then be changed by scanning the length of the FP cavity. The fixed quartz cavity is for monitoring the frequency during the scan. 108
6.2 The fibre optic setup for observing the cavity reflection spectrum of the cryogenic cavity. 109
6.3 The free space setup for measuring the reflection spectrum of the cryogenic cavity. 110
6.4 The reflection spectrum of a single peak of the microcavity varying both the microcavity length and the excitation laser frequency. 111
6.5 The connections and ports of the helium bath/flow cryostat. The two chambers, the helium reservoir and the VTI chamber, are housed inside the outer vacuum chamber (OVC). The two chambers are connected by a needle valve and both have several ports to admit gases and liquids. 112
6.6 A scan of the microcavity at 4.3 K. The finesse of the cavity is 8.4 with a visibility of 7.7%. 113

7.1 A flexure based design for a single cavity. The design uses the amplified motion of a single piezo actuator to scan the cavity length. Details in text. 118

LIST OF TABLES

3.1 A table of growth parameters from previous growth of anthracene crystals 42

4.1 The new mirror designs that allow a high reflectance at the wavelength of the zero phonon line but permit transmission at the excitation wavelength. 95

4.2 A table of predicted finesse and Purcell factor for a single DBT molecule inside the cavity. 96

ABBREVIATIONS

AOM	acousto-optic modulator
APD	avalanche photodiode
CAD	computer aided design
DBR	distributed Bragg reflector
DBT	dibenzoterrylene
DFB	distributed feedback
DFT	density field theory
ECDL	extended cavity diode laser
FDTD	finite-difference time-domain
FP	Fabry-Pérot
FSR	free spectral range
HOMO	highest occupied molecular orbital
LUMO	lowest unoccupied molecular orbital
NA	numerical aperture
NV	nitrogen-vacancy
OVC	outer vacuum chamber
PAH	polycylic aromatic hydrocarbon
PID	proportional integral derivative
PMMA	polymethyl methacrylate
PTFE	polytetrafluoroethylene
PVA	polyvinyl alcohol
SPDC	spontaneous parametric downconversion
QED	quantum electrodynamics
TEC	thermoelectric component
VTI	variable temperature insert
ZPL	zero phonon line

SYMBOLS

I have tried to maintain a consistent notation throughout this thesis. Below is a partial list of the symbols used.

a, b, c	=	crystal directions
$\hat{\boldsymbol{a}}^\dagger$, $\hat{\boldsymbol{a}}$	=	creation and annihilation operators
A, B	=	Antoine coefficients
$\boldsymbol{A}$, $\boldsymbol{B}$	=	angles between faces in crystal habit
β	=	angle in monoclinic crystal unit cell
${}^1\chi_v$	=	molecular connectivity
d_{if}	=	dipole moment of transition from $\|i\rangle \rightarrow \|f\rangle$
δ	=	number of bonds connected to an atom
ΔH_f	=	heat of fusion
ΔH_s	=	heat of sublimation
E	=	energy
$\mathcal{E}$ or $\mathscr{E}$	=	electric field
F_P	=	Purcell enhancement factor
g	=	coupling constant
$g^{(2)}$	=	second order correlation function
Γ	=	population transition rate in units of angular frequency, usually of ZPL
Γ_2	=	decoherence rate in units of angular frequency
$\hat{H}$	=	Hamiltonian
H_n	=	Hermite polynomial
$\mathcal{H}$	=	Hilbert space
I	=	intensity
I_{sat}	=	saturation intensity
k	=	wavenumber
k_{ij}	=	transition rates
κ	=	the linewidth of a cavity in units of angular frequency
l	=	a fixed length
$\mathcal{L}\{\}$	=	Laplacian transform
m	=	mass
$\boldsymbol{M}_{ij}$	=	transition element

μ	=	chemical potential
n_i	=	refractive index in the direction i
N	=	a fixed number
$\mathcal{N}_A$	=	Avogadro's number
ν	=	frequency
ω	=	angular frequency
ω_c	=	angular frequency of a cavity
ω_m	=	angular frequency of a molecule
p	=	pressure
P	=	power
p_{atm}	=	atmospheric pressure
p_{vap}	=	vapour pressure
ϕ_S	=	intersystem crossing rate
Q	=	the quality factor of a cavity
r_i	=	reflected field
R	=	rate
R	=	molar gas constant
R_i	=	reflected intensity
R_∞	=	saturated rate of fluorescence
$\mathcal{R}$	=	radius of curvature
ρ	=	density
$\boldsymbol{\rho}$	=	density matrix
S	=	saturation parameter
$S_{x,y}$	=	a singlet level: x signifies the electronic level and y the vibronic level
$\hat{\boldsymbol{\sigma}}_i$	=	Pauli matrices
t_i	=	transmitted field
T	=	temperature
T_i	=	transmitted intensity
T_b	=	boiling point
T_m	=	melting point
$T_{x,y}$	=	a triplet level: x signifies the electronic level and y the vibronic level
τ	=	time delay
τ_1	=	lifetime of ZPL emission
θ, ψ, ϕ	=	angles
v	=	velocity
V	=	volume
bold	:	denotes a vector or tensor quantity
$\hat{}$	:	denotes a quantum mechanical operator

CHAPTER 1

INTRODUCTION

1.1 Single Photon Sources

The concept of light as a photon began as a solution to the ultraviolet catastrophe and as an explanation of the photoelectric effect at the turn of the 20th century. Since that time, photons have passed from mathematical trickery, through readily observable phenomena, to a useful resource. The photon, due to its robustness against decoherence, demonstrates many characteristics of an ideal quantum mechanical state. The quantum mechanical behaviour of these single particles of light mean that they can and will be used as part of emerging quantum technologies. Improved measurements using highly entangled quantum mechanical states, secure quantum communication and the lofty promises of universal quantum computation all rely on the construction of reliable sources of these very states [1, 2]. Single photons could provide such a quantum mechanical resource as well as being useful for fundamental tests on quantum physics itself.

To date, a perfect single photon source has not been realised. Different applications exploit different characteristics of single photons and, as yet, no source can fulfil all of these needs. An ideal single photon source will produce exactly one single photon at a well defined time and with a high enough repetition rate to be useful. Such a source, could be used, for example, as an absolute standard for optical brightness [3]. For this application, it would be necessary to have good control of the wavelength of the emitted photon. Many applications that require the photons to be indistinguishable from one another, would also need the wavelength of each photon to be fixed. Indistinguishability further requires that as well as having the same wavelength, the photons must also have the same polarisation. So, a good single photon source will also emit photons in a defined polarisation.

When talking of a single photon, as emitted from a single photon source, what is meant is an excitation of the electromagnetic field that is localised in space and time. The electromagnetic field can be represented using a set of basis modes. The set of basis modes can be, for example, a set of travelling waves in a finite box or as the resonant modes of an optical cavity. Each of these modes, when quantised, is equivalent to the

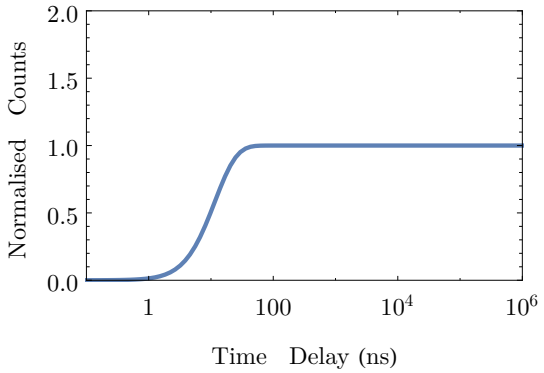


Figure 1.1: The predicted $g^{(2)}(\tau)$ curve for a single emitter showing antibunching at short times ($\tau_1 = 4\,\text{ns}$).

quantum harmonic oscillator. So, it has energy eigenvalues of $\hbar\omega(n+\frac{1}{2})$. $\hbar$ is the reduced Planck constant and ω is the angular frequency of the mode. When the field is in the corresponding eigenstate it is in a state of n photons, each photon having a unit of energy $\hbar\omega$. A state with a defined number of photons is called a Fock state. To detect these photons we can use the photoelectric effect. Each photon that lands on a photodiode is annihilated and promotes an electron to the valence band of the detector material [4]. This is amplified to a measurable electrical pulse which we register as detection of a single photon.

The number of photons can also be measured without annihilation by a quantum nondemolition measurement [5]. This has been demonstrated by determining the photon number inside a cavity by detecting the phase shift on Rydberg atoms transiting the cavity [6]. In this thesis we detect the light from single emitters using an avalanche photodiode thus annihilating the created photon.

An important way to quantify a single-photon emitter is to measure the second order correlation of the light emitted. This is the correlation of the intensity from the source at a time t with the intensity at some later time $t+\tau$.

$$g^{(2)}(\tau) = \frac{\langle I(t)I(t+\tau)\rangle}{\langle I(t)\rangle^2} \tag{1.1}$$

When we consider a classical beam of light with an intensity that is constant in time we can easily see that $g^{(2)}(\tau) = 1$ for all values of τ. However, when we consider a quantum mechanical source of light the value of $g^{(2)}(\tau)$ can differ from this substantially. Light emission from an ideal single emitter has a correlation $g^{(2)}(\tau) = (1 - e^{-\tau/2\tau_1})^2$ when the emitter is an isolated two-level system being driven weakly and τ_1 is lifetime of the excited state of this two level system [7]. A plot of this is seen in figure 1.1.

The correlation at short times goes to zero. This is because once the system has emitted a photon it needs to be re-excited in order to emit another photon. For weak

excitation the excited state probability builds up again over a time characterised by the excited state lifetime, so the curve shows a dip with a width of the order of that emitter lifetime. The lifetime of the emitter in figure 1.1 is chosen to be 4 ns which is similar to the lifetime of the emitter we consider.

This antibunching behaviour is characteristic of a single photon source and is a truly quantum mechanical property of the light. The first demonstration of antibunching was performed with a sodium beam in 1977 [8]. A molecular sodium beam was attenuated to the point were only one atom was within the region where atoms could be excited with a laser and the fluorescence was observed perpendicularly to the beam. Because this used a beam of atoms as the quantum emitters, it suffered due to the difficulty of interrogating such atoms for long periods of time.

By holding atoms within an ion trap this problem was largely overcome. In 1987, Dietrich and Walther showed the possibility of creating non-classical light from a single magnesium atom held in a radio-frequency Paul trap [9]. They were also able to vary pumping intensity and demonstrate more structure in the second order correlation function as the ion is driven from the excited state back into its ground state in characteristic Rabi oscillations. The major drawback to the use of single trapped ion is that the collection efficiency of the photons is limited as the ion can emit in any direction.

The use of spontaneous parametric downconversion (SPDC), discovered in 1970 [10], meant that single photons could be generated in a defined optical mode allowing them to be more readily used. These photons are generated within a nonlinear medium illuminated by a pump beam where a single photon of the pump beam is converted into two photons of twice the wavelength of the original pump. Because the two photons are generated together the detection of one can herald the presence of the other as was demonstrated by Hong and Mandel in 1986 when they detected the presence of a photon in precisely this way [11].

The SPDC process has since become the workhorse method for generating single photons for quantum optics experiments. Unfortunately, it is still hampered by the intrinsically probabilistic nature of the downconversion process. However, there are sources which use SPDC and try to address these problems by delaying and redirecting photons to make the source more on-demand [12]. Using a Pockels cell, one of the downconverted photons can be directed into a storage loop for a variable amount of time and then retrieved within a specific window. Recently, Kaneda *et al.* showed a time-multiplexed SPDC source that produces single photons in a regular time bins spaced by several hundred nanoseconds with probability 38.6% [13].

Another way of using optical nonlinearities to create single photons is through four wave mixing. A nonlinear $\chi^{(3)}$ medium can convert two photons from a pump beam into another two photons of differing wavelengths. Where again the presence of one photon can indicate the existence of the other and can be spectrally separated. This has been shown to occur in microstructured fibres and in photonic crystal waveguides [14, 15].

Ideally, we would use sources that have the prompt fluorescence of single atoms while emitting into well defined modes that can be easily utilised. The coupling of single emitters to optical structures is a way to achieve just that. Small optical cavities have been developed in the Centre for Cold Matter at Imperial College London to couple single rubidium atoms to a well defined cavity mode [16, 17]. These structures increase the coupling of a single atom to the cavity field and can be used for the detection of single atoms at a high fidelity [18]. The increased coupling means these cavities can also be used as part of photon sources though the atom only transits the cavity. Hijlkema *et al.* have shown a rubidium atom confined by an optical dipole trap in a small open cavity can encourage the emission of light into the cavity mode for tens of seconds [19]. While this begins to deal with the emission collection problem it is still encumbered by the heavy requirements of traps for many of these types of source to be used together. It would of course be an ultimate goal for a well designed single photon source to be used in parallel with other such sources for the kinds of applications we have in mind.

Alternative emitters to atoms are not tied to traps, and these may ultimately be more scalable. Quantum dots show promise as single emitters and have the advantage that they are manufactured with mature semiconductor technologies. A quantum dot is a small region of semiconductor with a narrow band gap surrounded by a region of semiconductor with a larger band gap. Electron-hole pairs form quantised bound state excitons that are localised within the narrow band gap material. Recombination of a pair leads to emission of a photon, and these structures behave like 'artificial atoms'. By embedding quantum dots into a microdisc resonator, Michler *et al.* showed that these structures can enhance the emission of specific excitons, generating photons with high efficiency [20]. They can also be placed into other high finesse structures such as photonic crystals that guide the emitted photons to allow easy collection and detection [21].

These semiconductor systems also have the advantage that they can be electrically driven [22]. In addition, when cooled below 7 K they have shown the potential to generate indistinguishable photons [23, 24]. Using the excitation of multiple electrons, creating a bi-exciton, quantum dots have even been shown to emit polarisation-entangled photon pairs [25]. The variety of quantum dot materials also permits the generation of photons at many different wavelengths, ranging from the visible to infrared telecommunications wavelengths. Cavities for quantum dots are normally constructed from the semiconductor materials that the quantum dots themselves are made from such as micropillars, microtoroids and photonic crystals [26, 20, 21]. It is also possible to couple quantum dots to open cavities that are very similar in geometry to those we hope to use here with single molecules. In 2009, Muller *et al.* grew quantum dots on top of a distributed Bragg stack reflector (DBR) with a high reflectance and then approached the surface with an optical fibre which had a concave mirror attached to the end of it with a slightly lower reflectance [27]. They demonstrated a much increased emission from a single quantum dot when the cavity was resonant with the emission of the dot.

Solid state alternatives to these 'artificial atoms' can be based on actual atoms such as rare earth dopants [28]. These are isolated rare earth atoms in silicates or synthetic crystals, such as praseodymium in yttrium aluminium garnet. While rare earth dopants have been used for some time in solid state lasers, their use as single emitters is quite recent. In addition to single dopant atoms in a crystal, solid state emitters may also be based on defects associated with a lack of atoms. This is the case for vacancy centres in diamond [29]. The nitrogen-vacancy (NV) centre is a point defect in the diamond lattice which consists of a nitrogen atom and adjacent vacancy. The hanging bonds of this defect present a localised state that can be optically excited and used to generate single photons. The NV centres in diamond can be neutral (NV^0) or negatively charged (NV^-). The negatively charged centre is the more studied of the two and its triplet ground state has enabled the manipulation of the electron spin of the NV^- centre [30]. This structure makes the NV^- centre a promising candidate for a solid state qubit. For single photon production the zero phonon line (ZPL) is located at 637nm, the zero phonon line is the emission from a purely electronic transition within the NV and not involving transition between local vibronic states or the creation and annihilation of phonons in the crystal. This ZPL is accompanied by a red-shifted vibronic band which does involve these transitions [31]. The amount of emission on the zero phonon line compared to the vibronic band is $3-5\%$, less than for the organic molecules we will shortly consider [32]. Fu *et al.* measure a linewidth of the ZPL of NVs as 16.2 MHz though it is subject to spectral diffusion over many tens of gigahertz [33]. The NV centre is a good single emitter though it does have a complicated energy level structure and low zero phonon line yield, even at low temperatures.

Diamond has a high refractive index and collecting the emission of a single vacancy centre into free space can be hampered by the total internal reflection at the boundary of the diamond. To address this issue, NVs have been created in nanodiamonds, though this can lead to an increase in the excited state lifetime [34]. Vacancy centres have also been coupled to optical structures to enhance the emission either surrounding the diamond or constructed from the diamond itself as in microdiscs or ring resonators [32, 35, 36]. The vacancies explored are not limited to nitrogen. Diamond possesses many colour centre defects and the silicon vacancy is another single emitter which has a branching ratio of 88% on the zero phonon line [37] and very recently has been shown to approach lifetime limited emission [38]. In fact, optically active defect centres are not only present in diamond. Anti-site vacancy pairs in silicon carbide have also recently been isolated as bright emitters even without optical structures to enhance the emission [39].

1.2 Single Molecules as Single Photon Sources

Single molecules are also bright sources of streams of single photons. The absorption of light by a single molecule was first detected in 1989 by Moerner and Kador [40], using a single cold (1.6 K) pentacene molecule in a *para*-terphenyl crystal. They discerned the

small signal from the background by a double modulation technique which varied both the excitation frequency of the laser and that of the molecular transition itself. Soon after, Orrit and Bernard detected individual pentacene molecules in the same host by their fluorescence [41]. The single molecule was excited by a dye laser through an optical fibre that was in contact with the *para*-terphenyl crystal and the fluorescence collected by a parabolic mirror. This detection technique is essentially the same method that we use in this thesis to detect our single molecules in our confocal microscope. Further fluorescence studies resolved single molecules spatially as well as spectrally, and discovered the spectral diffusion of single emitters [42]. This spectral diffusion was seen in the time trace of fluorescence from a single molecule as very rapid changes in intensity. It is also seen in spectra of the single emitters taken at different times, where the peak fluorescence frequency shifts around over time. This diffusion is a useful tool to investigate the surrounding matrix but is not desirable if the planned use of the single emitter is as a source of single photons.

Since the first observation of a single pentacene molecule, many other molecules in various different hosts have been investigated. For example, terrylene also in *para*-terphenyl [43], dibenzanthanthrene in a naphthalene matrix [44] and the first observation of single dibenzoterrylene (DBT) molecules in a naphthalene matrix [45]. In fact, the number of systems is rather large. Single molecule investigations have been performed on many organic molecules already [46]. There is also some work being done to increase the number of available dyes for these experiments. By replacing hydrogen atoms on the aromatic hydrocarbons with fluorine or bromine atoms, the emission frequencies as well as other properties can be altered [47]. Even the same molecule in different environments can have very different properties, giving a wealth of molecule-host systems to choose from.

The dibenzanthanthrene molecule, this time in a *n*-hexadecane matrix, was developed into a single photon source by placing the sample onto a silica plate with two aluminium electrodes [48]. The sample was constantly illuminated by a continuous-wave laser while a radio frequency signal was applied to the two electrodes to Stark-shift the excitation frequency of the molecule. The molecule was then excited upon each passage of the transition frequency through the frequency of the laser. This generated a stream of fluorescence photons that were collected by a parabolic mirror. These photons were delivered at 6 MHz with a probability of 74%.

Terrylene molecules were also chosen to be used as sources of single photons on demand, this time at room temperature [49]. The molecules were excited at a rate of 6.5 MHz by a pulsed laser with 35 ps wide pulses, and it was found that the molecule yielded a photon after each pulse with 83% probability. The photons emitted in this experiment were not identical because the sample was at room temperature and therefore the emission frequency was greatly broadened by collisions with phonons.

Toninelli *et al.* used DBT molecules, but this time in an anthracene matrix, when they coupled a single emitter to an optical cavity at room temperature [50]. The cavity formed between a plane mirror and the end of an optical fibre which had been machined to be

concave by CO_2 laser ablation and then coated with gold. The crystals were formed by spin coating a solution of anthracene and DBT onto the planar mirror. Then a microscope objective placed under the mirror collected the light that was transmitted through it. They showed that collection was increased when the cavity was in place, though only a very small enhancement was seen.

In an experiment to see how strongly a light field could be coupled to a single molecule [51], Gerhardt *et al.* subjected dibenzanthanthrene molecules to scanning near-field optical microscopy. This uses a tapered optical fibre that has been coated in aluminium and then had a sub-wavelength hole milled in the end of it using a focussed ion beam. These tips were then scanned across molecules in a *para*-terphenyl crystal and the transmission was monitored. When the probe was located directly over a molecule the transmitted light showed a 6% reduction. This demonstrates that significant coupling is achieved between the optical field and a single molecule by reducing the effective mode area of the light.

The interaction of light with a single molecule can also be quantified by noting the phase shift. Pototschnig *et al.* showed this by taking phase contrast microscopy images of single dibenzanthanthrene molecules [52]. They noted a phase shift of 3° from a single molecule. Recently Faez *et al.* have shown a stronger coupling of light to a single molecule using a nanoguide [53]. A glass capillary of 600nm diameter was filled with naphthalene doped with DBT and acted as a waveguide. The end of a short section of this capillary was polished to a 45° angle which allowed the light to be coupled out of the guide. When cooled to 1.5 K the narrow molecules (30 MHz) delivered 11% of their emitted light into the nanoguide.

Hwang and Hinds have also suggested that these single molecules can be efficiently coupled to waveguide structures [54]. They claim from finite-difference time-domain (FDTD) simulations that 28% of the emission of a single molecule can be coupled into a high aspect ratio waveguide. Good coupling occurs because one of the dimensions of the waveguide is reduced to maximise the field per photon just outside the guide at the position of the molecule. This requires a small mode area. The propagating field mode will then interact well with a molecule placed just outside the waveguide.

Single molecules have been shown to be ideal single-photon emitters that can effectively be coupled to optical structures to achieve directional emission, but there is clearly room for new structures to increase the emission and reliability.

1.3 Dibenzoterrylene in Anthracene

The molecule we choose to exploit is dibenzoterrylene (DBT) in an anthracene crystal. Of the numerous molecule-host combinations, this is one which has several encouraging characteristics. DBT in anthracene is a particularly stable combination and is not so susceptible to the spectral diffusion that was observed in the initial single molecule studies. The molecule also has a high quantum yield, i.e. after excitation it normally radiates a

photon. The first excited singlet state also has a very low probability of relaxing to the lower-lying triplet state [55]. That is good because decay to the triplet is followed by temporary interruption of the fluorescence until the molecule eventually returns to the ground state. Moreover, population of the triplet can lead to creation of singlet oxygen by energy transfer. This singlet oxygen then reacts with a nearby molecule and the molecule becomes permanently dark [56, 57], which is obviously undesirable. The transition frequency that we are interested in is also at a convenient wavelength $\approx 785\,\mathrm{nm}$, which enables us to use solid state lasers for excitation. This wavelength is also relatively close to the D_2 transition in rubidium which offers the potential for DBT to be interfaced with rubidium, much as dibenzanthanthrene in tetradecane already has been with sodium [58].

DBT in anthracene was first imaged by Hofmann *et al.* with a view to using these single molecules as probes for the local environment [59]. This particular combination was chosen to try to increase the stability of the emitters. The samples were prepared by co-sublimation and the intensity dependence of the linewidth and emission rate were investigated. Trebbia *et al.* managed to isolate a single DBT molecule in anthracene and measure the emission spectrum of this molecule providing a measurement of the branching ratio of the excited state to higher vibronic states of the ground state. They show that 33% of the decays are on the zero phonon line-another reason for the choice of DBT as our single photon emitter.

A fuller investigation of cosublimated samples was presented in a pair of papers in 2007 [55, 60]. In these two papers Nicolet *et al.* measured the intensity correlation $g^{(2)}(\tau)$ of single molecules and their linewidth and emission rate under various excitation powers. They also measured the emission spectra of individual molecules and identified two distinct insertion sites for DBT in anthracene. The 'main' site and 'red' site correspond to two different conformations of the DBT molecule as confirmed by simulation. This is also supported by an investigation into the orientation of single DBT molecules. The Stark coefficients and temperature dependence of the linewidth are also investigated.

In 2012, Makarewicz *et al.* investigated the vibronic structure of DBT in anthracene and a different host of 2,3-dimethylanthracene. Using a combination of fluorescence spectroscopy and density functional theory (DFT) simulations, they were able to provide more evidence for the particular conformation of DBT that is adopted within an anthracene crystal and the different vibrational states therein.

1.4 Optical Cavities

The modification of the electromagnetic modes surrounding a single emitter will cause changes in the behaviour of that emitter. This is because the interaction with the electromagnetic field is partly governed by the density of states of the field around that emitter. By placing a metal plate or mirror near the single emitter the density of states and thus

interaction with the electric field is modified. This can have the effect of changing the emission and absorption rates.

The spontaneous emission rate of an emitter transitioning from one state to another is described by Fermi's golden rule [4]:

$$\Gamma = \frac{2\pi}{\hbar} |\boldsymbol{M}_{if}|^2 \rho(E), \tag{1.2}$$

with $\boldsymbol{M}_{if} = \langle f|\mathcal{H}'|i\rangle$ as the matrix element for the transition from the initial state $|i\rangle$ to the final state $|f\rangle$ for some perturbing Hamiltonian $\mathcal{H}'$. $\rho(E)$ is the density of final states in energy after the transition. This follows from time-dependent perturbation theory provided $\rho(E)$ is constant over the spectral width of the transition. In our case, the interaction Hamiltonian is $-\hat{\mathbf{d}} \cdot \boldsymbol{\mathcal{E}}$ where $\hat{\mathbf{d}}$ is the dipole $e\hat{\mathbf{r}}$ and $\boldsymbol{\mathcal{E}}$ is the electric field. This means we can express the matrix elements as

$$\boldsymbol{M}_{if} = -e \left|\langle f|\hat{\mathbf{r}}|i\rangle\right| \mathcal{E} \cos(\chi), \tag{1.3}$$

with χ being the angle between the dipole and the field. When averaged over all orientations χ^2 is equal to 1/3. We also make the assignment

$$d_{if} = e \left|\langle f|\hat{\mathbf{r}}|i\rangle\right|, \tag{1.4}$$

with this quantity called the electric dipole moment of the transition. In some volume V the electric field in the absence of any photons is just that of the vacuum which we find by equating the energy, $\frac{1}{2}\hbar\omega$, to the integrated energy density of the electromagnetic field, $\int \epsilon_0 \mathcal{E}^2 dV$, giving

$$\mathcal{E} = \sqrt{\frac{\hbar\omega}{2\epsilon_0 V}}, \tag{1.5}$$

where ω is the frequency of the mode. Putting this together, the angle-averaged transition matrix element can be expressed by

$$|\boldsymbol{M}_{if}|^2 = \frac{d_{if}^2 \hbar\omega_0}{6\epsilon_0 V}, \tag{1.6}$$

where we have set the frequency of the mode to be equal to the frequency of the transition ω_0. For an isolated atom or molecule $\rho(E)$ is the continuum of photon states distributed over the full solid angle of free space. The total number of modes is

$$N = \int \rho(E) dE, \tag{1.7}$$

which can be expressed in momentum space as

$$N = \int \rho(k) d^3\mathbf{k}. \tag{1.8}$$

In a volume V, with length L on each side, the density in momentum space is $2\left(\frac{L}{2\pi}\right)^3$, where the factor of 2 comes from the two allowed polarisations. In this spherically averaged analysis, we can write $d^3\mathbf{k}$ as $4\pi k^2 dk$ which gives

$$N = \int 2\left(\frac{L}{2\pi}\right)^3 4\pi k^2 dk. \tag{1.9}$$

We can now change variables using $E = \hbar ck$ (also noting $V = L^3$) giving

$$N = \int \frac{VE^2}{\pi^2\hbar^3c^3} dE. \tag{1.10}$$

By inspection of equations 1.7 and 1.10 we see that

$$\rho(E) = \frac{VE^2}{\pi^2\hbar^3c^3}. \tag{1.11}$$

This is evaluated at the energy of the transition, $E = E_0 = \hbar\omega_0$

$$\rho(E_0) = \frac{V{E_0}^2}{\pi^2\hbar^3c^3}. \tag{1.12}$$

Now using the Fermi's golden rule (equation 1.2) and substituting equations 1.6 and 1.12 we obtain the emission rate for an atom or molecule in free space:

$$\Gamma = \frac{d_{if}^2{\omega_0}^3}{3\pi\epsilon_0\hbar c^3}. \tag{1.13}$$

Inside a cavity the density of modes is different. For an optical cavity we assume there is a single leaky mode inside the cavity. So the integrated mode density is given as

$$N = \int \rho(E) dE = 1. \tag{1.14}$$

The cavity is not perfect, the mode in the cavity has a finite lifetime. This means that the mode does not have a single frequency but is distributed over a small range. The density of the mode in frequency is described by a normalised Lorentzian function,

$$\rho(\omega) = \frac{2}{\pi\kappa} \frac{\kappa^2}{4(\omega - \omega_c)^2 + \kappa^2}, \tag{1.15}$$

κ is the linewidth of the cavity (and also the decay rate of energy of the field inside the cavity) and ω_c is the resonance frequency of the cavity. We can evaluate this density at

the frequency of the transition ω_0 which is

$$\rho(\omega_0) = \frac{2}{\pi\kappa}\frac{\kappa^2}{4(\omega_0 - \omega_c)^2 + \kappa^2}. \tag{1.16}$$

We can define the Quality factor of the cavity as $Q = \frac{\omega_c}{\kappa}$ and at resonance when the transition frequency and the cavity resonance are the same ($\omega_0 = \omega_c$) the expression becomes

$$\rho(\omega_c) = \frac{2Q}{\pi\omega_c}. \tag{1.17}$$

Expressing in terms of energy this is

$$\rho(E_0) = \frac{2Q}{\pi E_0}. \tag{1.18}$$

Now putting equation 1.18 along with equation 1.6 into Fermi's golden rule (equation 1.2). This gives the emission rate into this cavity mode as

$$\Gamma' = \frac{2d_{if}^2 Q}{\epsilon_0 \hbar V}. \tag{1.19}$$

In 1946, Purcell was the first to observe the modification of the spontaneous emission rate for a quantum system when placed in a resonant cavity. He observed that nuclear magnetic moment transitions were enhanced by coupling to a resonant electrical circuit [61]. The ratio of the decay rate in the cavity to free space is called the Purcell factor:

$$F_P = \frac{\Gamma'}{\Gamma} = \frac{3}{4\pi^2}\frac{Q}{V}\lambda^3. \tag{1.20}$$

This means that the rate of the transition to the cavity mode is increased for a cavity with a high quality factor and a small mode volume. This is the motivation for the small fibre based cavities that I am investigating here.

This factor is only valid when the cavity resonance is wider than the transition, and when the coupling between the cavity and the molecule is relatively weak. For strong coupling the perturbative treatment which leads to Fermi's golden rule is no longer valid, we will deal with this case in chapter 5. The simple outline given here serves to highlight the importance of sharp cavity resonances and a small mode volume to enhance the interaction of a single molecule with the electromagnetic field.

1.5 Experimental Cavity Quantum Electrodynamics

As mentioned in the previous section, the first report of a cavity-modified radiation rate was in the 1940's by Edward Purcell. The transitions he observed were in the radio fre-

quency regime. A decade later Gordon, Zeiger and Townes used a cavity in the microwave regime into which they fed a molecular beam of ammonia [62]. The ammonia beam amplified the microwave radiation inside the cavity and advanced the understanding of the interaction of matter and radiation in confined cavity modes.

The interaction and amplification of light moved into the visible with the advent of the laser in 1960 [63]. It was in this decade that a quantum mechanical model was developed to describe the interaction between and single atom or molecule and a single quantised cavity mode. Jaynes and Cummings proposed their eponymous model that will be the basis for the theoretical treatment of our system later [64].

Single emitters were successfully placed inside optical cavities in 1983. Goy *et al.* used Rydberg states of sodium in superconducting cavities to show that the amplification of the spontaneous decay of the atoms in the cavity leads to a reduction in the excited state lifetime [65]. This coupling is still in what is considered the weak-coupling regime. Where the enhancement of the decay rate is still small compared to the spontaneous decay of the excited states considered.

Soon after, Hulet *et al.* [66] showed inhibition of the spontaneous emission for Rydberg atoms passing between two plates that were spaced by less than half the emission wavelength λ. Single caesium atoms were also used by Jhe *et al.* to explore the inhibition of spontaneous emission [67]. Using a varying magnetic field they showed that the inhibition is dependent on the polarisation of the transition moment of the atom within the cavity.

The strong coupling regime, when the coupling is much larger, was entered by driving up the quality factor of cavities until Meschede, Walther and Müller managed to couple Rydberg states of rubidium to cryogenic microwave cavities at atom densities of less than one. These experiments were performed in a regime where the cavity size was similar to the wavelength of the emission, which was in the microwave regime. This made the Purcell factor $Q\lambda^3/V$ larger [68]. By contrast, optical cavities typically operate on much higher order modes and therefore require higher Q to achieve the same effect. With the developments of microfabrication techniques in the 80's and 90's, it became possible, by the early 2000s, to build small, high Q cavities in semiconductor materials [69]. Micropillar cavities consist of two parallel distributed Bragg reflector stacks separated by a spacer layer and then etched into cylindrical posts. These cavities could be filled with quantum dots and show enhancement of the spontaneous emission from these dots [70].

The advent of other types of solid state based cavities such as ring resonators and microdiscs have increased this even more, bringing experiments well into the strong coupling regime [71]. In this regime, excitation oscillates coherently between the emitter and the single mode of the cavity. For our application of a single photon source we would like to take advantage of the Purcell enhancement of the emission of the single emitter without venturing too far into the regime of strong coupling.

1.6 Thesis Guide

The rest of this thesis presents the work that I have done up to now to try and take advantage of the modified interaction of the electric field with a single DBT molecule in a optical fibre microcavity. The goal is to develop a cryogenic microcavity that we can place DBT molecules inside in order to use the single molecules as sources of single photons. In order to do this we must first grow DBT doped anthracene crystals that can be placed inside these microcavities. Chapter 2 presents the properties of the DBT molecule and its anthracene host. Chapter 3 then details the growth methods and apparatus we developed in order to grow these samples with a high level of control. I also present the characterisation of these samples both at room and cryogenic temperatures. The growth of suitable crystals complete, I then turn to the microcavity itself. The next chapter, chapter 4, details the design and performance of the cryogenic cavity to couple molecules at low temperatures. In order to test the coupling of the single molecules with the microcavity, we would like to observe the spectrum of the molecule-cavity system. Chapter 5 presents a more detailed examination of the cavity QED explanation of the behaviour of a molecule in a cavity and predicts the reflection spectrum of a cavity with a single resonant DBT molecule inside it. Finally, I present the optical experimental setup for performing the experiment to observe the simulated reflection spectrum and measure the coupling of the molecule to the cavity. The thesis finishes with an outlook to future cavities and further experiments.

CHAPTER 2

THE MOLECULES

2.1 Polycyclic Aromatic Hydrocarbons

Aromatic hydrocarbons are composed of cyclical benzene rings bonded together. The carbons are in conjugated π-bonds which give them chemical stability. The name aromatic comes from the fact that the first compounds of this group to be isolated were pleasant smelling oils and balsams including benzaldehyde from almond oil [72]. Most of the aromatic hydrocarbons that have more than 1 ring (polycyclic) are derived from substances found in coal tar. Derivatives of these components, developed in the mid 19th century, yielded synthetic dyes first used for dyeing cloth and later in dye lasers; it is these derivatives that we are interested in using. Dibenzoterrylene is a large polycyclic aromatic hydrocarbon (PAH) with a green appearance due to its absorption in both the blue and red. Our host material anthracene is a smaller PAH that crystallises readily and has been well researched.

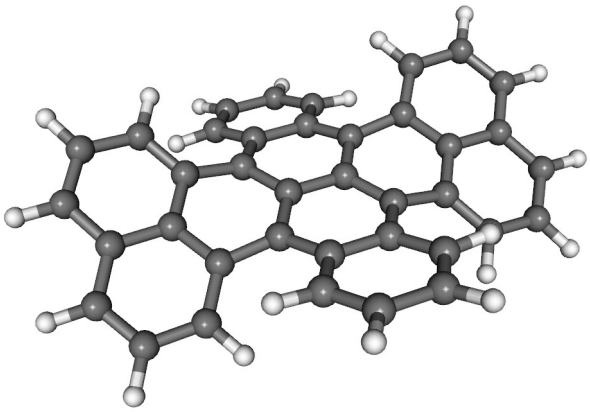


Figure 2.1: A stick and ball model of dibenzoterrylene ($C_{38}H_{20}$). Grey atoms are carbon and white are hydrogen. DBT is shown in its lowest energy free space conformation. Image was generated using Molekel visualisation software [73].

2.2 Dibenzoterrylene: Chemical Structure

Dibenzoterrylene (DBT), chemical formula $C_{38}H_{20}$, is a large PAH that has 10 fused aromatic rings, as illustrated in figure 2.1. It consists of a central tetracene moiety with two additional naphthalene moieties on either side. When discussing the structure, it is useful to assign dihedral angles to the orientation of these groups. In the most stable, free space, conformation of DBT the two naphthalene groups are tilted with respect to central plane of the tetracene moiety at an angle θ. Also, the benzene rings at each end of the tetracene group are tilted with respect to the two central rings at an angle ψ [74].

I confirmed this for myself by making a density functional theory (DFT) simulation of a single DBT molecule in free space using the ORCA package [75]. This employs some simplifications in order to solve the Schrödinger equation for the electrons in the DBT molecule. Rather than using the full wavefunction of many particles, the Hartree-Fock approximation represents the electrons as an antisymmetrised product of one-electron wavefunctions in the molecule [76]. To find the energy of a particular wavefunction we are required to calculate the correlation and exchange integrals, which represent the electron-electron interactions in the molecule. Rather than solving these integrals directly, DFT recasts the problem of determining the energy into functionals of the electron density. These have terms corresponding to the correlation and exchange integrals in the Hartree-Fock equations and are dependent on the electron density and the gradient of the electron density at different spatial coordinates of the molecule. They are termed hybrid functionals. My simulation uses the hybrid functionals B3LYP with the RI-J and COSX approximations [77, 78]. The electron densities are represented on a basis set which is composed of Gaussian orbitals around each atom in the molecule, specifically the def2-TVZ basis set [79], which uses multiple basis sets for the valence electrons of the atoms in the molecule. We can solve for the ground state of the DBT molecule by minimising the energy with respect to the positions of the atoms and hence we find its conformation.

My calculation yielded $\theta = 29\,^\circ$ and $\psi = 12\,^\circ$. These are close to the angles quoted in the literature for the conformation of DBT when it is inside an anthracene crystal [60]. It also gives the electron density of the highest occupied molecular orbital (HOMO) and the lowest unocupied molecular orbital (LUMO), shown in figure 2.2. The figure shows surfaces of constant charge density for negative (red) and positive (blue) probability amplitudes of the electron wavefunction. When an electron transitions between the HOMO and LUMO states there is an associated transition dipole moment. This dipole points across the central tetracene moiety towards the two naphthalene units and lies in the plane of the central two tetracene rings. The excited states that we use involve the promotion of one electron to the LUMO state. The spins of the hole in the HOMO state and the electron in the LUMO state combine to form a singlet (triplet) state when they are anti-parallel (parallel). These are the electronic states shown in figure 2.3 later. The energy of the singlet state is well known but the energy of the triplet is not. The triplet states is hard to

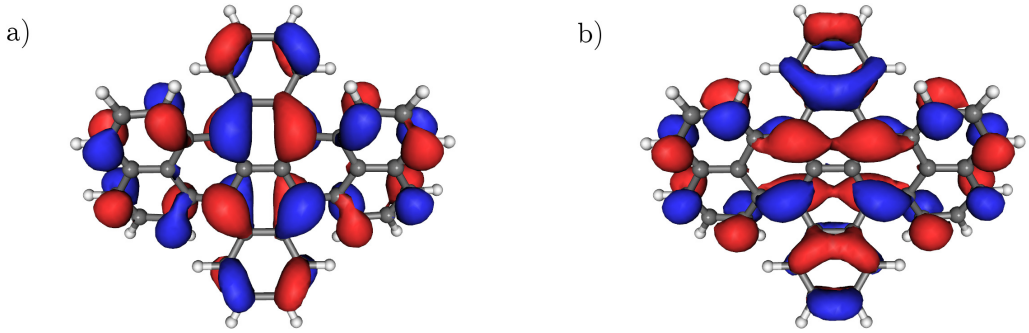


Figure 2.2: DBT orbital electron density: a) The highest occupied molecular orbital (HOMO). b) The lowest unoccupied molecular orbital (LUMO). The orbitals were calculated using DFT in the ORCA package.

detect as transitions from the ground and excited singlet states are spin-forbidden. This gives a small transition rate, induced by the spin-orbit coupling.

DBT has many vibrational modes so that each electronic level has a manifold of vibrational states that it can occupy. These vibrational states can be excited by optical processes in the molecule. They subsequently decay or vibrationally relax to the bottom of the vibrational manifold. This can occur by different processes but these generally involve the creation of phonons or local vibrations in the molecular crystal [80]. This process is frequently called internal conversion. The vibrational modes have been modelled for the free space conformation [74]. Deperasinska measured the vibronic spectra of DBT in naphthalene and 2,3-dimethylnaphthalene and noted a large variation from molecule to molecule and between different hosts. There was however a generally strong vibrational mode at $293\,\mathrm{cm}^{-1}$ wavenumbers shifted from the zero phonon line. This line was also directly observed by Makarewicz *et al.* in anthracene crystals at $290\,\mathrm{cm}^{-1}$ wavenumbers [81]. This corresponds to the 3rd vibrational state that we observe in the low temperature spectrum of DBT in anthracene as a relatively large peak (see figure 3.21 in chapter 3). The other vibronic transitions seen in this spectrum correspond to the vibrational states seen in figure 2.3 labelled as vibronic energy levels. Six vibrational levels can be seen for each electronic level, the second and third levels are so close that they appear as one thick line on this scale. The levels are spaced unevenly and there exists other levels between those shown. The levels shown here are just the ones that can be easily seen in the fluorescence spectrum.

As mentioned before the energy of the triplet is unknown, but it is suspected to be somewhat lower than the level in other PAHs of lower weight [45]. The lowest vibronic triplet energy level in figure 2.3 is taken from predictions made by Deperasinska *et al.* [74] based on the conformation of DBT in *n*-hexadecane where the conformation is similar to that in anthracene.

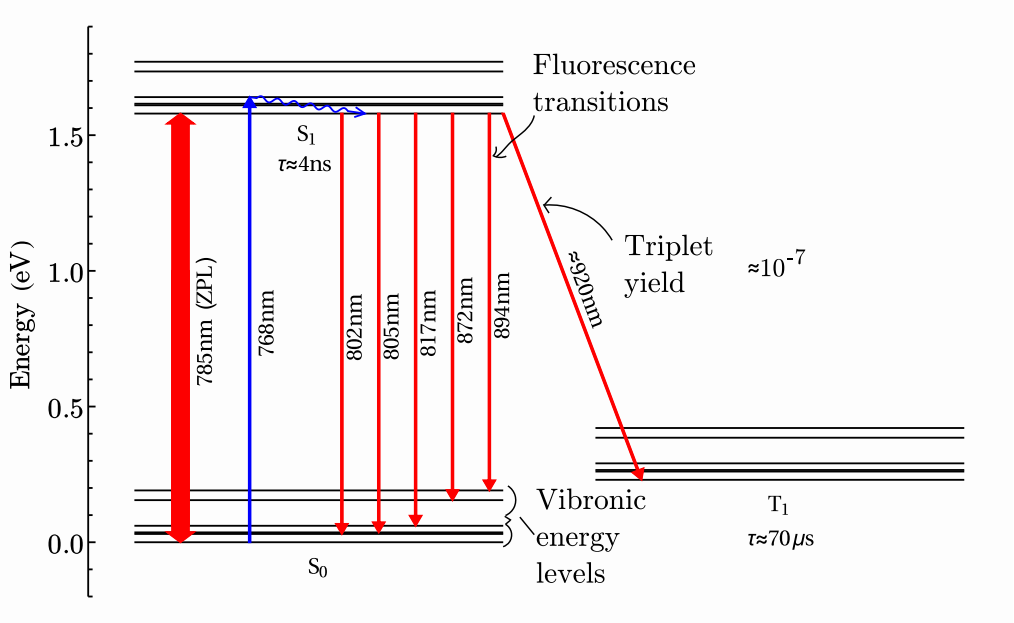


Figure 2.3: An energy level diagram of DBT. Straight arrows show optical transitions and wavy arrows represent nonradiative transitions. Details in the text.

2.3 Optical Transitions

The optical transitions we would like to exploit are shown in figure 2.3. The main transition we intend to use for single photon production is from the bottom of the S_0 singlet band to the bottom of the S_1 singlet band (lifetime, $\tau_1 \approx 4\,\text{ns}$). This transition is known as the zero phonon line (ZPL) and 33% of the time this is how the DBT molecule decays from the excited state [82]. From the bottom of the S_1 band DBT can also decay to higher vibronic states of the ground level singlet mentioned in the previous section ($S_{0,1}$, $S_{0,2}$, $S_{0,3}$, etc. where $S_{x,y}$ is the energy level in electronic state x and vibronic state y). These other transitions emit at longer wavelengths than the ZPL and during much of the confocal microscopy of DBT this is the fluorescence that is collected. Of these transitions the 805 nm is the strongest and corresponds to the transition to the vibrational observed by Deperasinska *et al.* [74] and Makarewicz *et al.* [81] mentioned above.

The molecule may also be excited to higher vibronic levels of the excited singlet. An example of this is shown as the 768 nm transition in figure 2.3, where the excited state is $S_{1,3}$. From this state the molecule relaxes to the bottom of the S_1 band nonradiatively over some picoseconds, as in other PAHs [83]. This fast decay gives the higher vibronic transitions a linewidth that is tens of GHz wide.

At low temperatures, the ZPL transition is lifetime-limited and can be only 32 MHz [55] wide when the molecule is below 4 K. This is due to the large mismatch between the energies of the optical transitions and the phonons in the crystal [84]. As a result the ZPL can only be broadened by two-phonon events which are rare at low temperatures.

As the temperature increases, these two phonon events become more frequent. At high enough temperatures this is the dominant mechanism determining the linewidth and all of the individual transitions are greatly broadened. Also, each transition has a phonon wing that grows as the temperature is increased [74]. This wing is due to optical transitions of the DBT that are accompanied by the absorption and emission of phonons in the anthracene crystal. At room temperature, the transitions from all of the individual vibronic transitions overlap and the emission from a single molecule is many tens of terahertz wide. We need to perform the experiments with single DBT molecules at cryogenic temperatures below 4 K, in order to remove this thermal broadening and collect photons from the narrow ZPL.

To generate single photons we would like to be able to prepare the molecule into the $S_{1,0}$ state with 100% probability. We could achieve this by exciting resonantly on the ZPL with a π pulse. This would prepare the molecule in the excited state but needs to be done resonantly or near resonantly. The excitation light would be hard to separate from the single photons generated unless the excitation pulse was very short compared to the excited state lifetime. Molecules have previously been excited by illuminating the sample with continous wave light and exciting on the ZPL by adiabatic passage [48]. A better way to prepare the molecule into the $S_{1,0}$ state is to excite the molecule to higher vibronic states [49]. Using a pulsed laser, it is possible to excite the molecule at a well defined point in time. By exciting to one of the higher vibronic levels of the S_1 band and then waiting for the molecule to relax to the bottom of the band, the molecule is prepared in the excited state. The ZPL or longer wavelength fluorescence photons will then be emitted over the 4 ns lifetime. As the excitation light is at a shorter wavelength the excitation light can also be spectrally separated from the generated single photons.

As well as the singlet-singlet transition, DBT can also decay to a long lived ($\approx 40\,\mu$s) triplet state. The branching to this triplet state, the triplet yield, is less than 10^{-7} [55]. Optical transitions to the triplet state occur in aromatic hydrocarbons through spin-orbit coupling induced by the out of plane vibrations of the atoms in the molecule [56]. This gives rise to a finite coupling between the singlet and triplet states.

There are also nonradiative mechanisms that can cause transitions between the singlet and triplet states. For instance, the $S_{1,0}$ state can decay to the $T_{1,0}$ state by first transitioning to a highly excited vibronic state of the triplet state $T_{1,n}$, where n is some integer. This is then followed by a multi-phonon transition back down through the lower vibrational states of the final state until it arrives in the $T_{1,0}$ state [56].

When we take images of single molecules, as we will see later, the fluorescence from some of the molecules under continous illumination occasionally stops. This temporary stopping of the fluorescence is termed blinking. The long lifetime of the triplet state is partly responsible for the observed blinking of molecules in microscope images though there are other mechanisms we will consider later.

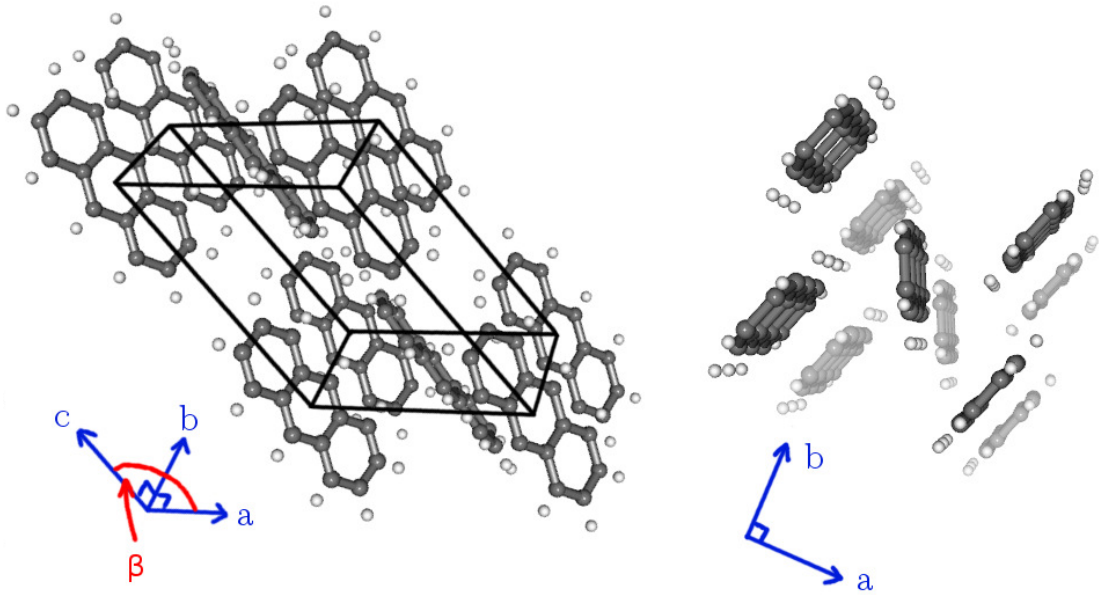


Figure 2.4: Left: A stick and ball model of the unit cell of anthracene. Only carbon bonds are shown for clarity. The angle between the a and c axis is $\beta = 124.7°$. Right: A top view looking down on the unit cell to show the herringbone packing structure. The molecules on the bottom of the unit cell are shown grayed out to distinguish them from those on the top.

2.4 Anthracene Crystals

Many of the ideal features of the DBT molecules that we observe, arise from their being well located in anthracene crystals. Anthracene, the most extensively studied of the organic molecular crystals [85], is composed of just three benzene rings bonded together in the planar structure seen in figure 2.4. It was isolated in 1832 by B. A. Dumas and Auguste Laurent [72] and has been researched primarily as an organic semiconductor with high carrier mobility [86]. Being an attractive material to use for organic electronics, it has been well studied and has well known crystal structure and optical properties.

Anthracene has fluorescent transitions with a very similar structure to DBT but fluoresces in the blue at 400 nm - 500 nm [87]. This is, usefully, far from the excitations in DBT and so the anthracene acts as a transparent host for DBT. The triplet state of anthracene lies energetically above the excited singlet of DBT [88]. This means that excitations of the DBT molecule are mismatched in energy with the triplet excitations of the surrounding anthracene and this nonradiative decay path is restricted.

Anthracene readily crystallises with a monoclinic crystal lattice. This crystal, like most other planar PAH molecular crystals, is held together by Van der Waals attraction between the individual molecules. This is why anthracene has a relatively low melting point $213 - 219°$C [89].

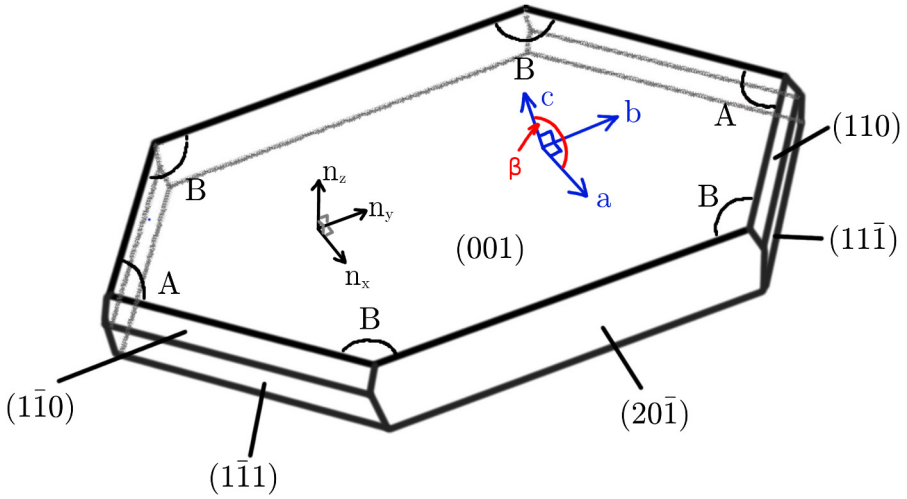


Figure 2.5: A diagram of a crystal of anthracene showing the crystal habit. The crystal axes a, b, and c and the indices of refraction n_x, n_y, and n_z are also shown

The unit cell of the anthracene crystal shown in figure 2.4, is base-centred and orthorhombic with one anthracene molecule at each vertex of the unit cell and another anthracene molecule in the centre of the a-b (001) plane. The central molecule is rotated with respect to those on the unit cell corners, this means the molecules in the crystal adopt a 'herringbone' packing structure which can be seen on the right of figure 2.4. The lattice constants of anthracene along each of the crystal axes a, b, and c are 8.56 Å, 6.04 Å and 11.16 Å respectively [90]. The angle β between the a and c crystallographic axes is 124.7°. The orientation of the individual molecules in the unit cell is such that the vector perpendicular to the plane of the molecule has angles with the a, b and c axes of 36.2°, 115.5° and 66.2°. The vector along the long axis of the molecule then has angles with the a, b and c axes of 119.7°, 97° and 30.6°. The centre molecule forms the same angles with the axes but is mirrored in the a-c plane.

The habit of the crystal that we aim to grow for single quantum emitter experiments can be seen in figure 2.5. This crystal is extensive in the a-b (001) plane and so has the b axis of the crystal lying in this plane [91]. This is consistent with the expected morphology from theoretical considerations of the various surface energies of the crystal faces [92]. For the thin crystals that we grow it is difficult to discern whether the faces (110) or (11$\bar{1}$) and (1$\bar{1}$0) or (1$\bar{1}$1) are present.

The angles formed by the other planes seen in figure 2.5 mean that it is easy to identify the b axis from the angles **A** and **B**. The angle **A** is 109.76° and angle **B** is 125.122°. This is useful for visually determining the dipole direction of the DBT single emitters embedded in the crystal, which lies along the b axis.

Anthracene has three different principal optical axes each with a different refractive index. In order to describe the refractive indices for linearly polarised light we use three orthogonal polarisation axes n_x, n_y and n_z. The n_y axis is parallel to the b axis of the

crystal and the n_x and n_z axes lie in the a-c crystal plane [93]. The values have been measured at 546 nm and are $n_x = 1.570$, $n_y = 1.817$ and $n_z = 2.220$ [94].

2.5 Insertion of Dibenzoterrylene into Anthracene Crystals

When DBT is doped into anthracene, it is located primarily in two sites [60]. In one of those the DBT molecule replaces three anthracene molecules within one crystal plane along the b axis of the crystal, we call this the main site. In the other site the DBT molecule again replaces three anthracene molecules. Two of the molecules are along the b axis in the corners of the unit cell and the third that is in the centre of the unit cell. That is, the DBT replaces three molecules in a triangular arrangement. This is called the red site.

In the main site, the line joining the centres of the two naphthalene moieties of the DBT lies along the b axis, while in the red site it is angled 8° away [60]. So, the dipole of the DBT molecule also lies along or nearly along the b axis. As the crystals grow extensively in the a-b plane the dipole of the DBT molecule then lies in that plane. A molecule in the main site has its optical transitions at or close to the wavelengths described above for the ZPL and the higher vibronic transitions. The red site is so called because the ZPL is red-shifted with respect to the main site to approximately 794 nm. The higher vibronic transitions are all also correspondingly redshifted to longer wavelengths. For most of the experiments below, we will utilise the main site.

Although the DBT molecules occupy well defined locations in their host crystals, single DBT molecules are very sensitive to the local environment [55, 95]. Small environmental differences experienced by each molecule shift the energy levels of the molecule around in the manner of a two-level system. Therefore, the ZPLs of different DBT molecules are distributed over a large range of many tens of GHz compared to their natural linewidth of some tens of MHz.

Nicolet *et al.* have measured the Stark shift of the DBT ZPL in anthracene due to an electric field [60]. Writing the frequency shift as

$$\mathrm{d}\nu = \alpha\mathcal{E} + \gamma\mathcal{E}^2 \tag{2.1}$$

they obtain the values $\alpha = 0 \pm 30\,\mathrm{MHz\ (kV\ cm^{-1})^{-1}}$ and $\gamma = -0.4 \pm 0.5\,\mathrm{MHz\ (kV\ cm^{-1})^{-2}}$ for the main site, and $\alpha = 0 \pm 90\,\mathrm{MHz\ (kV\ cm^{-1})^{-1}}$ and $\gamma = -1.7 \pm 0.8\,\mathrm{MHz\ (kV\ cm^{-1})^{-2}}$ for the red site [60]. In addition, the red site shows a separate population of molecules with $\gamma = -5.2 \pm 1.6\,\mathrm{MHz\ (kV\ cm^{-1})^{-2}}$. Stark tuning makes it possible to adjust the emission frequency of individual molecules. Lettow *et al.* used this feature of dibenzanthanthrene molecules to tune the emission of two separate molecules into resonance so that the emission from the two molecules was indistinguishable [96]. The presence of a quadratic Stark coefficient means that such tuning into indistinguishability is in principle

possible with DBT molecules.

While the DBT molecules are well located in the anthracene crystal, neither the crystal nor the molecule is perfectly rigid. This provides further reasons for the blinking of the DBT molecules seen in confocal scans: conformational changes of the molecule itself and discrete changes in the crystal around it. Spectral 'jumps' of single molecules were observed during the first investigations of pentacene in *para*-terphenyl [41, 42]. This behaviour has been described as being due the presence of two-level systems in the surrounding crystal. These provide a way of simplifying the complex potential energy landscape of the molecule and surrounding crystal, with the two level systems representing transitions between the potential energy minima. In the pentacene in *para*-terphenyl system this has been ascribed to the conformational change in the position of one of the central phenyl rings [97]. But this two-level system description can be seen to describe a variety of changes in the molecule-host system. These sorts of changes are predominantly present in amorphous host materials [98], but they can also be present in crystalline materials like pentacene in *para*-terphenyl described above and DBT in anthracene as well.

DBT is an ideal emitter with attractive properties when located in an anthracene crystal. We can attempt to grow crystals of anthracene doped with DBT to take advantage of these desireable attributes.

CHAPTER 3

GROWING DIBENZOTERRYLENE DOPED ANTHRACENE CRYSTALS

3.1 Crystals

Crystal growth occurs when there is a difference in the chemical potential between two phases of a material where one of the phases is a solid. The difference in chemical potential $\Delta\mu$ is the 'driving force' of the crystal growth [99]. For growth from a melt this may be evaluated in terms of the difference in temperature of the melt region and the solid region. For a solution growth this will be determined by the ratio of the solution concentration and the equilibrium. For growth from a vapour $\Delta\mu$ is determined by the ratio of the vapour pressure, p_{vap}, to the pressure, p, [100]

$$\Delta\mu = \mathrm{R}T \ln\left(\frac{p_{vap}}{p}\right). \tag{3.1}$$

R is the molar gas constant and T is the temperature of the vapour. When this value is positive, the system is said to be supersaturated and crystals grow. When it is negative the opposite happens and the crystal sublimes.

To begin with, small clusters of molecules form but these may dissociate due the finite temperature of the cluster. At some point a cluster forms that is above a critical size and does not dissociate. This initial step is called nucleation. Most nucleation is heterogeneous, meaning that it happens in conjunction with other surfaces or particles. For this reason, the nucleation also depends on the free energy of the surface of nucleation in addition to the chemical potential difference given in equation 3.1.

3.2 Growing Anthracene

I investigated several methods to grow crystals that can be effectively doped with DBT to use in single emitter cavity experiments. Several had problems and were deemed unsuitable, but cosublimation showed promise as a good growth method. In this section, I will

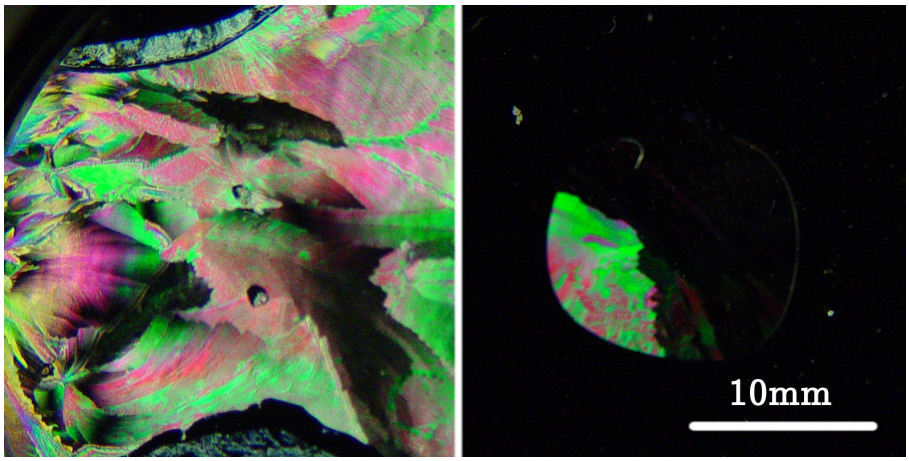


Figure 3.1: A crystal of anthracene grown between two coverslips viewed under crossed polarisers. The sample on the left was not annealed, the sample on the right was. Regions of the same colour are the same crystalline region.

present the various methods investigated before deciding on cosublimation as the most promising method.

Anthracene, as a typical molecular crystal, has been grown from the gas phase for research from as early as the 1930's [101]. However, most of the research of anthracene crystals to date has been on crystals grown from a liquid. The most popular and effective method of growing large anthracene crystals is the Bridgman method [102]. This method uses an oven which has narrow opening in it heated to above the melting point of anthracene. A sealed, usually glass, ampoule containing anthracene inside is inserted into this opening. The anthracene inside the ampoule then melts, forming a liquid inside. The ampoule is then slowly drawn out of the oven. As it is pulled out and cools, the anthracene freezes. By moving the ampoule at a rate comparable to the rate of crystallisation, the anthracene grows into a largely defect-free crystalline material. Manipulating the ampoule geometry by adding constrictions or small tubes can cause a single crystal to dominate inside the freezing anthracene and large single crystals can be grown. Using this method Sherwood and Thompson grew centimetre sized crystals for measuring diffusion coefficients in anthracene [89].

Crystals doped with DBT can be grown directly from the melt and crystals of naphthalene were grown in a microcapillary by Faez *et al.* [53]. They then used the same microcapillary as a nanoguide for light to enhance the interaction with DBT. We attempted growth of DBT doped anthracene crystals by melt growth. Figure 3.1 shows two crystals of anthracene grown from the melt viewed under crossed linear polarisers. One linear polariser is placed after the light source and one before the camera. As anthracene is a birefringent material, it acts as a waveplate on the linearly polarised light passing through the crystal. This means that some light can get through the second orthogonal polariser. The light that passes through the polariser is of a small band of frequencies and

so appears coloured on the camera image. Different regions of the crystal are orientated differently and have different thicknesses allowing different frequencies to transmit and appearing as different colours on the image.

Preparing these samples involved placing several mg of anthracene between two microscope coverslips and placing the two coverslips onto a hotplate set to 240°C. The coverslips were then removed and left to cool at ambient conditions or the hotplate was turned down to 150°C and was left to anneal for 15 hrs. The annealed anthracene grew into large crystalline regions of a millimetre scale. This was confirmed by cross polarisation microscopy, described above, where the different crystalline regions can be observed as different colours. The unannealed sample, shown on the left of figure 3.1, shows regions of the crystal that are largely crystalline but have less defined crystalline boundaries. The large single colour regions also have streaks of other colours running through them and show gradients in colour. The annealed image on the right shows small sections of a more uniform colour and has more clearly defined boundaries between the sections, though this sample is much smaller as most of the anthracene sublimed away after being heated for an extended period of time.

Using this same preparation method, we added a small quantity of DBT mixed with the anthracene. This was done by adding a solution of DBT dissolved in toluene at a known concentration to the anthracene and then allowing the solvent to evaporate. When observing these samples using the confocal microscopy setup described in section 3.5, we found that the DBT dopants aggregated along lines in the samples. The lines are supposed to be the boundaries of the individual crystalline regions on the sample. They could also be defect lines of the anthracene crystal. The higher concentration of molecules at the edges of the crystal regions suggests that as the crystal is growing not all of the molecules are incorporated within the crystal and are held in the still molten anthracene at the edge of the forming crystal. Thus, the molecules aggregate along lines in the sample. This is consistent with previous observations of melt growth causing the dopants to be pushed out of the samples grown in such a way [41].

Unfortunately, this melt growth method permits little control over the position of the individual dopants in the crystal. For cavity emitter experiments we need to be able to guarantee that the crystals we use have an even distribution of DBT molecules, to ensure that there is a molecule in the mode of the cavity. The melt growth method cannot enable us to do this and so is not suitable for cavity experiments.

Other methods of growing anthracene crystals are based on growing from a solution. Spin coating has been shown to be effective in growing DBT doped anthracene crystals [103]. Spin coating involves dropping a solution, in this case anthracene and DBT in toluene, onto a rotating surface. The spinning surface creates a thin and uniform layer of the solution. As the solvent evaporates the solute that is left behind forms thin single crystalline regions. The emitters in spin coated crystals are stable and bright [103]. However, the crystals themselves do not provide full coverage of the surface. Therefore, like

the melt growth method, this method is less than ideal for placing single emitters on a surface. While spin coating is not suited to create the single crystals of anthracene, it is useful as a means of protecting the crystals once they have been grown as we shall see in section 3.4.

Another way of growing crystals from solution is meniscus growth [104], which uses the thin film that is created at the edges of the meniscus when the solution is placed into a container. As the solution evaporates away and the level of the liquid moves down, this leaves a thin layer of anthracene on the surface of the container. I grew anthracene using this method in solution with ethyl acetate. The anthracene was dissolved by heating the solution to 50°C and occasionally agitating it until totally dissolved (2% w/w). I then put a glass slide at an angle into a container filled with the anthracene solution. The solution was left to evaporate at room temperature in a fume cupboard.

Anthracene did form thin films in certain regions of the slide but the surface of the films was not very smooth when the film was analysed with an atomic force microscope. The films also varied in structure at different points on the slide. Only at certain points did the films begin to appear uniform and even then upon closer inspection with an atomic force microscope they were not smooth. I also viewed these crystals under crossed polarisers and was able to identify some regions that were single crystals. However, in general the crystals did not appear as uniform single colour regions.

This may be because the growth was dependent on the concentration of the solution. As the solvent evaporates the concentration of the solution changes. It is the concentration of the solution that determines the difference in chemical potential of the solid anthracene and that in solution and so determines the growth. Simply allowing the solution to evaporate did not allow enough control of the film geometry. A controlled removal of the solution from the vessel could make this method more reproducible. Overall, this method did not produce the good optical quality crystals that we need to be able to maintain the reflectances of the mirror and high finesses of the optical cavities.

After investigation, melt growth and spin coating do not provide enough control of the crystal geometry and the emitter position or concentration to be used reliably for the cavity experiment. Also, the meniscus growth does not form optically good crystals that will not affect the mode of the cavity. This makes these methods unsuitable for the intended cavity experiments. I also investigated the method of cosublimation. Preliminary results showed that this method forms optically good, single crystals that are large compared to those produced by the other methods presented so far. The most appropriate method of growing crystals that are suitable for the cavity experiment is cosublimation. This crystal growth method is presented in the next section.

3.3 Cosublimation

3.3.1 Comparison of previous sublimation methods

Table 3.1 shows a summary of the main parameters of previous methods of growth of anthracene by sublimation. The table compares the different methods, described below, listing the carrier gas or environment that the crystals are grown in along with its pressure, and the temperatures of the anthracene source and collection temperature. It also compares the growth times for the different references and the morphologies of the crystals grown.

Most sublimation growth follows the principles set forth by Lipsett in 1957 using his tube sublimation apparatus [101]. Lipsett grew pure anthracene crystals in a long, cylindrical container, holding a small amount of anthracene powder at the bottom and a metal collector placed towards the top. With the bottom placed into a glass furnace, the anthracene sublimed from the powder and crystallised on the collector which was colder. The growth was in an argon atmosphere at < 1 bar of pressure. The collector is a plate that has a large area for many cyrstals or is much smaller (point sink) to try to encourage nucleation of a small number of crystals. Lipsett's method produces good crystals but does not allow active control of the temperature of the anthracene powder and collection surface. Seeking more control Karl developed plate sublimation.

This alternative method uses two large plates closely spaced in a cylindrical 'cheese box' geometry [105]. The temperature of each surface is independently controlled and anthracene sublimes from the warmer surface and collects on the cooler. Because the top and bottom plates are closely spaced, their temperature difference must be limited in order to avoid substantial heat transfer from one surface to the other. This leads to long growth times.

A flow method has also been used [106]. This uses a heated tube with a temperature gradient along the length of it. Anthracene is placed at the hot end, where there is also a port to allow a carrier gas to enter, while an exit port allows the gas to leave at the cold end. Anthracene crystals of various morphologies collect at different positions along the heated tube.

These crystal growth procedures cover a wide variety of conditions. The pressure varies from vacuum to hundreds of mbar. The temperature of the source varies from 50°C up to 185°C. The temperature difference between this surface and the collection surface ranges from 1°C to 200°C lower. The large range of conditions caused a wide variation in the time it took to grow these crystals. The conditions I finally used for growing crystals, as described below, are at the high end, both in pressure and in the temperature, of the source and collection plate.

Reference	Growth Type	Gas	Pressure/Flow	Anthracene Temp	Collection Temp	Growth Rate/Time	Morphology Width×Thickness
[101]	Tube Sublimation	Ar	133 mbar (below 13 mbar powdery above 293 mbar dendritic)	160°C - 185°C	-	$4-8$ min	hexagonal plates $1\,\text{cm}\times 0.5-1\,\mu$m
[107]	Point Sink	Ar	$6.6 * 10^{-6}$ mbar, 1.3 mbar and 13.3 mbar	$120-145$°C	$1-2$°C lower after nucleation at 10°C lower	Overnight	$1\,\text{cm}\times 1-2$ mm
[94]	Vacuum Sublimation	N_2	1.3×10^{-6} mbar	70°C	-130°C	-	thin films $0.5\,\mu\text{m}-100\,\mu$m
[105]	Plate Sublimation	N_2	1.3 mbar	120°C	9.5°C below	0.1 mm min^{-1}	$1\,\text{cm}\times 1-2$ mm
[91]	Plate Sublimation	-	Evacuated	70.8°C reduced to 54°C	53.35°C	Several days	$100\,\mu\text{m}\times 100\,\mu$m
[106]	Flow Sublimation	He	50 ml/min	160°C	<150°C	-	plates >1 cm
[108]	Tube Sublimation	N_2	2.5×10^{-2} mbar	93°C	<93°C	1.44×10^{-2} mg/hr	plates $100\,\mu\text{m}\times 10\,\mu$m
[86]	Flow Sublimation	He	-	170°C	100°C	24 hr	$1-2\,\text{mm}\times 10-30\,\mu$m

Table 3.1: A table of growth parameters from previous growth of anthracene crystals



Figure 3.2: The sublimation vessel used for initial growth of anthracene crystals.

3.3.2 Vapour Pressure of Anthracene

For all these sublimation methods, the growth rate and crystal morphology are affected by the vapour pressure of the material being grown. The vapour pressure of anthracene has been well studied and has been measured over a large range [109, 110, 111, 112, 113, 114, 115, 116]. The vapour pressure, p_{vap}, can be expressed empirically as an Antoine equation in the form

$$p_{vap} = 10^{\left(A - \frac{B}{T}\right)}. \tag{3.2}$$

The average values of the Antoine coefficients A and B from references [109, 110, 111, 112, 113, 114, 115, 116] are $A = 12.26 \pm 0.05$ and $B = 5190 \pm 20$, with p in Pascal and T in Kelvin. The data used to determine these coefficients is within the range $40° - 215°$

3.3.3 Initial Sublimation of Anthracene

My first growth of anthracene crystals was performed in a glass sublimation vessel after the plate sublimation method of Laudise [106]. This vessel consisted of two parts with roughly concentric profiles separated by a couple of centimetres which formed the source and collection surfaces (figure 3.2). The vessel also had a valved port to allow the influx of gas. A small amount of anthracene was placed on the bottom surface of the vessel, which was evacuated and filled with nitrogen to a pressure of 200 mbar. The vessel was then placed onto a hot plate at 160 °C and anthracene sublimed from the bottom surface and collected on the top surface.

Initially, the anthracene crystals nucleated on the top surface very rapidly and com-

pletely covered the surface which led to a high concentration of crystals and made isolating single crystals difficult. To prevent this, the top surface was initially heated to 60°C with a cartridge heater mounted into an aluminium block. This did produce small, flat crystals but the growth took a long time (several hours). Anthracene also collected on other areas of the vessel. The reason for the long growth time was that the bottom surface would also heat the top surface over time. So the temperature difference between the surfaces decreased during the growth. This suggests the top surface should be actively cooled to allow good control of the temperature difference. It was for this reason that we designed our oven in the way described below. The design of the oven also incorporates a separately heated crucible that can be filled with DBT to dope the anthracene crystals.

3.3.4 Growing Doped Crystals

Ultimately, we wish to grow anthracene crystals that are doped with a known quantity of DBT molecules. The glass vessel used for the intial growth of anthracene crystals had no means of admitting DBT, but a variation on the plate sublimation growth method is suited to growing doped anthracene crystals. Cosublimation was employed to create the first DBT doped anthracene crystals and subsequent studies of their properties[59, 55, 60]. For these investigations, I built a cosublimation apparatus with a similar design to that of Laudise. In addition to the anthracene source, there was an second DBT crucible that was heated with a resistive wire to generate a vapour of DBT molecules. Through active control of the temperature of all of the surfaces in the oven, I was able to control the dopant concentration in a quantitative way. The key to this was control of the DBT vapour pressure through control of the crucible temperature.

3.3.5 Vapour Pressure of DBT

The vapour pressure of DBT has not previously been measured, but we expect it to be low as the molecule is larger than most PAHs. The Knudsen effusion method used to determine lower vapour pressures can only measure down to 10^{-5} torr [115], and the vapour pressure of DBT is many orders of magnitude below this. However, we can make an estimate of the vapour pressure of DBT based on the known vapour pressures of other PAHs. The vapour pressure above solid DBT may also be expressed using other thermodynamic properties. It is derived from the Clausius-Clapeyron equation [117],

$$\frac{dp}{dT} = \frac{\Delta H_s \, p}{\mathrm{R}\, T^2}, \tag{3.3}$$

where ΔH_s is the molar heat of sublimation and R is the molar gas constant. In order to use this for a prediction of the vapour pressure we need to integrate the Clausius-Clapeyron

equation. This produces an expression that has a constant of integration C,

$$p = Ce^{-\frac{\Delta H_s}{\mathrm{R}\,T}}. \tag{3.4}$$

This constant is found using a known vapour pressure at a given temperature. Unfortunately, as was mentioned before the vapour pressure of DBT has not been measured at any temperature.

In the absence of a measurement, we resort to estimating the constant of integration by choosing a reference point and comparing DBT with a range of other PAHs. Let us take the boiling point T_b, at which the vapour pressure above liquid DBT is equal to atmospheric pressure, p_{atm}. In this case we describe the vapour pressure using the heat of vaporisation instead of the heat of sublimation

$$p = p_{atm}e^{\frac{\Delta H_v}{\mathrm{R}}\left(\frac{1}{T_b}-\frac{1}{T}\right)}. \tag{3.5}$$

When the temperature drops below the melting point of DBT we have to consider the effect of the additional heat required to melt the DBT before it evaporates. In order to convert this to the vapour pressure above a solid we need an additional factor containing the heat of fusion, ΔH_f, and the melting point, T_m, [118]

$$p = p_{atm}e^{\frac{\Delta H_v}{\mathrm{R}}\left(\frac{1}{T_b}-\frac{1}{T}\right)+\frac{\Delta H_f}{\mathrm{R}}\left(\frac{1}{T_m}-\frac{1}{T}\right)}. \tag{3.6}$$

We note that generally $\Delta H_s = \Delta H_v + \Delta H_f$. So really equation 3.6 is equivalent to equation 3.4 when C is given by

$$\ln C = \ln(p_{atm}) + \frac{\Delta H_v}{\mathrm{R}}\frac{1}{T_b} + \frac{\Delta H_f}{\mathrm{R}}\frac{1}{T_m}. \tag{3.7}$$

We now have a description of the vapour pressure which depends on four thermodynamic values, which have been measured for many different PAHs. Using these we can make an educated guess about the four values for DBT and then use them to predict the vapour pressure.

We can aid this prediction using the molecular connectivity, which is a measure of how interconnected the atoms in the molecule are [119]. White has shown that boiling point and heat of vaporisation of PAHs are strongly correlated with their molecular connectivities [120]. To first order these are described by the following formula

$$^1\chi_v = \sum_{n,m}\frac{1}{\sqrt{\delta_n\delta_m}} \tag{3.8}$$

where each atom in the molecule is assigned a value δ, which is equal to the total number of bonds connected to that atom (ignoring hydrogen bonds). The bond between atoms n

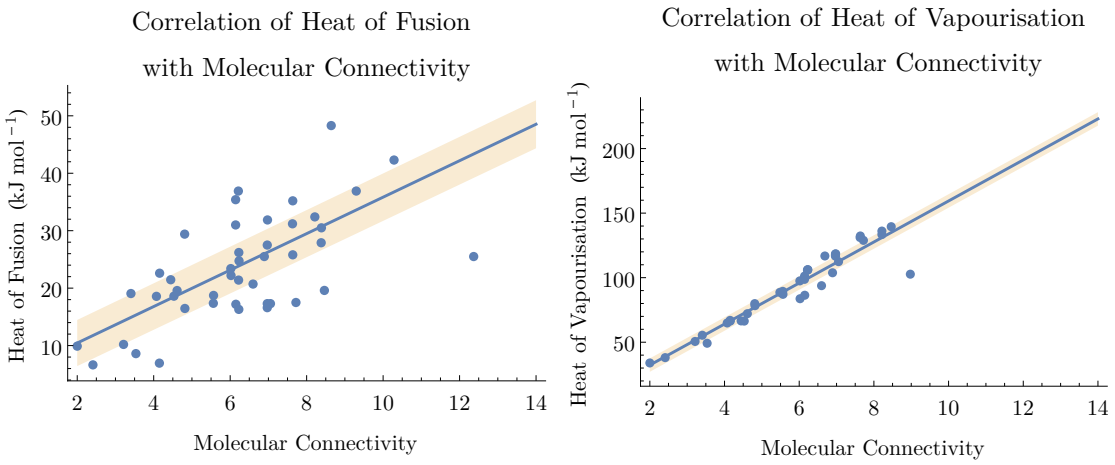


Figure 3.3: The fit of heat of fusion (left) and heat of vaporisation (right) against molecular connectivity, the line shown is the linear fit to the data with the error shown as the shaded band.

and m gives one term in equation 3.8 and the sum is performed over all bonds.

The correlation of the heats of vaporisation and fusion with the molecular connectivity for 39 PAHs are plotted in figure 3.3. The heats of vaporisation are taken from the critical review by Roux *et al.* [121]. By extrapolating to the molecular connectivity for DBT ($^1\chi_v$= 13.4) we estimate the heats for DBT as $\Delta H_v = 213\,\mathrm{kJ\ mol^{-1}}$ and $\Delta H_f = 46\,\mathrm{kJ\ mol^{-1}}$. The boiling point is estimated separately using the US Environmental Protection Agency's EPI suite [122] which utilises the Brown and Stein method giving a value of $1043\,K$ [123]. The melting point has been measured and is $633\,K$ [124]. Now with these four values we can estimate the vapour pressure for DBT as a function of the crucible temperature. The result is heavily dependent on the specific set of molecules that is used to predict the heats of fusion and vaporisation. This is because the predicted value is extrapolated really quite far from the measured values. The vapour pressure of a very large molecule like DBT is difficult to predict and even more sophisticated methods using contributions from the different functional groups have large errors. To try to get an idea of the error the prediction was bootstrapped, that is to say the prediction was made on a sample set from the 39 PAHs by sampling with replacement from the original set. This was repeated 1000 times and the resulting prediction for the vapour pressure is shown as the orange band in figure 3.4 which covers the range within one standard deviation of the mean value.

We can also compare the measured vapour pressure of other PAHs directly. Yaws' Handbook of Antoine Coefficients for Vapor Pressure provides the measured vapour pressures of a large number of aromatics using equation 3.2 [116]. Again, by correlating the Antoine coefficient of the same 39 molecules from before with their molecular connectivity we can predict the Antoine coefficients of DBT. This prediction can also be seen in figure 3.4 as a significantly higher prediction. The error was found using the same bootstrapping

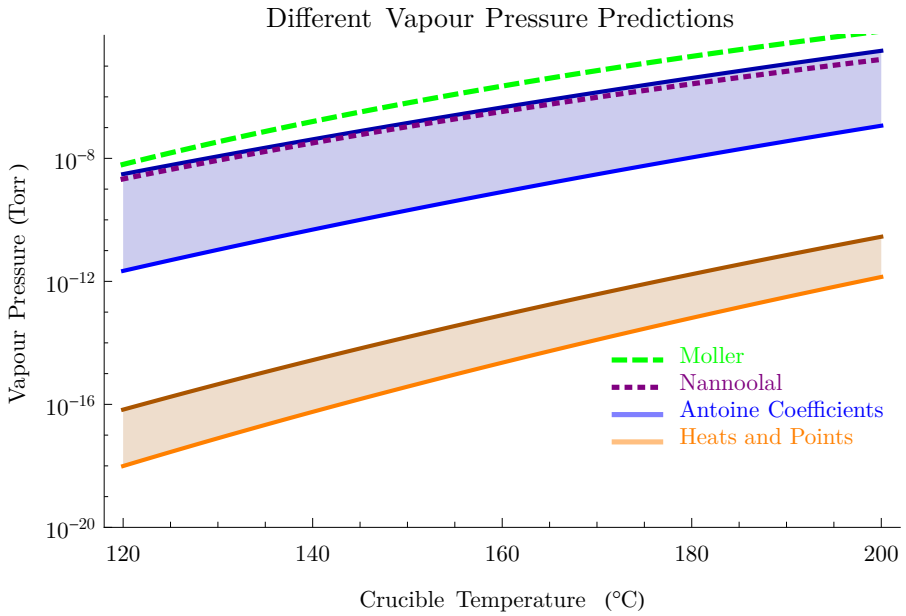


Figure 3.4: Different estimates of the vapour pressure of DBT. The dashed lines are vapour pressures estimated from two different group contribution models [125, 126]. The upper band (blue) is obtained by correlating the Antoine coefficients with connectivity. The lower band (orange) is the estimate obtained from connectivity-correlated heats of vaporisation and fusion, together with the measured melting point and the estimated boiling point.

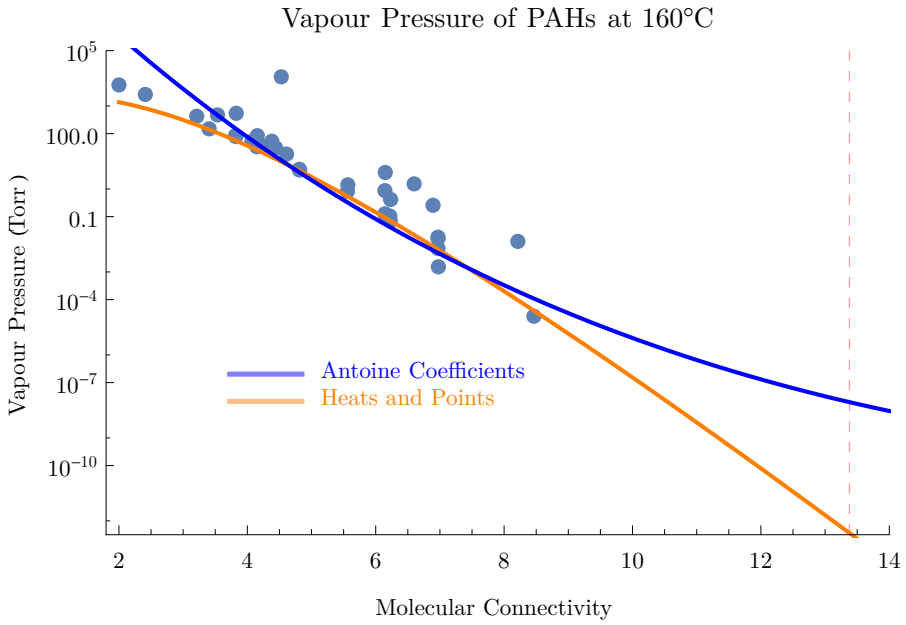


Figure 3.5: The vapour pressure of a various different PAHs at 160°C against their molecular connectivity. Also shown is the predicted vapour pressure at 160°C as a function of the molecular connectivity. The dashed red line shows the molecular connectivity of DBT.

method as before.

A comparison of vapour pressure obtained from these two different estimation methods is seen in figure 3.5. This plot shows the estimated vapour pressure for PAHs at 160°C as a function of the molecular connectivity of these compounds. It also shows the measured vapour pressure for a number of PAH at this same temperature. The plot shows that both methods tend to agree at mid ranges $(4-8)$ of molecular connectivity. The estimation which uses the Antione coefficients begins to overestimate the vapour pressure for molecules with low connectivity. At higher connectivities the estimates diverge substantially until at the molecular connectivity of DBT ($^1\chi_v$= 13.4), denoted by a dashed red line, the two estimates disagree by many orders of magnitude.

Another way to estimate the boiling point and heats, and hence the vapour pressure, is to assess which functional groups are important for determining these quantities. By dividing a large number of molecules into sets containing similar groups the contribution from those groups can be determined. Moller *et al.* and Nannoolal *et al.* provide two different methods for making predictions of the DBT vapour pressure which both use models with group contributions [125, 126]. These estimates, shown with dashed lines, in figure 3.4 are much higher than the predictions which use the heats and transition temperatures, but are closer to predictions made with the Antoine coefficients.

I have the most confidence in the vapour pressure prediction that is based on the measured Antoine coefficients as it is based on measured values and is closer to the group contribution predictions. The doping concentrations of crystals grown from the vapour should be close to the ratio of the vapour pressures of DBT and anthracene.

We would like to have the anthracene source at 160 °C in order to grow optically good crystals of the correct habit. Holding the anthracene source at 160 °C and varying only the DBT source temperature we can vary the predicted concentration i.e. the ratio p_{DBT}/p_{Ac} from $10^{-11}-10^{-7}$ by changing the DBT crucible between 100 °C and 180 °C. This gives a starting point for the design considerations for a crystal growing oven that can control the doping concentration over many orders of magnitude.

3.3.6 Oven Design

Parts of the following section have been published in the August 2015 edition of Review of Scientific Instruments [127].

We wish to grow thin, large anthracene crystals that are optically good and have a well defined concentration. The intention is to place these crystals inside optical fibre microcavities so the crystals must be thin so that the addition of the crystals into the optical cavity does not affect the finesse of the cavity. They must be large because they must be able to be manipulated into the cavity by hand and cover the mode of the light in the cavity. These thin, large crystals adhere to one of the mirrors of the optical cavity by Van der Waals forces and cannot be easily removed without damaging the crystal. So,

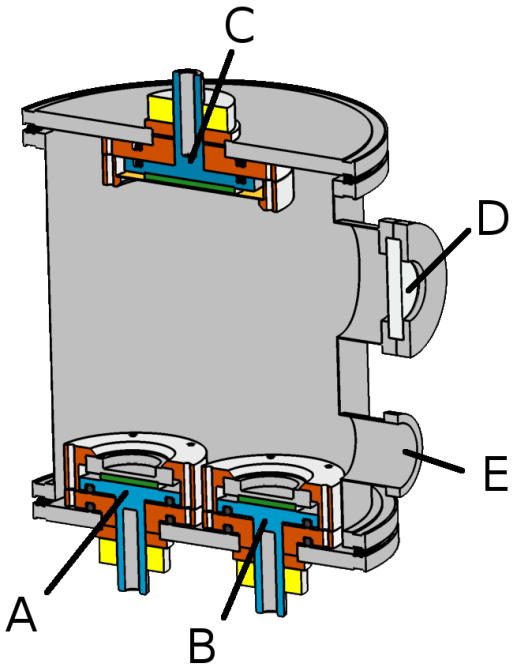


Figure 3.6: Cross-section of the oven design showing the main body with crucible and collection plate assemblies. A: anthracene Crucible. B: DBT Crucible. C: Collection plate. D: View port. E: Vacuum port.

the concentration of emitters must be known in advance because the crystal cannot be initially analysed elsewhere and then transferred into the cavity.

The successful growth of anthracene following the method of plate sublimation means we chose a design which used a large temperature-controlled collection plate on which to grow the anthracene crystals. The anthracene crucible was also temperature-controlled and was separated from the collection plate to avoid the crucible heating the collection plate. From the estimates of DBT vapour pressure above we also needed a second crucible that could be set in the range 100 °C–180 °C.

The oven chamber, illustrated in figure 3.6 is composed of a 30 cm diameter, 30 cm long main body made from 304 stainless steel. At each end two ISO DN250 flanges are welded. These flanges allow two end plates to be mounted, sealed by Polymax fluorinated ethylene propylene encapsulated Viton O-rings. The plates are clamped in place but can be removed to access the interior of the main body. On the bottom plate two holes are drilled to admit two temperature-controlled sources. On the top plate a single hole allows the temperature-controlled collection module to be secured.

The main body also has a 2 3/4-inch Pyrex Conflat view port to allow the collection surface to be monitored during growth. There is also a vacuum port that allows the air to be pumped out and dry nitrogen to be admitted. A pressure gauge (DPG1000B-

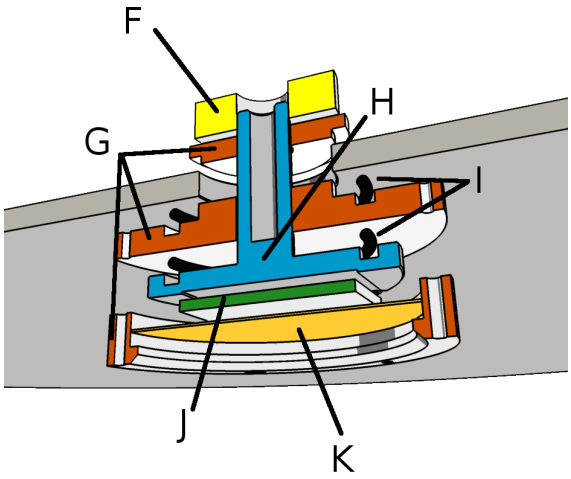


Figure 3.7: Exploded view of the collection plate heating/cooling assembly. F: Water-cooled nut. G: PEEK spacers. H: Cartridge heater holder. I: High temperature O-rings. J: TEC heater/cooler. K: Collection plate.

30V100G, OMEGA Engineering) is attached to the port to monitor the pressure and a valve (SS-8BK, Swagelok) allows the chamber to be isolated from the pump and nitrogen source used to evacuate the chamber. Originally, electrical feedthroughs were placed in the base plate but the rapid thermal cycling at reduced pressure caused the feedthroughs to eventually fail. Instead, a 15 pin D-sub KF50 electrical feedthrough (IFDGG151058C, Kurt J. Lesker) was placed further down the tubing attached to the vacuum port where the temperature variations are not so severe. The main oven body is also wrapped with heating tapes (FGS0031-010, OMEGA Engineering) and covered in fibreglass wool and aluminium foil. This is to raise the temperature of the walls to above 160 °C to prevent deposition of anthracene on other surfaces on the interior of the oven.

The heating and cooling are controlled using a two-stage module. The first stage is used for coarse heating by cartridge heater or cooling with water. The second stage uses a thermoelectric component (TEC) heater/cooler to even out the temperature variations of the first stage. Three of these are used: one as a DBT source, one as an anthracene source and the third as the collection plate. The sources and collection plate are well separated by around 25 cm distance to avoid excessive heat transfer between them.

An exploded view of an individual module is shown in figure 3.7. A water cooled nut (F) is held in place by normal nut that is not shown on the image. Under the nut there are two polyether ether ketone (PEEK) spacers (G) to isolate the heater/cooler assembly from the oven body. The seal against the body of the oven is a high temperature O-ring (I) similar to those holding the end plates onto the main body of the oven. We previously used polytetrafluoroethylene (PTFE) as the material for the spacers. The PTFE spacers

showed a lot of creep when they where being used at elevated temperature and eventually deformed to the point where they did not form a good seal with the chamber body. The cartridge heater holder (H) is sealed to the second PEEK space with another high temperature O-ring, again to hold the inert atmosphere. This forms the first coarse stage of the module and is controlled by a proportional integral derivative (PID) controller (PID 330, Tempatron). The temperature of the first stage is read by a Pt100 resistance thermometer which is attached to the water-cooled nut.

The second stage consists of a heater/cooler thermoelectic component (TEC) (GM250-49-45-30, European Thermodynamics) (J) which is sandwiched between the cartridge heater and the collection plate. Thermal contact to both is ensured with thermal paste (6018, Jelt). The TEC has a much quicker response but can only handle a limited heat flux. The collection plate is a copper disk 0.5 mm thick and 80 mm diameter. The second stage is controlled by another PID controller (PTC 10 K-CH, Wavelength Electronics). The temperature is measured by another Pt100 resistance thermometer which is placed between the TEC and collection plate. For the source assemblies, the copper collection plate is replaced with an aluminium crucible and the Pt100 resistance thermometer is attached to the outside of this crucible.

These assemblies ensure that the temperature variation on the collection plate and the crucibles is less than 0.1 °C. This is a significant improvement over the variation obtained with the cartridge heaters alone which is 3 °C.

3.3.7 Growth Parameters

We began a search for the best growth parameters by looking for the correct temperature of the collection plate and the optimum pressure for growing anthracene crystals. 1 g of anthracene (CAS: 120-12-7, $>$ 99% purity, Aldrich) was placed into the anthracene crucible and the oven closed. Then the oven was pumped out and refilled with nitrogen three times. After a final (fourth) pump down, nitrogen was again admitted to the chamber, bringing the pressure to a measured value, as determined by a gauge referenced to the ambient atmospheric pressure. The latter was also measured to obtain the absolute pressure with an uncertainty of $\pm$10 mbar.

The coarse heater for the top plate was set to around 60 °C below the desired plate temperature with water also running through the cooling block. The heaters for the body and top and bottom plates were also turned on so that the interior surface of the oven reached between 170 °C - 180 °C which varied between different points on the surface.

After 1 hour, to allow the stabilisation of the collection plate and oven body, the anthracene and DBT crucibles were turned on. The anthracene and DBT cartridge heaters were set to 20 °C below the setting for the anthracene and DBT TECs. If the setting of the cartridge heaters was too close to the setting of the TEC, this caused the temperature of the crucible to oscillate. The source TECs were set to 162 °C. During the heating and

growth stages the water cooled nut was not attached to the coarse stage of the two sources.

The crystal morphology we sought is described in section 2.4. To find good conditions for these large flat plates, the starting pressure and the temperature of the collection plate was varied. There were two primary concerns to get crystals to grow correctly. The first was to achieve an ideal density of nucleation, the second was to ensure the plate crystal habit seen in figure 2.5 of the crystals themselves. Both of these depended on the combination of pressure and temperature. It is possible to make some broad qualitative comments about the range of growth parameters. However, these parameters were investigated during the prototyping stage of the oven. Changes in the amount of insulation, repositioning of heaters and temperature sensor etc. make it difficult to make definite comparisons between all of the crystal growths performed.

That being said, nucleation was slower and more sparse at higher collection plate temperatures (up to 130 °C), it became dense at lower temperatures, down to 80 °C. The crystals themselves also appeared granular at starting pressure of below 150 mbar and became increasingly fine and powdery up to 350 mbar. The crystals grew at different rates depending on the temperature of the collection plate with lower temperatures yielding larger crystals in the same growth time. The crystals that grew in flat plates of the habit seen in figure 2.5 grew suspended from the collection plate attached at one vertex. As the temperature was lowered, some of the crystals exhibit striations that resembled the veins in leaves. These ran from some of the other vertices of the crystal to the single vertex at which the crystal attached to the collection plate. As the temperature was lowered below 80 °C the majority of the crystals became so intensely striated that the growth was dendritic.

A starting pressure of 255 mbar with a collection plate temperature of 102 °C consistently yielded a reasonable number of crystals (usually a dozen or so) of several millimetres size in the growth time (1 hr).

Once these conditions had been determined we placed 1.2 mg of DBT into the second crucible and repeated the anthracene crystal growth. Multiple growths were performed while varying only the temperature of the DBT crucible to see what effect this had on the density of the DBT in the anthracene crystals. In order to determine this density the samples were characterised with confocal microscopy as described in section 3.5.

3.4 Crystal Protection

Because the anthracene crystal is held together by weak Van der Waals bonds it has a substantial vapour pressure at room temperature and readily sublimes away. To enable us to spend any substantial time investigating these crystals we must protect them somehow. This was done using spin coating to produce thin films of material that can cover the anthracene crystals while not interfering with the emission from the DBT.

I first tried polymethylmethacrylate (PMMA) dissolved in the aromatic solvent toluene

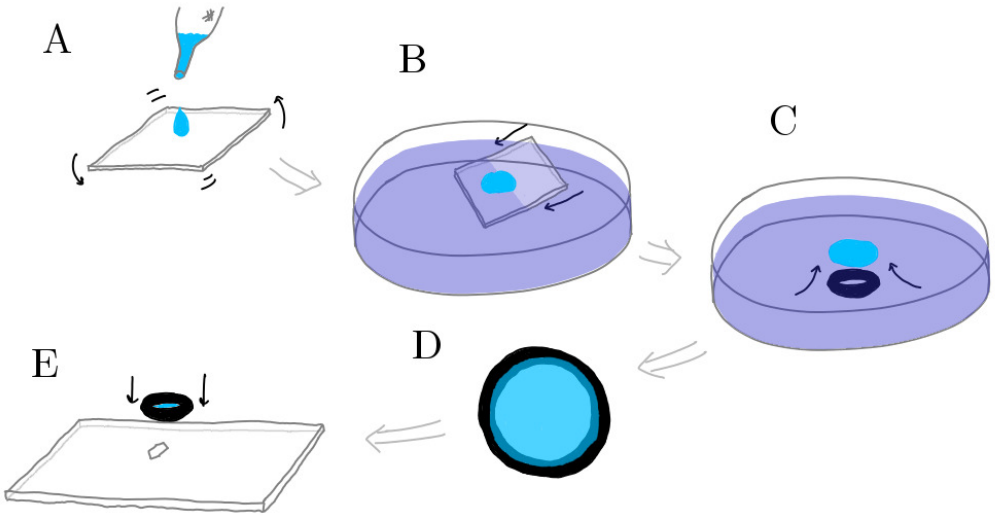


Figure 3.8: The 'cling film' method of overcoating anthracene crystals with PMMA. A: Spin coating a thin film of PMMA onto a coverslip. B: Floating the PMMA film on water. C: Fishing out the film. D Drying procedure. E: Using the film to cover an anthracene crystal.

[128]. However, this solvent also dissolves the anthracene. To get around this, I followed the 'cling film' method that is illustrated in figure 3.8. First, 10 mg/ml of PMMA (445746-25G, Aldrich) in a toluene solution (4 μl) was spin coated onto a clean glass slip at 200 RPM for 200 s (A). This created films of $75 - 100$ nm in thickness and cm extent. The slip was then scored using a scalpel to cut a useful shape. It was then slid into a Petri dish of water (B). The PMMA is hydrophobic and as the level of the water approached the edge of the PMMA the film separates from the glass slip and floats on the surface of the water. The very thin film can then be fished out using a rubber O-ring and allowed to dry in air (C,D). After it had dried, the rubber O-ring had a thin film of PMMA stretched across it that could be stamped onto an anthracene crystal on a glass slip (E). This PMMA 'cling film' cover did protect crystals and slowed the rate of sublimation. The films themselves were very tricky to handle and could easily be perforated.

A more robust protection method used hydrolysed polyvinyl alcohol (PVA) in water. Because anthracene is not very water-soluble this could be spin coated directly on anthracene crystals placed onto glass slips. A solution of PVA (341584-25G, Aldrich) in distilled water (4% w/w) was heated to 80°C for 1 hr to allow the PVA to completely dissolve. The solution was then allowed to cool in a refrigerator and was used directly from the refrigerator. After depositing 10 μl of solution on the surface, the sample is accelerated to 6000 rpm over 5 s and then held at that speed for a further 55 s. This produces thin films of $\approx$ 200 nm thickness. These thin film covers help to protect the grown crystals from subliming away more effectively than PMMA.

The 'cling film' method would be more suited to create fully encapsulated crystals.

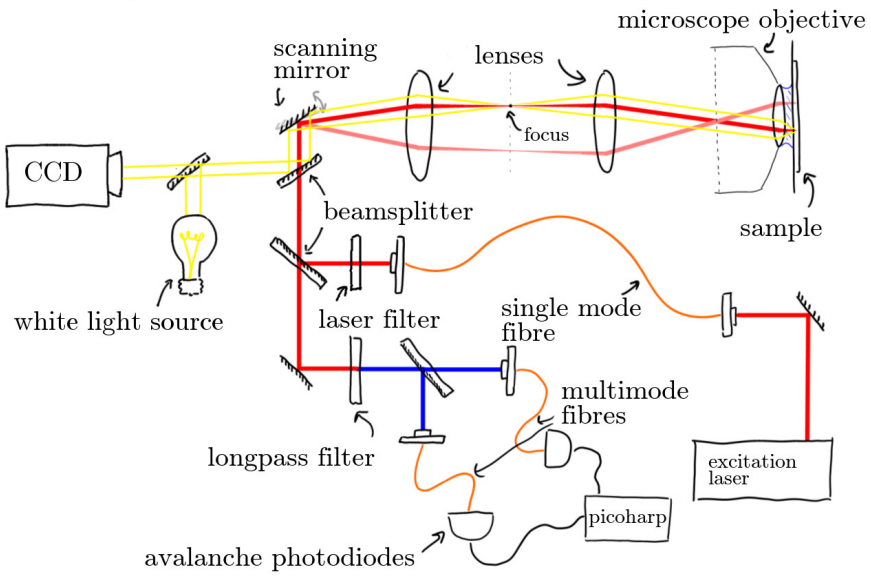


Figure 3.9: The layout of the room temperature oil objective confocal microscope showing the effect of displacing the galvo mirrors to vary the position of the focal spot.

This is a potential method that can extend the PMMA protection I have described above. A base layer of PMMA would have a doped anthracene crystal placed on top of it and then be covered in PVA by spin coating. A second layer of PMMA on top of the PVA would then create an encapsulated crystal that could be floated on water in the same way as the previous PMMA films. This creates a suspended crystal housed in a thin film that could be readily applied to the inside of the optical fibre microcavities and possibly other optical structures.

3.5 Confocal Microscopy

Our DBT-doped anthracene crystals were observed at room temperature under a confocal microscope in order to detect the individual DBT molecules and to measure their density. The setup is seen in figure 3.9. The microscope illuminates the sample using a 779 nm laser (TEC 100 Littrow – Lynx, Sacher Lasertechnik) that is coupled into a single mode fibre (PI-780A-FC-1, Thorlabs). After the single mode fibre the light passes through a laser line filter (FL 780-10, Thorlabs). This filter removes any components of light that are not close to the laser frequency.

One source of this unwanted light is amplified spontaneous emission from the laser diode. Another is additional fluorescence from optical components or coatings. For example, the fibre itself has noise bands due to Raman scattering that can be observed at high excitation powers if not filtered out [129]. A pellicle beamsplitter (BP108, Thorlabs) reflects 10% of the excitation light towards the objective and transmits 90% of the fluorescence returning towards the detectors. The beam is steered by two galvo mirrors through

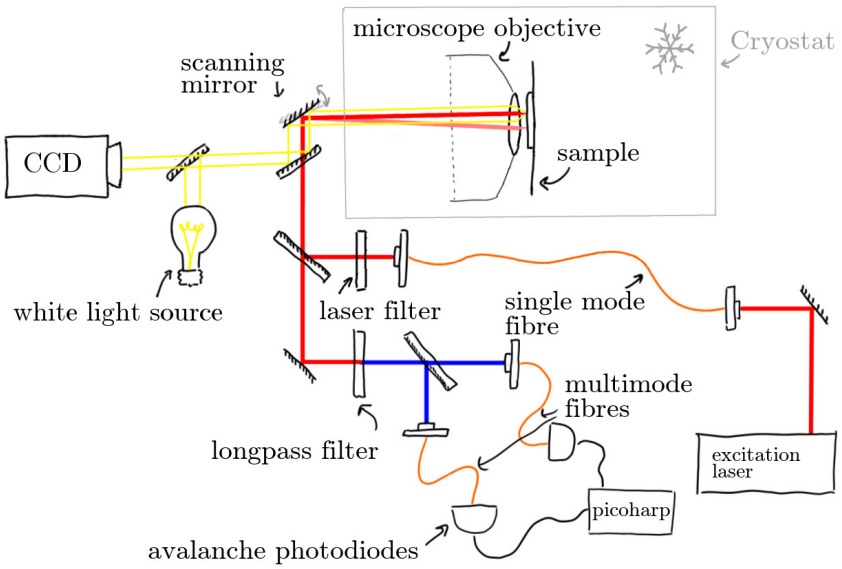


Figure 3.10: The layout of the cold confocal air objective microscope showing the effect of displacing the galvo mirrors to vary the position of the focal spot.

a beam expander and into the NA 1.4 60× oil objective lens (Apo Plan, Nikon). The beam expander lenses are placed such that when the angle of the beam is changed by the galvo mirrors, the position of the beam is still centred on the back focal plane of the objective lens. This lens is placed close to a 170 μm coverslip and the intervening space is filled with index matching oil which reduces the total internal reflection from the coverslip-air interface, increasing the numerical aperture to 1.4. The sample is placed on the opposite side of the microscope coverslip. The collimated beam is focussed to a FWHM 428 nm spot whose position on the sample is controlled by the galvo mirrors. The coverslip is attached to a larger microscope slide that is held onto a slide mount on top of a 3-axis NanoMax stage (MAX313D, Thorlabs), this allowed the fine adjustment of the focus and x and y position of the sample.

The fluorescence from the sample then passes back through the same optics, and transmission through the beamsplitter is conditioned by a longpass filter (LP800HQ, Chroma) that removes the laser excitation light from the signal. The fluorescence is then coupled into two multi mode fibres (GIF 625, Thorlabs) which act as spatial filters for any light that is not focussed and thus discriminate in favour of fluorescence from within the focal spot on the sample. The fibres are connected to two avalanche photodiodes (APD) (SPCM-AQRH-15-FC, Perkin-Elmer) which record the fluorescence from the sample.

For cryogenic images of the molecules, we used another confocal microscope, sketched in figure 3.10 that was built with a similar design to the room temperature confocal microscope (Figure 3.9). The cold microscope sent the laser directly into the air objective after reflecting off of the galvo mirrors. This simplifies the optics, but at a slight cost. When the angle of the galvo mirrors is large, the beam is clipped by the back aperture of

the objective lens reducing the intensity of the light falling on the sample and vignetting the final image. Both the objective and the sample are placed inside a closed cycle cryostat (Cryostation, Montana Instruments). Within this cryostat, the objective is held at 300 K by heaters. This allows the sample to be very close to the objective and permits the objective to have a high numerical aperture (EC Epiplan-Neofluar NA 0.9 100×). The spot on this microscope has a FWHM of 555 nm. The sample is separated from the objective by a radiation shield that is held at 30K. The radiation shield has a 2 mm hole to let light from the molecule into the room temperature objective. For cold images, the molecules were excited with a Ti:Sapphire laser at 770 nm or 785 nm using either FB770-10 or FL780-10 (Thorlabs) laser line band pass filter. The long pass filter was then either a XRLP792 or a HQ800LP (Thorlabs). The x, y and z positioning of the sample was achieved by using a 3-axis slip-stick positioner (3× ANPx101, Attocube). Thermal contact to the cold head of the cryostat was achieved using a beryllium copper sample mount that has a flexible link connecting the cold platform inside the cryostat to the sample holder mount on the top of the attocube positioner. This ideally means the sample, at a temperature of 3.2 K, can be positioned relative to the objective lens using the attocubes. The sample was usually mounted onto a glass slip, overcoated with PVA, then placed top of the sample mount with a small amount of thermal N grease (Apiezon).

An image can be constructed in either of the confocal microscopes, by scanning the laser across the sample and recording the fluorescence counts on a single APD, as is seen in the top face of the cube in figure 3.11. The image shows single molecules as bright spots on a scan in x and y. The other images on the side of the cube show scans in x and z and also y and z. The focal spot is extended in the z direction. Well defined foci can be seen in a narrow band in the centre of both of these scans. This band corresponds to the thickness of the crystal and the region in which a good x-y image is formed. The brightest streak seen in the x-y image is a crack in the crystal. This can been seen in the white light CCD image shown on the left figure 3.11. The crack is the source of increased scattering. Laser light falling on to this point scatters into the crystal and excites many molecules. The fluorescence is then rescattered back into the collection optics. The picture is built up of multiple scan lines across the whole image. A close-up of one region is seen in the inset on the right of figure 3.11. The effect of blinking can be seen in this image, as indicated by a red arrow. A molecule has briefly been driven into a dark state during the scan and this is seen as a dark streak in the image due to the line by line way in which the image is built up. By setting the galvo mirrors to sit on one single molecule, the second-order correlation, $g^{(2)}(\tau)$, of the emission from this molecule can be be measured as described in more detail in section 3.6.

Alternatively, the fluorescence is sent to a Shamrock 303i grating spectrometer (Andor) with a cooled electron multiplying CCD (Newton, Andor). This can detect the very low emission levels from a single molecule.

To calibrate the transverse dimensions of the scan the laser was heavily attenuated

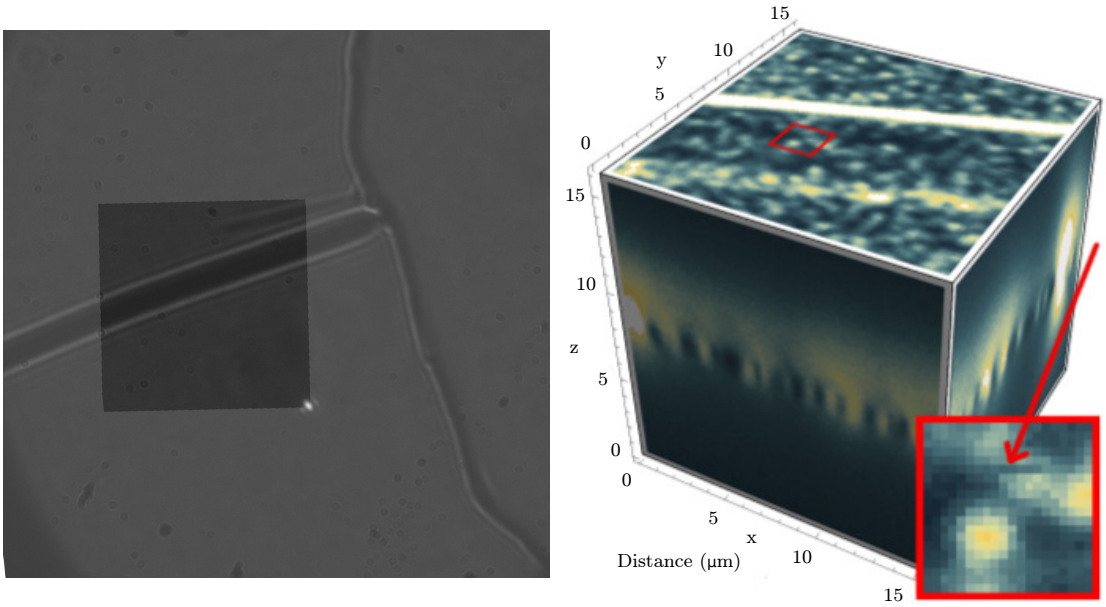


Figure 3.11: Left: A white light optical image using a CCD camera of the crystal that is imaged in the confocal microscope. The scan area is highlighted by a dark square. The attenuated laser spot can be seen in the bottom right hand corner of the square. Right: A room temperature confocal scan in x, y and z of $16 \times 16 \times 16\,\mu\text{m}^3$ volume of anthracene crystal doped with DBT. The xy scan was taken at z= 7.5, the xz scan was taken at y= 0 and the yz scan was taken at x= 15. The inset shows the area highlighted on the x and y scan showing a dark streak left by a molecule that has blinked off indicated with an arrow.

and the longpass filters removed from the collection path. A nickel calibration grid was placed on the cover slip and could be imaged in the same way as the single molecules. The scan range was typically $10 - 20\,\mu$m along x any y and the spot size was measured as a Gaussian spot with FWHM of 428 ± 10 nm on the room temperature oil objective and FWHM of 555 ± 9 nm on the cold confocal air objective.

3.6 Sample Characterisation

The crystals grown in the oven were imaged using both the room temperature and cold confocal microscopes. The first step was to characterise the doping density of the crystals as a function of the DBT crucible temperature. The thickness of the crystals was determined by an atomic force microscope (Nanoscope Dimension 3100) at various points (typically 3-5) around the edge of the crystal. The surface roughness of the crystals varied from crystal to crystal but was measured to be in the range $1 - 3$ nm, though this is close to the resolution limit of the microscope. These crystals were then overcoated with PVA as described in section 3.2. The room temperature confocal microscope produced images with single bright spots that were easy to count by hand. If the number of molecules was low, several images were taken. The ratio of DBT molecules to anthracene molecules was

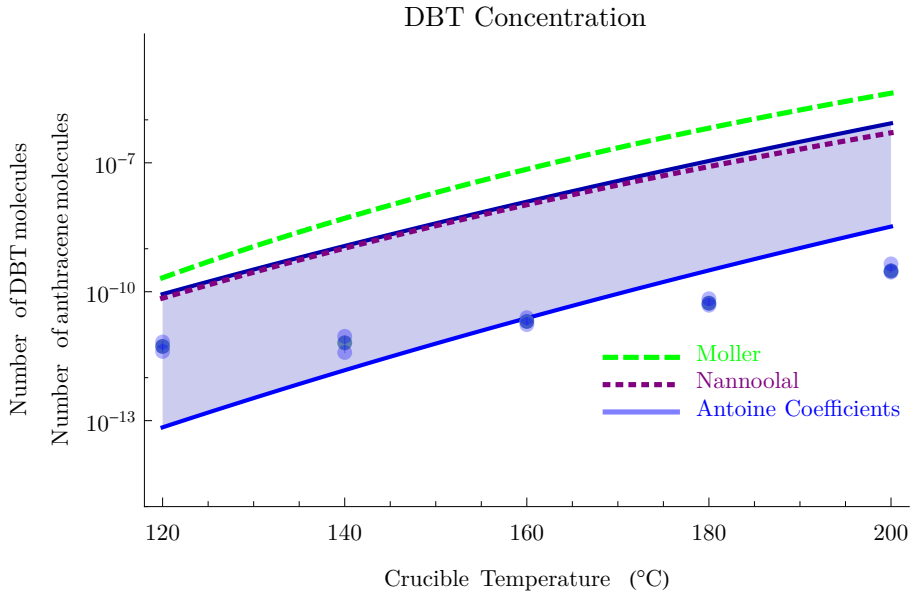


Figure 3.12: DBT concentration versus temperature. Blue circles show the measured concentrations. Lines show predictions from the various sources mentioned in section 3.3.2 (with prediction from heats and, boiling and melting points omitted).

then determined by estimating the number of anthracene molecules in the image volume. The number of anthracene molecule per unit volume is

$$\frac{N}{V} = \frac{\rho \mathcal{N}_A}{m_A} \tag{3.9}$$

where the density, ρ, is 1.28 g cm^{-3}; the molecular weight of anthracene, m_A, is 178.229 g mol^{-1} and $\mathcal{N}_A$ is Avogadro's number [130]. This gives 4.33×10^9 molecules per μm^3. The results of these measurements are plotted as blue circles in figure 3.12.

In an effort to consider what doping concentrations we might expect, we first estimate the arrival rates of the two different molecules at the collection plate. The number density of molecules in the gas above the individual crucibles (dropping constants as we are only interested in a ratio) is

$$n \propto \frac{p}{T}, \tag{3.10}$$

with n being the number of molecules and P and T, vapour pressure and temperature respectively. The flux of molecules, N, leaving a surface area, A, of the substance in the crucible is proportional to nAv, where v is the velocity of the molecules. Again dropping constants

$$v \propto \sqrt{\frac{T}{m}}, \tag{3.11}$$

with m being the mass of the molecule. Now combining equations 3.10 and 3.11 for each of the molecules and dividing one by the other we arrive at a ratio of the rates for production for the two species of molecule (Ac denotes anthracene):

$$\frac{N_{\mathrm{DBT}}}{N_{\mathrm{Ac}}} = \frac{p_{\mathrm{DBT}} A_{\mathrm{DBT}} \sqrt{m_{\mathrm{Ac}} T_{\mathrm{Ac}}}}{p_{\mathrm{Ac}} A_{\mathrm{Ac}} \sqrt{m_{\mathrm{DBT}} T_{\mathrm{DBT}}}}. \tag{3.12}$$

The vapour pressures were addressed earlier in section 3.3.2. We estimated the area ratio of DBT:anthracene by photographing the two crucibles and measuring the areas seen in the two photographs. This gave a ratio of 6:100. The masses are 178.229 g/mol for anthracene and 476.565 g/mol for DBT [130]. This allows us to estimate the ratio of DBT to anthracene we expect. These are plotted in figure 3.12. The green dashed line assumes the DBT vapour pressure estimated using the group contribution method of Moller *et al.* [125]. The purple dashed line assumes the different DBT vapour pressure given by the group contribution method of Nannoolal *et al.* [126]. The blue band assumes the DBT vapour pressure found by correlating the Antoine coefficients of other PAHs.

At the lowest DBT crucible temperature the measurement sits in the middle of these estimates, but we do not see the concentration increasing as rapidly as expected when the temperature is increased. We can think of three reasons for this: (i) the counting of individual molecules is inaccurate, (ii) the DBT molecules are not always incorporated into the crystal and (iii) the DBT is not arriving at the collection plate.

Firstly, it may be that at low concentrations the measurements are counting other things in the crystal that are not molecules. This would cause an artificial levelling out. That possibility could have been avoided by making $g^{(2)}(\tau)$ measurements on all the bright spots that we counted as molecules, but this was not done. Also, at higher densities we should expect to undercount the number of molecules because of the likelihood of having more than one molecule located within the same focal spot. This error will ultimately limit the concentration that can be measured at room temperature to $\approx 10^{-9}$. Because the concentrations we observe are well below that level, we do not think this can explain the discrepancy in figure 3.12.

Possibility (ii) is that the DBT molecules may only locate with less than unity probability. The DBT molecule is substituted for three anthracene molecules in the crystal and may only be incorporated into the crystal if it finds an ideal location. This may be thought of as a surface diffusion process. The DBT molecule will diffuse across the surface until it finds a location at which it will be fully incorporated into the crystal. This incorporation is likely to be at steps on the crystal face, with the step originating from dislocations that form spontaneously in the crystal [131]. This type of crystal growth has been observed in anthracene grown by physical vapour deposition [132]. So, the DBT molecule is competing with the anthracene molecules to become part of the crystal. Diffusion processes generally follow an Arrhenius equation with temperature. Depending on the relevant activation energy this rate of this process could vary with temperature. This could mean that the

rate at which the DBT molecules are arriving at the crystal is not the concentration that is found in the final crystal.

The third explanation is that as the temperature is increased, the DBT molecules are likely to adsorb onto the other surfaces of the oven that are at a lower temperature. This means that not all of the DBT generated at the DBT crucible is making it to the collection plate and the predicted concentration is too high.

It must also be remembered that the DBT vapour pressure used to predict the concentration is an estimate. Without an independent measurement of the DBT vapour pressure, it is not possible to elaborate further on the theory. Whatever the explanation for this discrepancy may be, the main point here is that we can vary the concentration of DBT by a factor of ten over a useful range, while producing crystals of high optical quality.

When the DBT is properly incorporated into the anthracene crystal, the molecules are known to be orientated along the b axis [60]. To confirm the orientation of DBT molecules the confocal microscope was modified so that the polarisation of the excitation light could be varied. The DBT molecule is most efficiently excited when the polarisation of the excitation light is aligned with the optical dipole moment of the molecule. By rotating the polarisation of the excitation light and monitoring the fluorescence of the molecule we can determine when the polarisation is aligned with the dipole and so measure its orientation. A half-wave plate was placed in the excitation path of the confocal microscope and rotated to vary the polarisation. Some of the optics in the microscope were also sensitive to the polarisation of the light. The pellicle beamsplitters in particular were found to vary in reflectance depending on the polarisation. To account for this a glass plate was also placed just before the microscope objective in order pick of some of the excitation light and direct it onto a photodiode. This allowed us to monitor the power falling on the sample and normalise out the power fluctuations due to any optical components. As the orientation of the molecule is fixed the emission is not subject to any such variation.

Confocal images were taken at 10° intervals in the polarisation orientation. From each of these images we identified individual molecules and plotted fluorescence intensity from each molecule against the angle of the polarisation of the excitation light. This trace was normalised using the photodiode that monitored the power landing on the sample. An example of this normalised trace is seen in figure 3.13. The variation is fitted to the function

$$A\cos^2(\theta+\phi)+C. \tag{3.13}$$

A gives the amplitude of the oscillations seen in the images and ϕ is the angle between our arbitrary zero of θ and the alignment direction of the anthracene's crystallographic b axis. The constant C accounts for the background counts not coming from the fluorescence of the molecule. The measured values of A, which have been normalised against the

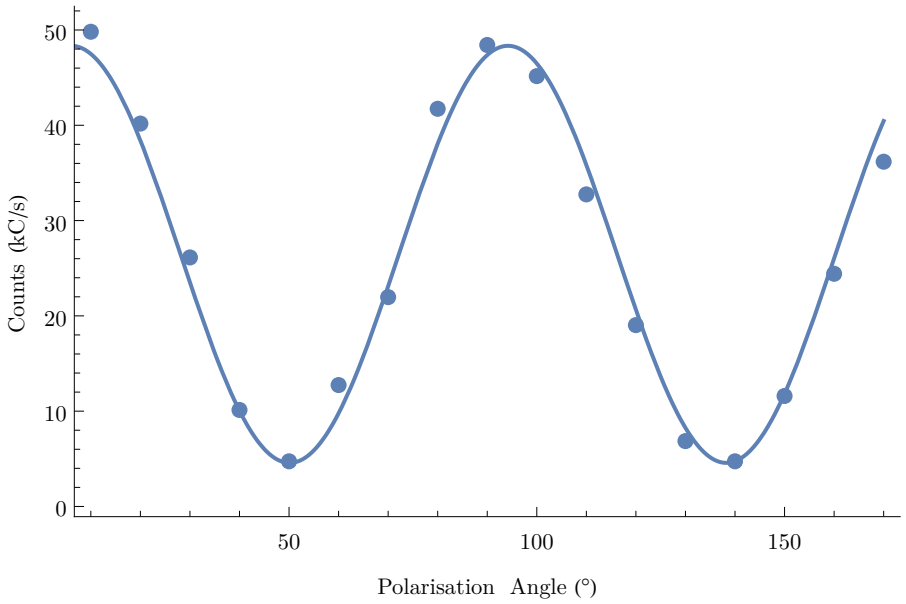


Figure 3.13: A trace of the fluorescence from a single molecule as the excitation polarisation is varied.

brightest molecule, and ϕ are shown in a scatter plot in figure 3.14. Also shown, are histograms of intensity and orientation individually. The b axis which was determined by observing the crystal through an optical microscope and noting the angles that the crystal faces formed is at $\phi = 0$. The b axis bisects the smaller of the two angles formed by the crystal edges (See figure 2.5). The scatter plot shows that the brightest molecules are well aligned with the crystallographic axis.

This is consistent with other observations of the dipole orientation of DBT in anthracene [60]. Nicolet *et al.* see the dipole of the molecule aligned with the b axis for molecules in the main site and also measure a small deviation of the dipole for molecules in the red site of DBT in the crystal. This is because the molecule is orientated at a small angle with respect to the b axis. We do see a second peak at $-8°$ though it is not completely convincing. The molecules that are not so aligned with the b axis are also the molecules that are not as bright. In fact, there are two well established peaks in the intensity histogram. The peak absorption of the red site is shifted to longer a wavelength. The reduction in intensity could be due to the fact the these molecule are not absorbing and thus emitting as many photons. To confirm this, the same orientation experiments should be performed at cryogenic temperatures where the two sites can be resolved spectrally.

As well as alignment of DBT molecules, we also investigated the saturation of the molecules in the anthracene crystal. This was performed by moving the microscope galvo mirrors to isolate one single molecule and recording the fluorescence while the excitation power was varied. An example of a trace for a single molecule is seen in figure 3.15. The intensity is determined by measuring the power before the objective lens. The spot on the sample has a FWHM of 555 nm and the spot is very close to Gaussian. This gives an

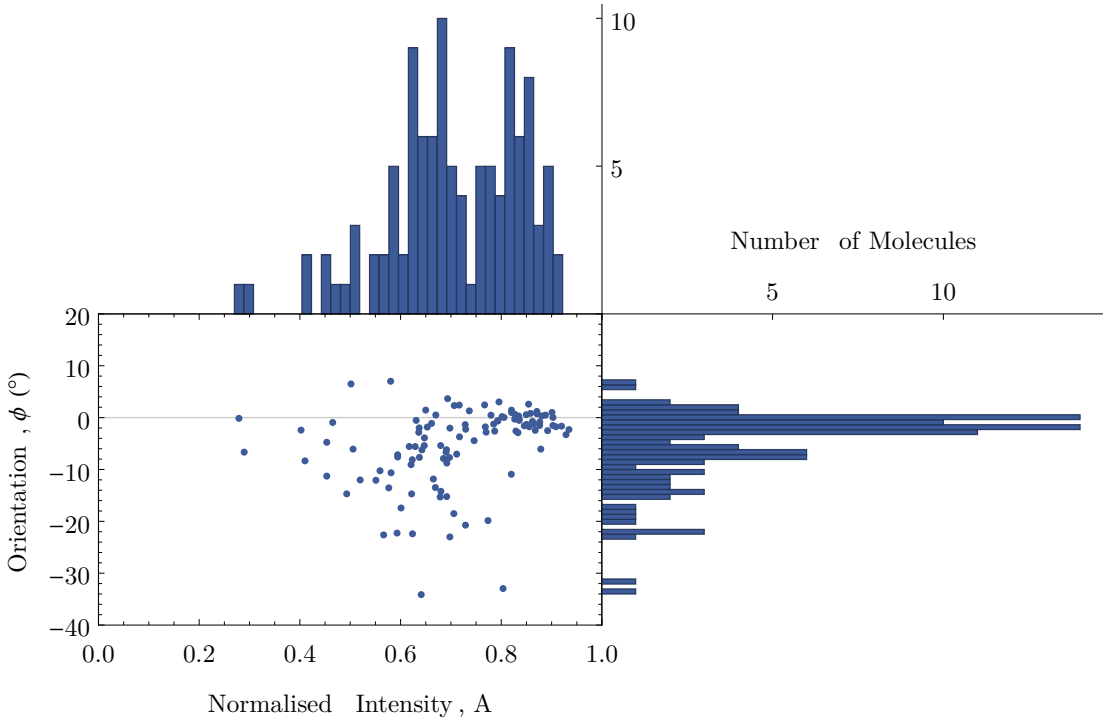


Figure 3.14: Scatter plot of the normalised maximum intensity and the orientation relative to anthracene b axis for 113 DBT molecules. Histograms of each parameter are shown on the edges of the plot.

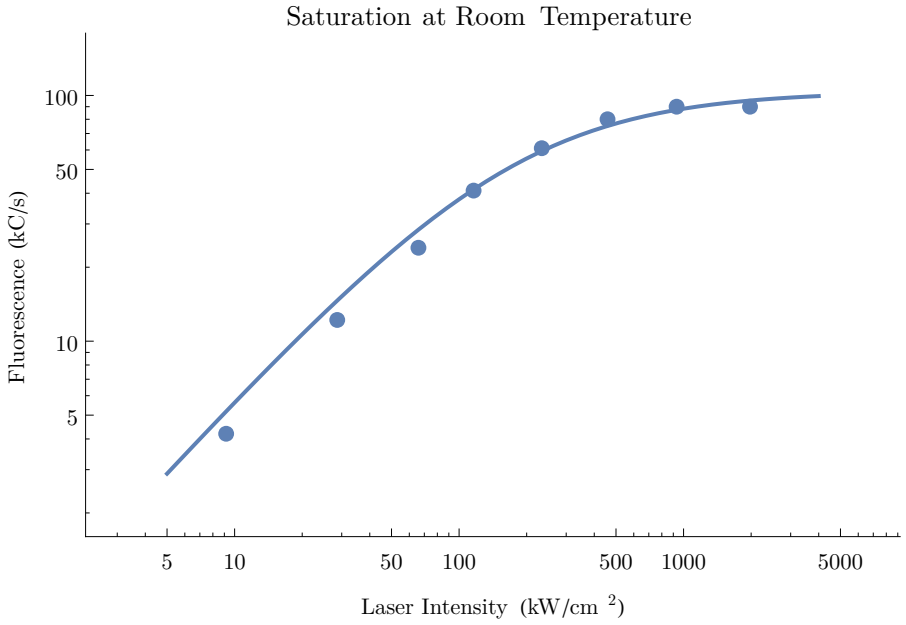


Figure 3.15: A saturation curve for a single molecule at room temperature, $I_{sat} = 170 \pm 20\,\mathrm{kW/cm^2}$.

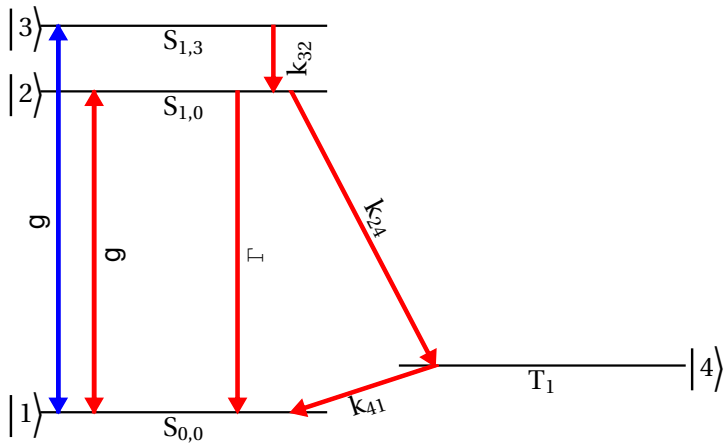


Figure 3.16: A simplified energy level diagram of DBT for the three level model of $g^{(2)}(\tau)$.

intensity at the centre of the spot of

$$I = \frac{2P}{\pi \left(\frac{FWHM}{\sqrt{2\ln(2)}} \right)^2}. \tag{3.14}$$

A curve fitted to the data has the form

$$R = R_\infty \frac{I/I_{sat}}{1 + I/I_{sat}}, \tag{3.15}$$

where R is the (detected) fluorescence rate and R_∞ is the saturated rate of fluorescence. I_{sat} is the saturation intensity, found in this experiment to be $170 \pm 20\,\mathrm{kW/cm^2}$. The value of R_∞ is 103 ± 4 kcounts/s and is the maximum (detected) emission rate from the molecule in the limit of infinite excitation power. The fact that this molecule saturates indicates that we are indeed dealing with a quantum emitter, but to be sure we would like to investigate the second order correlation of the light. The exact form is more complicated than was presented earlier in section 1.1, so I will take a slight digression here to describe the true form of the correlation.

The $g^{(2)}(\tau)$ described in section 1.1 is the second order correlation observed from an ideal two level system acting as a weakly driven single emitter. The more complicated level structure and environment of the DBT molecule modifies the $g^{(2)}(\tau)$ that we actually observe. When the molecule is cold and the individual vibronic transitions are well separated, the observed correlation function depends on which level the molecule is excited to. Also, the presence of the triplet state has an effect. Figure 3.16 shows the levels that we consider in deriving a more detailed theory of $g^{(2)}(\tau)$. The ground state, $|1\rangle$, corresponds to the $S_{0,0}$ state. We can excite the molecule on the ZPL to level $|2\rangle$ or to a higher vibronic state, $|3\rangle$, which correspond to the $S_{1,0}$ state and the $S_{1,3}$ state. The triplet state is level

$|4\rangle$. Γ is the decay rate of the ZPL transition and the other single headed arrows shown are the population decays from other excited states. The double headed arrows show the two possible excitation methods, red on the ZPL and blue to the $S_{1,3}$ level. These two excitation schemes will be solved separately.

The $g^{(2)}(\tau)$ gives the average probability of successive photons being emitted from the molecule with a time seperation τ. After a photon has been emitted on the ZPL the molecule is prepared in the ground state. The emission of another ZPL photon can only occur when the molecule is re-excited to $|2\rangle$. We can then find the form of the $g^{(2)}(\tau)$ by solving the driven optical Bloch equations for this system to find the population of $|2\rangle$ [133]. The optical Bloch equations are given in terms of the density matrix, $\boldsymbol{\rho}$, of the system. For resonant excitation, on the $|1\rangle - |2\rangle$ transition, the optical Bloch equations are:

$$\dot{\boldsymbol{\rho}}_{22} = -\Gamma\boldsymbol{\rho}_{22} - k_{24}\boldsymbol{\rho}_{22} + ig(\boldsymbol{\rho}_{12} - \boldsymbol{\rho}_{21}), \tag{3.16}$$

$$\dot{\boldsymbol{\rho}}_{11} = \Gamma\boldsymbol{\rho}_{22} + k_{41}\boldsymbol{\rho}_{44} + ig(\boldsymbol{\rho}_{21} - \boldsymbol{\rho}_{12}), \tag{3.17}$$

$$\dot{\boldsymbol{\rho}}_{12} = -\Gamma_2\boldsymbol{\rho}_{12} + ig(\boldsymbol{\rho}_{22} - \boldsymbol{\rho}_{11}), \tag{3.18}$$

$$\dot{\boldsymbol{\rho}}_{21} = -\Gamma_2\boldsymbol{\rho}_{21} + ig(\boldsymbol{\rho}_{11} - \boldsymbol{\rho}_{22}), \tag{3.19}$$

$$\dot{\boldsymbol{\rho}}_{44} = k_{24}\boldsymbol{\rho}_{22} - k_{41}\boldsymbol{\rho}_{44} \text{ and} \tag{3.20}$$

$$\boldsymbol{\rho}_{11} + \boldsymbol{\rho}_{22} + \boldsymbol{\rho}_{44} = 1. \tag{3.21}$$

Γ_2 is the decay rate of coherence between the $S_{0,0}$ and $S_{1,0}$ levels. g is the coupling between the molecule and the driving field which is half the angular Rabi rate of the interaction with an oscillating driving field $\hbar g = -\frac{1}{2}\langle 2|\hat{\mathbf{d}} \cdot \mathbf{E}|1\rangle$. In order to find the saturation parameter $S = \frac{I}{I_{sat}}$, we solve the optical Bloch equations in the steady state by setting all of the time derivatives to zero. This gives and expression for the population $\boldsymbol{\rho}_{22}$ as

$$\boldsymbol{\rho}_{22}[\tau \to \infty] = \frac{2g^2k_{41}}{2g^2k_{24} + 4g^2k_{41} + \Gamma_2k_{24}k_{41} + \Gamma\Gamma_2k_{41}}. \tag{3.22}$$

In the limit of large g this then becomes

$$\boldsymbol{\rho}_{22}[\tau \to \infty]\big|_{g\to\infty} = \frac{k_{41}}{k_{24} + 2k_{41}}. \tag{3.23}$$

This is the maximum population that can be driven into level $|2\rangle$. The expression for the emission on the ZPL is the product of the maximum emission rate and $\frac{S}{1+S}$, where S is the saturation parameter. The maximum emission rate is Γ times the maximum probability that the molecule is in the state $\boldsymbol{\rho}_{22}$ which is $\boldsymbol{\rho}_{22}[\tau \to \infty]\big|_{g\to\infty}$ from above. It can also be expressed as simply the product of Γ and $\boldsymbol{\rho}_{22}[\tau \to \infty]$. So, we can equate these two

definitions to get

$$\Gamma\frac{k_{41}}{k_{24}+2k_{41}}\frac{S}{1+S}=\Gamma\frac{2g^2k_{41}}{2g^2k_{24}+4g^2k_{41}+\Gamma_2k_{24}k_{41}+\Gamma\Gamma_2k_{41}}. \tag{3.24}$$

This allows us to express the coupling g in terms of a saturation parameter S

$$g=\sqrt{\frac{Sk_{41}\Gamma_2(k_{24}+\Gamma)}{2k_{24}+4k_{41}}}. \tag{3.25}$$

This will be useful when we compare $g(2)(\tau)$ curves in different regimes of saturation.

We solve the time dependent optical Bloch equations fully using a Laplace transform method [134]. The initial conditions of this system of equations are $\boldsymbol{\rho}_{11}=1$, $\boldsymbol{\rho}_{22}=0$ and $\boldsymbol{\rho}_{44}=0$. Then applying a Laplace transform with parameter s to each of the equations,

$$s\mathcal{L}\{\boldsymbol{\rho}_{22}\}=-\Gamma\mathcal{L}\{\boldsymbol{\rho}_{22}\}-k_{24}\mathcal{L}\{\boldsymbol{\rho}_{22}\}+ig(\mathcal{L}\{\boldsymbol{\rho}_{12}\}-\mathcal{L}\{\boldsymbol{\rho}_{21}\}), \tag{3.26}$$

$$s\mathcal{L}\{\boldsymbol{\rho}_{11}\}-1=\Gamma\mathcal{L}\{\boldsymbol{\rho}_{22}\}+k_{41}\mathcal{L}\{\boldsymbol{\rho}_{44}\}+ig(\mathcal{L}\{\boldsymbol{\rho}_{21}\}-\mathcal{L}\{\boldsymbol{\rho}_{12}\}), \tag{3.27}$$

$$s\mathcal{L}\{\boldsymbol{\rho}_{12}\}=-\Gamma_2\mathcal{L}\{\boldsymbol{\rho}_{12}\}+ig(\mathcal{L}\{\boldsymbol{\rho}_{22}\}-\mathcal{L}\{\boldsymbol{\rho}_{11}\}), \tag{3.28}$$

$$s\mathcal{L}\{\boldsymbol{\rho}_{21}\}=-\Gamma_2\mathcal{L}\{\boldsymbol{\rho}_{21}\}+ig(\mathcal{L}\{\boldsymbol{\rho}_{11}\}-\mathcal{L}\{\boldsymbol{\rho}_{22}\}), \tag{3.29}$$

$$s\mathcal{L}\{\boldsymbol{\rho}_{44}\}=k_{24}\mathcal{L}\{\boldsymbol{\rho}_{22}\}-k_{41}\mathcal{L}\{\boldsymbol{\rho}_{44}\}\,\text{and} \tag{3.30}$$

$$\mathcal{L}\{\boldsymbol{\rho}_{11}\}+\mathcal{L}\{\boldsymbol{\rho}_{22}\}+\mathcal{L}\{\boldsymbol{\rho}_{44}\}=\frac{1}{s}. \tag{3.31}$$

Now we can solve this system of equations to give $\mathcal{L}\{\rho_{22}\}$ in terms of the transition rates and s the parameter of the Laplace transform

$$\mathcal{L}\{\boldsymbol{\rho}_{22}\}=\frac{2g^2\left(k_{41}+s\right)}{s\big(2g^2k_{24}+4g^2k_{41}+4g^2s+\Gamma_2(\Gamma k_{41}+k_{24}s+k_{41}s+k_{24}k_{41}+s^2+\Gamma s)+k_{24}s^2+k_{41}s^2+\Gamma k_{41}s+k_{24}k_{41}s+s^3+\Gamma s^2\big)} \tag{3.32}$$

The Laplace transform of an exponential is

$$\mathcal{L}\{e^{at}\}=\frac{1}{s-a}. \tag{3.33}$$

So, we can then perform the inverse Laplace transform by arranging the expression for $\mathcal{L}\{\boldsymbol{\rho}_{22}\}$ in the form

$$\mathcal{L}\{\boldsymbol{\rho}_{22}\}=\sum_{i=1}^{4}\frac{c_i}{s-s_i}. \tag{3.34}$$

where s_i are the roots of the quartic expression of the denominator of equation 3.32 above. These are rather long expressions of the transition rates but can be dealt with symbolically

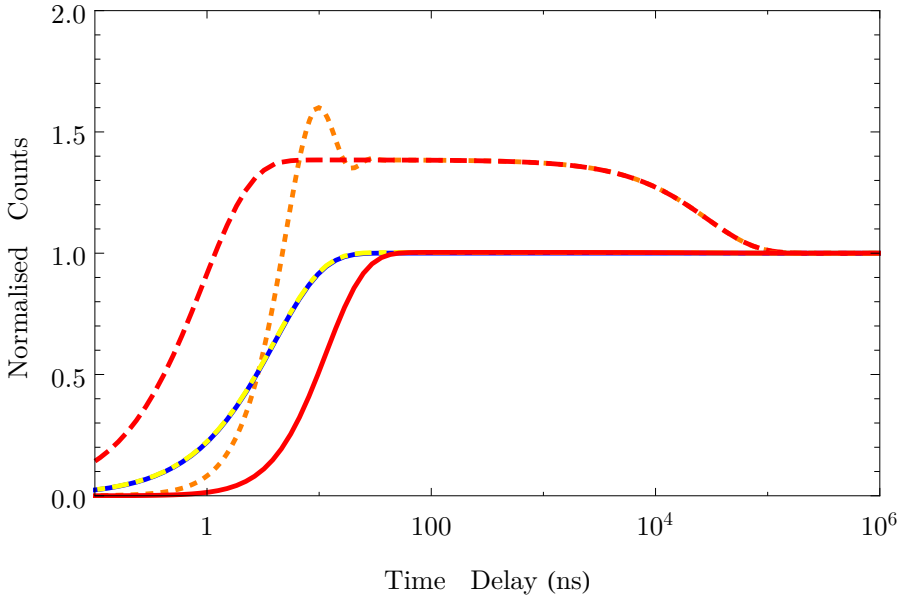


Figure 3.17: The predicted $g^{(2)}(\tau)$ curve for a single molecule with multiple levels shown in figure 3.16. The short-dashed orange curve shows the molecule being driven resonantly with the ZPL at a high rate and demonstrates Rabi oscillations at short times and photon bunching due to the triplet state at longer times. The dashed red line shows the observed second order correlation at room temperature at the same saturation, at room temperature the dephasing rate, Γ_2 is greatly increased. The solid red curve shows the response from a single molecule being driven resonantly at low pump powers. The dot-dashed yellow line shows the second order correlation function for a molecule that is driven at low power at room temperature. The blue line shows the molecule being driven from the ground state, $|1\rangle$, to level $|3\rangle$. More details in the text.

in Mathematica. The values of c_i are determined using partial fractions and are given as

$$c_i = \frac{2g^2\,(k_{41} + s_i)}{\prod_{j=1}^{4}(1-\delta_{ij})(s_i - s_j)}. \tag{3.35}$$

Then we can do the inverse Laplace transform and the expression for $\boldsymbol{\rho}_{22}$ is

$$\boldsymbol{\rho}_{22} = c_1 e^{s_1 t} + c_2 e^{s_2 t} + c_3 e^{s_3 t} + c_4 e^{s_4 t}. \tag{3.36}$$

Finally, $\boldsymbol{\rho}_{22}(\tau)$ divided by $\boldsymbol{\rho}_{22}(\infty)$, gives us $g^{(2)}(\tau)$. We can now see how the $g^{(2)}(\tau)$ curve depends on the different transition rates and the coupling strength of the driving field. Figure 3.17 shows these curves normalised against the value at times longer than any timescale of the dynamics of the molecule, in this case at $\tau = 1\,\text{ms}$. The orange short-dashed curve shows the $g^{(2)}(\tau)$ at high pumping powers. The rates for the molecule are $\Gamma = 250\,\text{MHz}$ ($\tau_1 = 4\,\text{ns}$), $k_{24} = 25\,\text{kHz}$ (corresponds to an intersystem crossing of 10^{-4} which is greatly inflated to demonstrate the behaviour), $k_{41} = 25\,\text{kHz}$ (triplet

lifetime= 40 μs), $\Gamma_2 = 125\,\text{MHz}$ and $S = 5$. This curve shows a Rabi oscillation at short delay times, followed by a shoulder due to trapping in the triplet state. At much longer times $g^{(2)}(\tau)$ tends to unity.

The red dashed curve shows the same molecule being driven on the ZPL but at room temperature. At this elevated temperature the dephasing rate, Γ_2 is now at 12.5 THz. This is comparable to the dephasing rate for DBT at room temperature. It is still being driven at a saturation parameter of $S = 5$ which is a significantly higher power than when the molecule is warm, and the population damping rates are unchanged. This curve shows no Rabi oscillations as the coherence between levels $|1\rangle$ and $|2\rangle$ quickly decays. It does show a narrowing of the dip at short times.

The solid red curve is the seen when the pumping rate is low, $S = 0.01$. The form of the curve in this regime simplifies to the form

$$g^{(2)}(\tau) = (1 - e^{-\frac{\Gamma}{2}|\tau|})^2, \tag{3.37}$$

when S is small and $\Gamma_2 = \frac{\Gamma}{2}$.

The yellow dot-dashed line is the curve seen at both low powers and room temperature ($\Gamma_2 = 12.5\,\text{THz}$ and $S = 0.01$) this curve also reduces to the equation

$$g^{(2)}(\tau) = 1 - e^{-\Gamma|\tau|}, \tag{3.38}$$

when S is small and Γ_2 is large.

The blue curve is the curve when the molecule is being driven to the level $|3\rangle$. In this case the molecule behaves like the resonant pumping at room temperature. The curve shown is at low pumping powers. At higher powers the curve approaches the red, dashed curve and the triplet level can be seen.

We measure the second order correlation function by selecting one molecule that seemed well isolated for images in the confocal microscope. We then centered the microscope over this single molecule and optimised the position of the galvo mirrors observing the fluorescence counts on one of the APDs. To take the measurement, the fluorescence light is split by a beamsplitter and coupled to two multimode fibres connected to two APDs as shown in figures 3.9 and 3.10. The APDs are connected to a timing card (TimeHarp 200, PicoQuant) by two coaxial cables, one of which has an additional 30m of cable and goes through a pulse inverter. The timing card allows us to measure the time difference between pairs of TTL pulses from the APDs. The time delays between many pairs of pulses are then plotted in a histogram. This is precisely the time delay between photons emitted by the molecule. Due to the extra length in one of the cable the zero time delay in the $g^{(2)}(\tau)$ histograms was actually at around 100 ns. The curves shown later have been offset to show zero time delay at $\tau = 0$.

The data and fitted curve are shown in figure 3.18. This curve shows clear antibunching

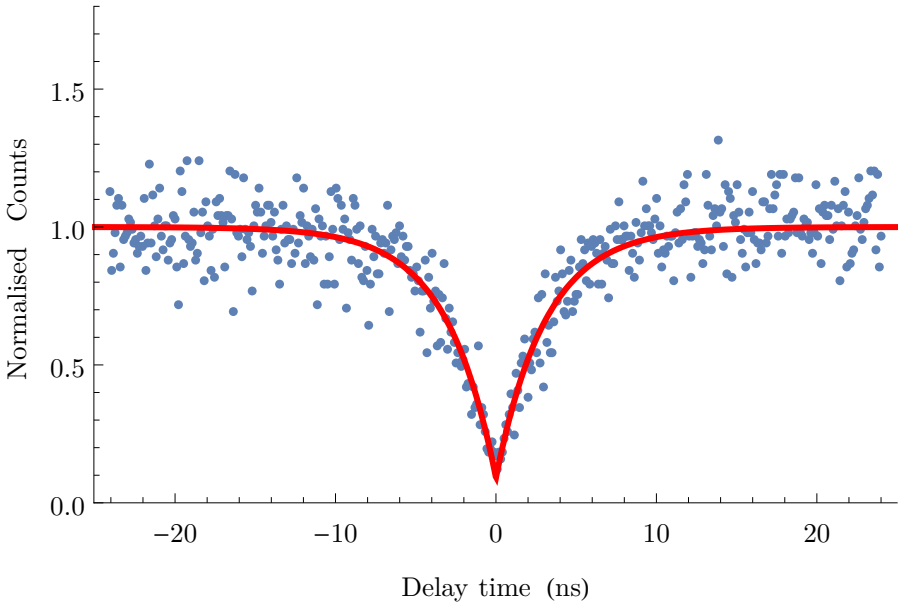


Figure 3.18: A $g^{(2)}(\tau)$ curve for short times showing antibunching for zero time delay. The fitted line is equation 3.38 which yields visibility of 91% and lifetime $\frac{1}{\Gamma} = \tau_1 = 3.11\,\text{ns}$

at zero time delay, with a dip that goes down to 9% at the centre. When fitted, the peak denotes a lifetime of 3.11 ns. The visibility of the dip is 91%. We expect a small increase from zero at $\tau = 0$ because the timing card has a resolution of 108.6 pm, but that should only account for 0.7%. We think there is some emission from other nearby molecules. If there were two molecules in the confocal spot half of the light would be coming from one molecule and the other half from the second molecule. At $\tau = 0$, $g^{(2)}(\tau) = 0.5$. This is true in general for n molecules so the modified form of equation 3.38 curve would be

$$g^{(2)}(\tau) = 1 - \frac{1}{n} e^{-\Gamma|\tau|}. \tag{3.39}$$

On fitting the data in figure 3.18 to this equation (3.39), we find $n = 1.09$ molecules. We are mostly observing the light from a single molecule but other molecules out of focus or nearby reduce the visibility.

The timecard gave the autocorrelation at short time delays but could not measure out to the long times, where we may be able to observe the triplet shoulder shown in figure 3.17. For this, we record the APD signals using a DAQcard (USB-6343, National Instruments) with a timing resolution of 1 μs, enough to resolve individual TTL pulses. We recorded the emission from a single molecule for 20 s. The autocorrelation of the light from this single molecule over these long time delays is seen in figure 3.19, together with the data for shorter delays from another molecule. Both have been normalised to the maximum coincidence counts at long time delays.

The triplet shoulder that we see in figure 3.20, is very small, but it is, nevertheless sufficient to provide information on the triplet lifetime. We use a simplified expression for

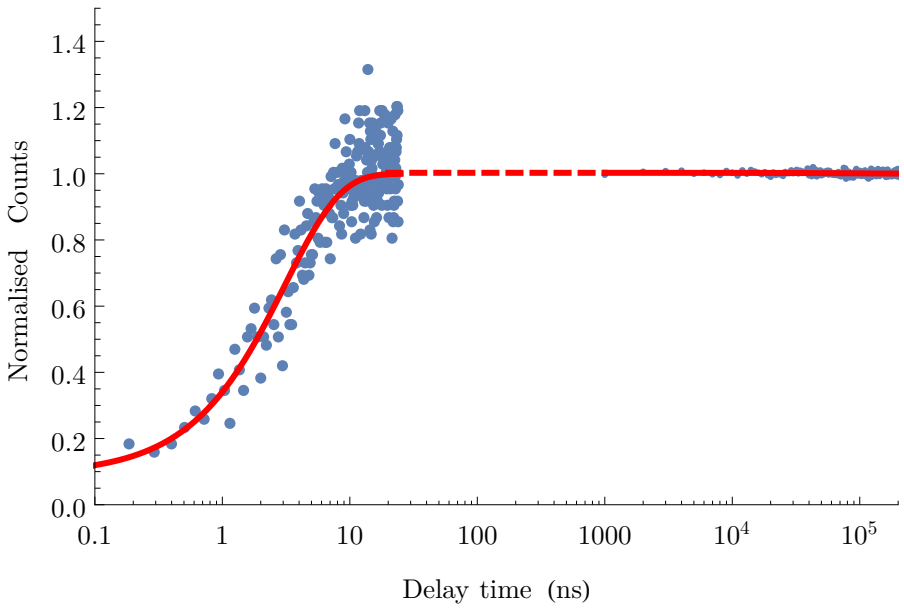


Figure 3.19: A graph showing the combination of short and longer timescale autocorrelation measurements.

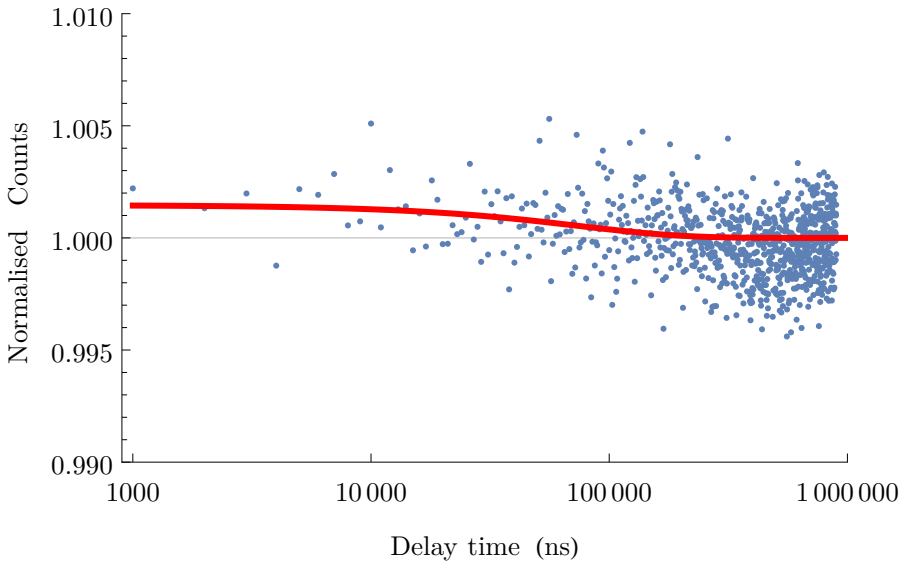


Figure 3.20: A graph showing the longer timescale autocorrelation measurements. The fit is of the form of equation 3.40.

the $g^{(2)}(\tau)$ (equation 6 in [135]). When $k_{24} + k_{41} << \Gamma$ the correlation function can be given as

$$g^{(2)}(\tau) = 1 + Ae^{-\sigma\tau}, \tag{3.40}$$

where

$$\sigma = k_{41} + \frac{k_{41}S}{1 + 2S\frac{k_{41}}{k_{24}}} \tag{3.41}$$

and

$$A = \frac{\sigma - k_{41}}{k_{41}}. \tag{3.42}$$

For the fitted curve in figure 3.19, $\sigma = 14000 \pm 4000$ and $A = 0.0014 \pm 0.0003$. From equations 3.41 and 3.42 and using the fact that the intersystem branching ratio is $\phi = \frac{k_{41}}{k_{21}+k_{41}}$, we measure a triplet lifetime of $70 \pm 30\,\mu$s and an intersystem branching ratio of $1.2 \pm 0.5 \times 10^{-7}$. This is consistent with the values previously found for DBT in anthracene by Nicolet *et al.*, who report triplet lifetimes in the range $40 - 200\,\mu$s and say ϕ is "around 10^{-7}" [55].

Our fit to the data in figure 3.18 to equation 3.38 gives an upper state lifetime of 3.11 ns. This allows us to assess the collection efficiency of the microscope. From a bright molecule we collect 100 kcounts/s whereas from the lifetime we should expect 3.2×10^8. Therefore the collection efficiency of the microscope is only of the order 3×10^{-4}.

At room temperature, the emission from DBT is distributed over a wide range of wavelengths. In order to spectrally resolve the vibrational structure in the emission from a single molecule it is necessary to cool the molecules down. By placing molecules into the cold confocal setup we can do just that. A crystal of anthracene doped with DBT was placed onto a glass coverslip which was thermally contacted to the beryllium copper sample mount using a small amount of thermal grease. The setup was cooled to 3.4 K and a confocal image of a small area of the crystal taken. The galvo mirrors pointed the beam onto a single DBT molecule and the collected fluorescence was sent to the spectrometer.

The spectrometer was tested with an attenuated laser beam. This registered 800 cps on the APDs which have an efficiency of 65%. The EMCCD with 210 vertically binned pixels, a pre-gain of 4× and a gain setting of 255 then registered 170 counts/photon above the background. This enabled us to record the spectrum of just one DBT molecule, as shown in figure 3.21. Exposures were taken for 100 s. The molecule was pumped on its zero phonon line at 786 nm and the residual laser light passing through the longpass filters can be seen as a peak at that wavelength. This molecule was out in the red wing of inhomogeneous broadening so the wavelength of the zero phonon line is different from 785 nm given in section 2.3. The step up at 800 nm shows where the edge of the longpass

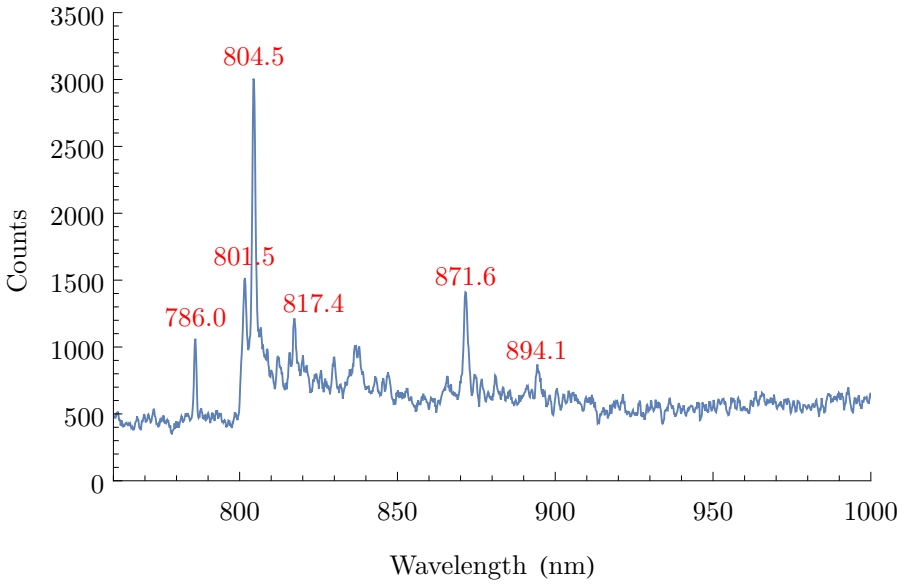


Figure 3.21: The emission spectrum of a single DBT molecule. The edge of the 800 nm longpass filter can be seen and the peak at 786.0 nm is the residual excitation laser light. Other emission lines are labelled with their wavelength. It should be noted this molecule is in the wings of the inhomogeneous distribution.

filter is. Moving to longer wavelengths, we see the emission from the first five vibronic states of the excited state manifold to the ground state (labelled).

By scanning the frequency of the excitation laser and monitoring the amount of fluorescence we mapped the homogeneous linewidth of the zero phonon line using a single APD. Scanning the transition at 390 nW we see the line profile plotted in figure 3.22. This line is very broad compared to what we expect for cryogenic DBT molecules [55, 82]. The excitation intensity is too low for this to be caused by power broadening. The most obvious explanation is that although the molecules are cold, they are not cold enough to have lifetime-limited linewidths. They are not at the 3.4 K that the cryostat says they are. In fact, deducing the temperature from the linewidth according to Nicolet *et al.* the molecules seemed to be at a temperature of ≈ 8 K. We therefore had to consider why it was not lower.

Our samples are mounted on #00 glass coverslips using N grease for thermal contact with the cold plate. They sit directly below a 2 mm hole in the radiation shield and the objective at a temperature of 300 K which is only 300 μm away. The black body radiation from this should be low enough that the cryostat can deal with the heat load and keep the molecules below 4 K. Another source of heating could be from residual gas in the chamber, but calculations show that this should be easily cooled by the cryostat. However, poor conduction from the mounted samples to the cold plate could be responsibly for the anomalously high temperature of the molecules (and we now know that it was).

We wanted to meaure the distribution of the zero-phonon lines to be able to compare

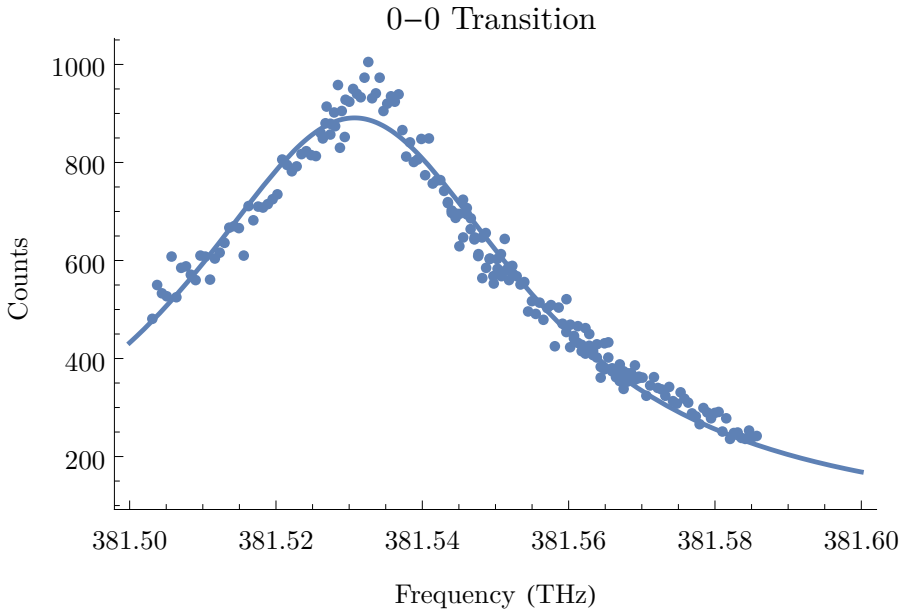


Figure 3.22: The lineshape of the zero phonon line transition of a DBT molecule at 390 nW. The fitted function is a Lorentzian with FWHM of 56 ± 8 GHz.

them with literature values. We measure the ZPL distribution by taking images of a small area of the crystal at about 40 different excitation laser frequencies. Three of these can be seen in figure 3.23, where the individual molecules can be seen as single dots. In different images different molecules can be seen depending on whether the laser is resonant with that individual molecule or not. In images at similar frequencies, the molecules can be seen to persist from one image to another. This is because, as was shown above, the linewidth of individual molecules is a significant fraction of the inhomogeneous distribution. Also, in figure 3.23 we can see the summed counts for each image at a given excitation frequency. Gaps in the scan are due to mode hops of the Ti:Sapphire laser. The counts are peaked at 382.388 ± 4 THz with a full width half maximum of 220 ± 11 GHz. With the highest concentration of molecules grown, we would expect around 18 molecules to be located within the $\approx 20\,\mu\text{m}^2$ cross sectional area of the cavity mode. Since we can scan the frequency of the excitation laser by 40 GHz, we can expect to find 1.9 molecules on average coupling to the cavity and also accessible by the laser. This means that the crystals have an ideal concentration to couple single molecules to the fibre microcavities.

Recently, we have managed to see molecules with a much narrower linewidth by improving the thermal contact in our cryostation. The way that the sample is thermally contacted to the sample mount had a severe effect of the final temperature of the molecules. After testing various candidates, the N grease was replaced with a colloidal silver paint (G3790, Agar Scientific). This enabled the molecule to reach a lower temperature, estimated to be 4.4K from the narrow linewidths. A scan of a narrow molecule is seen in figure 3.24. This

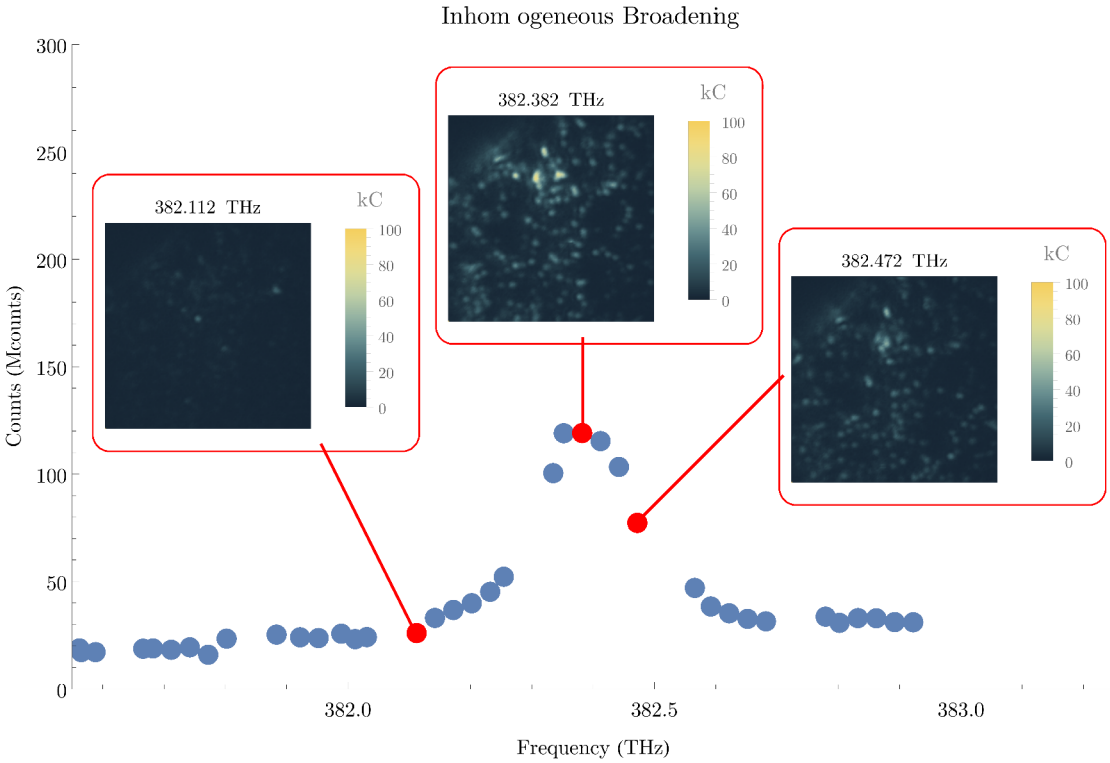


Figure 3.23: The summed counts of multiple images at different laser frequencies showing the distribution of the zero phonon lines of individual DBT molecules. The images are taken at the frequencies indicated by the red points.

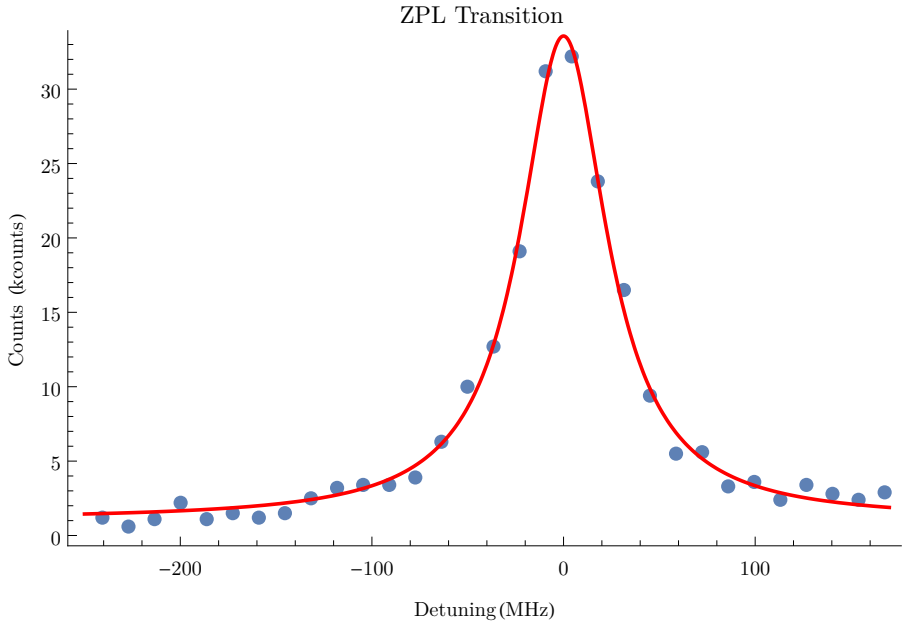


Figure 3.24: The linewidth of a single cold DBT molecule. The fitted curve is a Lorentzian with a FWHM of 55 ± 2 MHz.

was measured in the cold confocal microscope using the 780nm DFB laser described in section 6.2, at a frequency of 382.454 THz. The detuning from resonance is shown in MHz. The linewidth is fitted with a Lorentzian line shape that has a FWHM of 55 ± 2 MHz. Given the lifetime of 3.11 ns measured at room temperature from the $g^{(2)}(\tau)$, we would expect a lifetime-limited linewidth of 51 MHz, so this line may still be lightly broadened by interaction with phonons. It is also slightly wider than the 32 MHz presented by Nicolet *et al.* [55]. Even so, we can say that a key goal has essentially been reached here.

In summary, we were able to grow DBT-doped anthracene crystals and measure properties of both the anthracene and the DBT molecules. At cryogenic temperatures, the molecules initially had a much wider zero phonon line linewidth than has been previously reported because they were not cooling properly. The molecules were however stable and located in a defined orientation inside optically good crystals, at a known concentration, making them ideal to be placed inside optical fibre microcavities. Very recently, we have understood how to make the sample stage cool properly and we have been able to see spectra with a much narrower linewidth, close to the lifetime limit.

CHAPTER 4

CRYOGENIC MICROCAVITIES

4.1 Theory

In this chapter, I discuss the theory, construction and first tests of an optical microcavity, designed to collect photons from several individual DBT molecules. These are plano-convex Fabry-Perot cavities, formed between an array of circular concave mirrors and an array of optical fibres. The round mirrors were made by wet etching and overcoating with a dielectric Bragg reflector (before my time as a PhD student). These mirrors have already been effective in building high finesse cavities [136, 137]. The plane mirrors are dielectric Bragg reflectors coated on the polished face of a commercial 12-fibre array. An optical microcavity is created by aligning one of the optical fibres with one of the round mirrors as illustrated in figure 4.1.

In the paraxial approximation the electric field of a free space propagating laser is a solution to the Helmholtz equation. The solutions can be represented by the Hermite-Gaussian function which form a complete orthonormal set [138]. The electric field has the

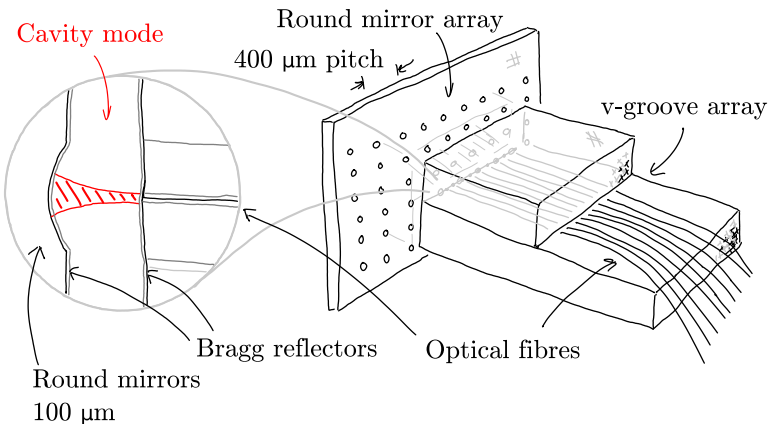


Figure 4.1: The optical fibre v-groove array with attached Bragg reflector brought up to the array of round mirrors to create an optical microcavity

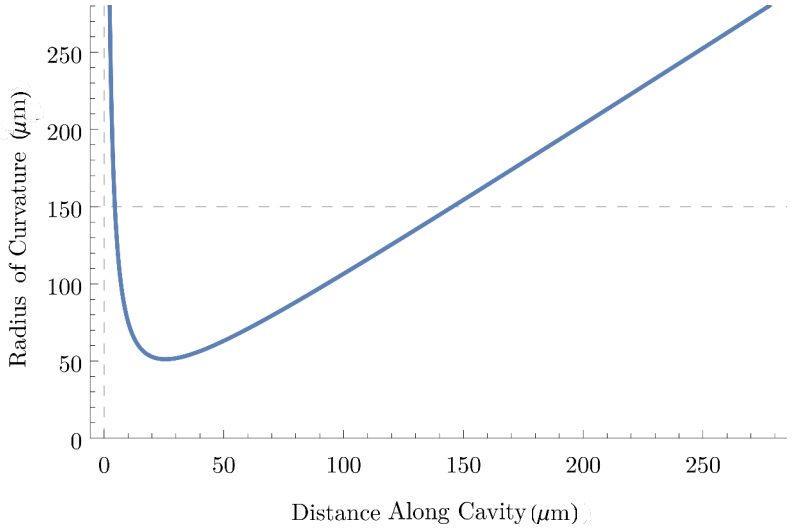


Figure 4.2: The radius of curvature of a Gaussian beam expanding in free space with the mirror radius shown as a dotted line.

form

$$E_{n,m}(x,y,z) = E_0 e^{ikz}\sqrt{\frac{2}{\pi}}\frac{1}{w(z)}e^{-\frac{x^2+y^2}{w(z)^2}}\frac{1}{\sqrt{2^n n!}}H_n\left(\frac{\sqrt{2}x}{w(z)}\right)\frac{1}{\sqrt{2^m m!}}H_m\left(\frac{\sqrt{2}y}{w(z)}\right)\Phi_r\Phi_z. \tag{4.1}$$

where the light propagates along the z axis and has a Gaussian profile in x, y when $n = m = 0$. The expression is normalised so that the total intensity is E_0^2. When $n \neq 0$, $m \neq 0$ the profile is multiplied by Hermite polynomials H_n and H_m at higher order (n, m). $w(z)$ is the characteristic beam width and is given by

$$w(z) = w_0\sqrt{1+\left(\frac{z}{z_R}\right)^2}, \tag{4.2}$$

where w_0 is the beam waist at the end of the fibre. z_R is the Rayleigh range, $z_R = \frac{\pi w_0^2}{\lambda}$, which is also the point when $w = \sqrt{2}w_0$. Φ_r and Φ_z give the additional contributions to the phase of the field,

$$\Phi_r(z) = e^{i\frac{k(x^2+y^2)}{2\mathcal{R}(z)}}. \tag{4.3}$$

This just represents the phase change across the transverse plane due to the curvature of the wavefront. In the last term,

$$\Phi_z(z) = e^{i(1+m+n)\tan^{-1}\left(\frac{z}{z_R}\right)}, \tag{4.4}$$

the exponent is called the Gouy phase.

As this beam propagates the radius of curvature also changes according to

$$\mathcal{R}(z) = (z + \frac{z_R^2}{z}), \tag{4.5}$$

where the beam has a plane wavefront at the fibre end, and diverges as it propagates through the cavity. A plot of this is shown in figure 4.2. If the second mirror is placed at a distance where the radius of curvature of the mirror matches that of the beam, a stable cavity is created. For the particular size of the mode in the fibre ($w = 2.5\,\mu$m), a cavity length of $\approx 150\,\mu$m requires the radius of curvature of the mirror to be $150\,\mu$m, marked as a dashed line in figure 4.2. The finesse, $\mathcal{F}$, of these cavities is the ratio of the width of the transmission peak, $\Delta\lambda$, to the free spectral range, FSR, of the cavity and is determined by the reflectances of the mirrors, R_1 and R_2,

$$\mathcal{F} = \frac{\Delta\lambda}{FSR} \approx \frac{\pi(R_1R_2)^{\frac{1}{4}}}{1-(R_1R_2)^{\frac{1}{2}}}. \tag{4.6}$$

This approximation is valid for high reflectivities.

Now, we can determine the resonances of the cavity by considering the electric field inside the cavity. The field within the cavity is due to light originally transmitted through the first mirror and the multiple reflections from the two mirrors. The electric field entering the cavity through the first mirror is E_0t_1 with E_0 being the incident field and $t_1 = \sqrt{T_1}$ where T_1 is the transmitted power. As the field propagates in the cavity it acquires a phase according to equation 4.1. So the field just before the second mirror is $E_0t_1e^{ikl}\Phi_r(l)\Phi_z(l)$ for cavity length l. Part of this field is transmitted through the second mirror but most is reflected off of the second mirror and makes another transit of the cavity so the electric field has another contribution of $E_0t_1r_1r_2e^{ikl}\Phi_r(l)\Phi_z(l)(e^{i2kl}\Phi_r(2l)\Phi_z(2l))$. There are an infinite number of contributions of these and so we can give the total electric field in the cavity as the geometric sum of terms representing initial transmission and the reflection back and forth from both mirrors along with the phase accumulated from round trips of the cavity:

$$E_{cav} = E_0\Big(t_1e^{ikl}\Phi_r(l)\Phi_z(l) + t_1r_2r_1e^{ikl}\Phi_r(l)\Phi_z(l)(e^{i2kl}\Phi_r(2l)\Phi_z(2l)) \tag{4.7}$$

$$+ t_1r_2r_1e^{ikl}\Phi_r(l)\Phi_z(l)(e^{i2kl}\Phi_r(2l)\Phi_z(2l))^2 + \dots\Big). \tag{4.8}$$

We can perform the geometric sum and express the electric field in the cavity as

$$E_{cav} = E_0\left(\frac{t_1e^{ikl}\Phi_r(l)\Phi_z(l)}{1-r_1r_2(e^{i2kl}\Phi_r(2l)\Phi_z(2l))^2}\right). \tag{4.9}$$

So, the electric field in the cavity is maximised when $(e^{i2kl}\Phi_r(2l)\Phi_z(2l))^2 = 1$, using

equations 4.7 and 4.8,

$$2kl + \frac{k(x^2+y^2)}{2\mathcal{R}(2l)} + 2(1+m+n)\tan^{-1}\left(\frac{2l}{z_R}\right) = 2\pi q, \tag{4.10}$$

for integers q. This is the resonance condition for the cavity. For $m = n = 0$ at $x = 0$ and $y = 0$, this means $\lambda = \frac{2l}{q}$. For the higher order radial modes the resonance conditions are slightly modified by the Gouy phase. We can measure the resonance of such a cavity by looking at the reflected intensity from the cavity.

The reflected intensity is equal to $E_0^2 - E_t^2$ where E_t is the transmitted electric field which is given by the transmission through the second mirror of the circulating field in the cavity

$$E_t = t_2 E_{cav} \tag{4.11}$$

$$E_t = E_0\left(\frac{t_1 t_2 e^{ikl}\Phi_r(l)\Phi_z(l)}{1 - r_1 r_2 (e^{i2kl}\Phi_r(2l)\Phi_z(2l))^2}\right). \tag{4.12}$$

The reflected intensity for $x = 0$ and $y = 0$ is thus

$$I_r = E_0^2 - \frac{E_0^2 t_1^2 t_2^2}{1 + r_1^2 r_2^2 - 2r_1 r_2\cos(\delta)}, \tag{4.13}$$

for each mode in the cavity, where $\delta = 2kl + (1+m+n)\tan^{-1}\left(\frac{2l}{z_R}\right)$.

The value of the theoretical reflected intensity as the cavity length is scanned is shown in figure 4.3. It is possible to measure many properties of the cavity by observing this reflection spectrum. If the cavity length is changed by many half-integer wavelengths then several longitudinal resonant modes are observed over the course of its travel. We can achieve this using two piezo stacks for our microcavities (details in section 4.3). Measured traces show dips in the reflectance, allowing us to measure the finesse of the cavity. Higher-order radial modes are excited because the axis of the fibre is offset from the axis of the cavity, as discussed below. These resonances can be used to determine the misalignment of the cavity. They also provide a simple way to measure the cavity length, which is otherwise hard to determine when the cavity is assembled. Let us further investigate how these higher order modes are excited.

The coupling into higher order radial modes can be calculated from their overlap with the fibre mode at the fibre end of the cavity. We represent the transverse mode of the incoming light in the fibre as a Gaussian ($n = m = 0$). When the fibre is well centred on the cavity, this Gaussian is orthogonal to the radially excited cavity modes ($n \neq 0$, $m \neq 0$), and therefore they are not excited. But if the fibre is displaced to the side, the

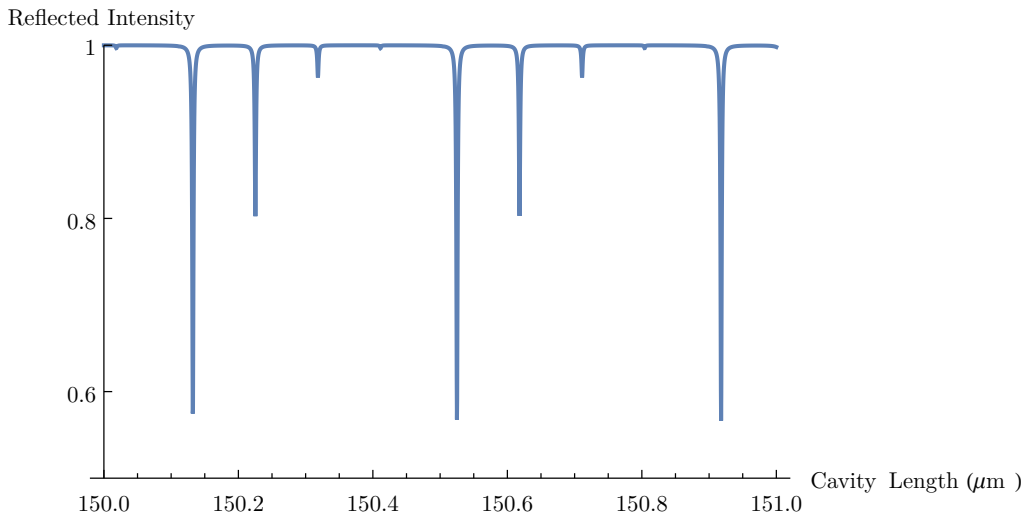


Figure 4.3: The theoretical modes of a cavity with the fibre misaligned by 0.7 beamwidths of the input mode in each direction. The higher order radial modes are seen as smaller peaks beside the fundamental modes.

overlap is

$$\int_{y=-\infty}^{\infty}\int_{x=-\infty}^{\infty} \frac{2}{\pi}\frac{1}{{w_0}^2\sqrt{1+\frac{c^2}{\left(\frac{\pi {w_0}^2}{\lambda}\right)^2}}}\frac{1}{\sqrt{2^n n!}}H_n\left(\frac{\sqrt{2}x}{w_0}\right)\frac{1}{\sqrt{2^m m!}}H_m\left(\frac{\sqrt{2}y}{w_0}\right) \tag{4.14}$$

$$e^{-\frac{x^2+y^2}{{w_0}^2}}e^{-\frac{(x-a)^2+(y-b)^2}{{w_0}^2\left(1+\frac{c^2}{\left(\frac{\pi {w_0}^2}{\lambda}\right)^2}\right)}}dxdy. \tag{4.15}$$

The displaced Gaussian has been moved by in x, y and z by a, b and c. w_0 is the beam width at the plane mirror. Displacements in z basically amounts to a change in the width of the cavity mode according to width change of a propagating Gaussian beam (see equation 4.2). The integral can be performed by using the explicit form of the Hermite polynomials. Details of this calculation are given in appendix A. The solution of this integration for one dimension (x) is

$$\sqrt{\frac{2n!}{2^n}}\sqrt{\frac{c'}{1+c'^2}}e^{-\frac{a^2}{{w_0}^2(1+c'^2)}}\sum_{j=0}^{\lfloor n/2\rfloor}\frac{(-1)^j}{j!(n-2j)!}\left(\frac{2\sqrt{2}}{w_0}\right)^{n-2j} \tag{4.16}$$

$$\sum_{k=0}^{\lfloor n/2-j\rfloor}\frac{(n-2j)!}{2k!(n-2j-2k)!}\left(\frac{{w_0}^2c'}{2(1+c'^2)}\right)^k\left(\frac{a}{1+c'^2}\right)^{n-2j-2k}(2k-1)!!, \tag{4.17}$$

where $c'^2 = 1+\frac{c^2}{\left(\frac{\pi {w_0}^2}{\lambda}\right)^2}$. This expression is a polynomial in the displacement of the cavity

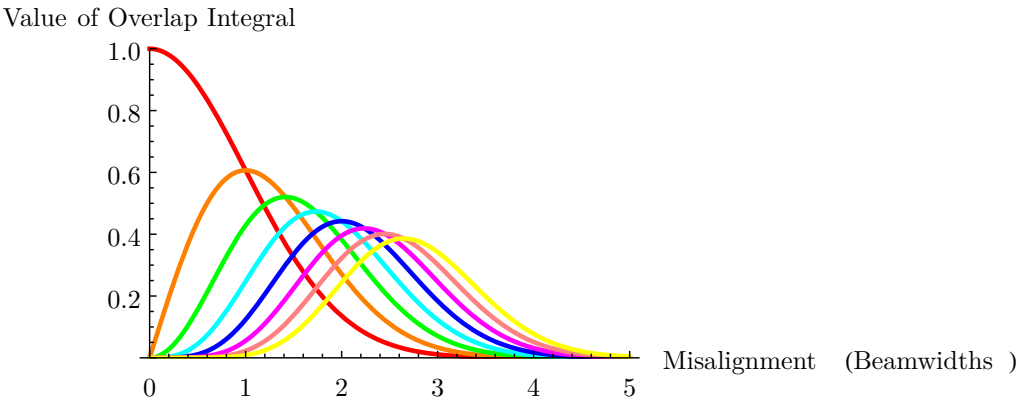


Figure 4.4: The graph of the overlap integral of the first eight modes of the cavity with a displaced Gaussian function as the cavity is misaligned in the x direction. At $x = 0$ only the fundamental mode has any overlap, as x increases the higher order radial modes have a significant overlap, thus higher order radial modes are excited in the cavity.

with a Gaussian envelope. There is a corresponding expression for misalignment in the other axis. The misalignment in the z axis effectively changes the width of the Gaussian and so couples to higher order modes but is much less sensitive than the displacement in x and y.

Figure 4.4 shows the value of the overlap of the displaced Gaussian fibre mode with the Hermite-Gaussian modes of the cavity for the first eight modes when the cavity is misaligned in one dimension (x). This then describes the coupling to the higher order modes. We now have enough theoretical understanding of the cavity modes and reflection spectrum to interpret the reflection spectrum from an actual cavity.

4.2 Cavity Characterisation

After aligning the cavity, as I describe in section 4.3, I scan the cavity length while monitoring the reflected light from the cavity. Figure 4.5 shows such a scan. The modes with $n = 0$ and $m = 0$ give the most prominent peaks in the scan, with the higher order radial modes seen as smaller peaks. As well as this higher mode structure, the cavity possesses split modes due to astigmatism in the mirrors (see figure 4.10) [137]. At low finesse, these are observed as an asymmetry in the cavity lineshape, while scans of cavities with higher finesse resolve these separate peaks, as seen in figure 4.5. This shows two separate scans of a cavity with a DBT doped anthracene crystal inside it. The cavity retains finesses of around 150 (similar to empty cavities) demonstrating that the anthracene crystal grown has good optical quality and does not reduce the finesse. The anthracene itself is also a birefringent material as mentioned in section 2.4. As described earlier, the anthracene crystals are grown as large plates in the x and y directions. The difference between the refractive indices in these two directions is 0.24. This means that

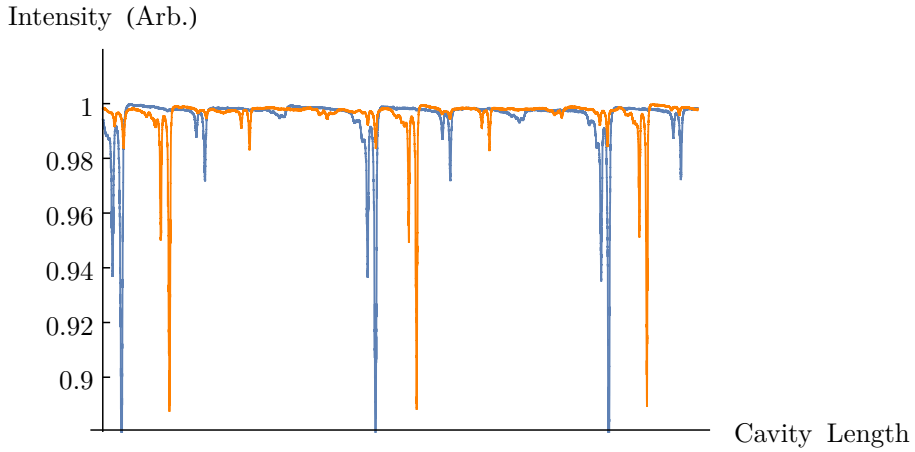


Figure 4.5: Two scans of the length of the cavity with the polarisation controller set at horizontal and vertical polarisations (shown in different colours). The peaks of one polarisation are visible as attenuated peaks in the other. The split modes due to the mirror asymmetry and higher order Hermite-Gaussian modes are also visible.

addition of anthracene into the cavity admits two separate polarisation modes within the cavity each with a slightly different optical length corresponding to n_x and n_y.

Before going into the cavity the fibre is passed through a fibre polarisation controller or wave plate (section 6.2). This allows the manipulation of the polarisation to contain more than 95% of the field in one linear polarisation mode of the cavity, horizontal or vertical. This is not 100% as the fibre controller does not allow the creation of a perfect wave plate.

The orange curve in figure 4.5 shows a scan with one (almost) linear polarisation, while the blue curve is for the perpendicular polarisation. The two polarisation directions have been chosen to maximise the difference, which is due to the birefringence of the anthracene. The imperfect polarisation means the horizontal polarisation resonance mode can be seen in the vertical polarisation scan and vice versa. This polarisation control of the light is essential for efficient coupling of the DBT molecule to the cavity mode because the DBT molecules preferentially align to the b axis of the crystal. By aligning the excitation light to the correct polarisation, it is automatically aligned with the molecular dipole moment, regardless of the crystal orientation on the mirror surface.

When we align the cavity, only the first few radial modes are seen. The depth of each of these dips or visibility is determined by how strongly each of these modes is excited which is determined from the overlap discussed above. Figure 4.6 shows the visibility of the first three cavity modes as the cavity is intentionally misaligned in the x direction. The measured visibility of the first few modes of the cavity, shown as points, are qualitatively similar to the visibilities of the first few modes as calculated from the overlap of these modes which are shown as solid curves. The visibilities were determined from the relative depth of the dips in the reflection spectrum as in figure 4.5 at different distances in the

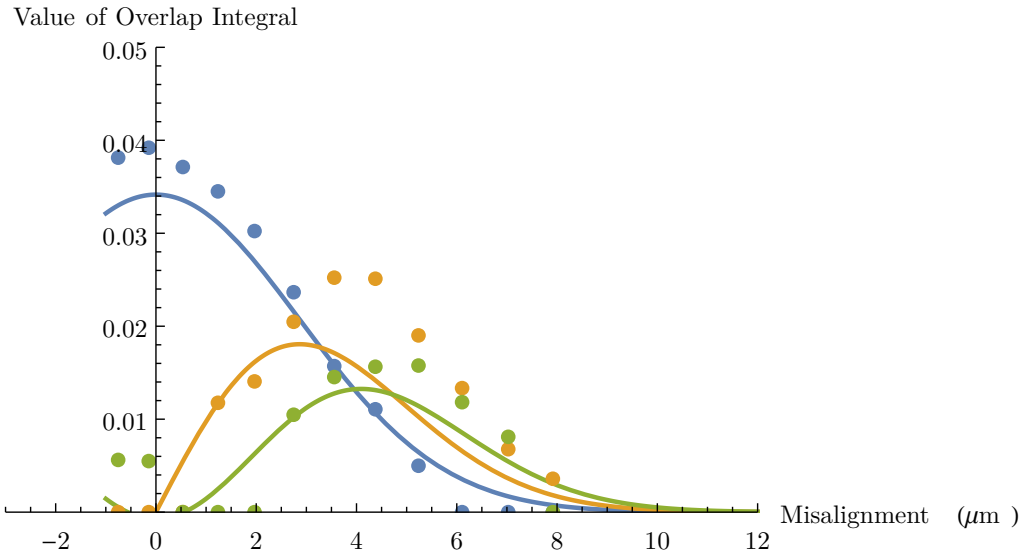


Figure 4.6: The predicted visibility from overlap integral (lines) and measurement (points) of the visibility of the fundamental traverse and first two higher order radial mode reflection resonances as the cavity is misaligned along one axis.

x-direction measured with a micrometer. For a misalignment comparable with the beam waist, $x = 2.5\,\mu$m, the population of the first and second orders is about equal. For the theory curves, we varied the misalignment in the z direction along with the zero offset of the misalignment in the x axis. The theory is shown as solid curves in figure 4.6. Although the data was fitted using these two parameters the discrepancy between the data and theory is still quite large. The misalignment in the y-axis was not varied but it was optimised before varying the x-axis. However, there still could have been a small misalignment is this axis. The disagreement could also be due to the fact that the higher order modes suffer different loss due to their larger spatial mode and the finite size of the mirrors and so the depth of the dip in the reflection spectrum is not entirely determined by the overlap integral. This would be confirmed by a Fox and Li numerical simulation [138], which can determine the stability of the higher order modes for a specific cavity geometry. The different modes are similar enough to the theory to allow us to identify which mode is which. As the spacing of the higher order modes is a function of the Gouy phase accumulated as the light propagates through the cavity it is possible to use the mode spacing as one way to determine the cavity length.

This means, the length of the cavity can be determined from the reflected spectrum. This was attempted in two ways. The first used the position change of the fundamental transverse peaks when the wavelength of the laser was changed and the second used the spacing of the radial modes in the cavity.

As the allowed wavelengths in the cavity are $\lambda = \frac{2l}{q}$ for $n = m = 0$, q can be determined by observing the shift in the position of the dips in the reflection spectrum. By changing the wavelength of the laser slightly and changing the cavity length to compensate. q is

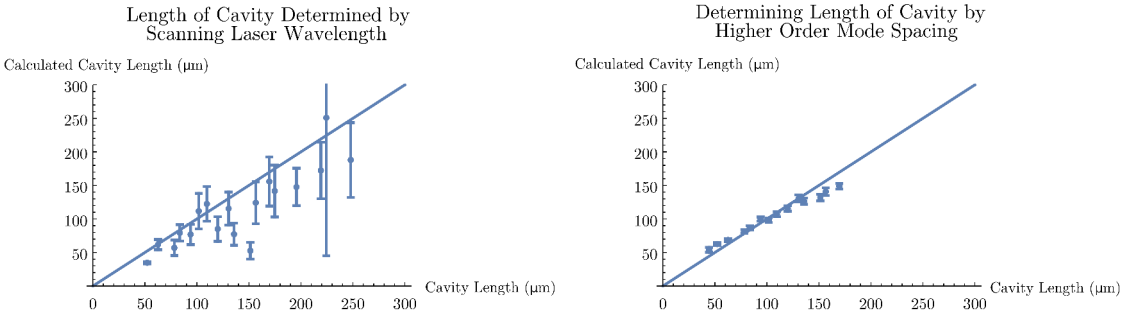


Figure 4.7: Cavity length as determined by two different methods.

then expressed as

$$q = \frac{1}{2}\frac{dl}{d\lambda}, \tag{4.18}$$

which means the length can be determined by

$$l = \frac{dl}{d\lambda}\lambda. \tag{4.19}$$

I determined the actual cavity length by measuring the separation of the v-groove array and the round mirror array with a microscope which could be varied with a micrometer. Shear piezos allowed the length of the cavity to be scanned a distance of several microns, as I will describe more fully in section 4.3. I moved the piezo to sit on a cavity resonance with $n = m = 0$. The wavelength of the laser was changed so the position of this resonance shifted. The piezo was then moved to regain the resonance. By noting the change in wavelength and in distance, the length could be determined from equation 4.19. The result of this analysis can be seen on the left of figure 4.7. The plotted points show the determined length at different measured lengths and the straight line is $y = x$. The error on the length determination is quite large as the laser wavelength could only be changed by approximately 1 nm. Figure 4.7 also shows length determination of the cavity by the higher order mode spacing.

The Gouy phase, given in 4.4 has a range of $\pm(1+m+n)\frac{\pi}{2}$ for the different values of m and n. This means that the first radially-excited mode is located at the midpoint between the longitudinal modes of the cavity at extreme short or long cavity lengths. In between, the spacing of the higher order radial modes as a fraction of the fundamental longitudinal mode spacing, $s = \frac{\text{radial mode spacing}}{\text{fundamental mode spacing}}$, varies with cavity length, l. We will show this using equation 4.10 at a length, l, corresponding to a fundamental longitudinal mode

$$kl + \tan(\frac{2l}{z_R}) = 2\pi q. \tag{4.20}$$

The expression at a different length, $l - \Delta l$, corresponding to the first excited radial mode

is

$$k(l+\Delta l)+2\tan^{-1}(\frac{2(l+\Delta l)}{z_R})=2\pi q. \tag{4.21}$$

Equating equations 4.20 and 4.21 using the approximation $\tan^{-1}(\frac{2(l+\Delta l)}{z_R})=\tan^{-1}(\frac{2l}{z_R})$, which is good for these long cavities. We arrive at

$$k\Delta l=\tan^{-1}\left(\frac{2l}{z_R}\right). \tag{4.22}$$

Now the fundamental longitudinal mode spacing is $\frac{\lambda}{2}$, so using $s=\frac{2\Delta l}{\lambda}$ we now have an expression for the length in terms of the radial mode spacing as a fraction of the fundamental longitudinal mode spacing

$$\pi s=\tan^{-1}\left(\frac{2l}{z_R}\right). \tag{4.23}$$

Knowing that the radius of curvature, $\mathcal{R}$, has to match that of the wavefront, we can write

$$\mathcal{R}=(l+\frac{z_R^2}{l}), \tag{4.24}$$

Now eliminating z_R between 4.23 and 4.24 the length is given by

$$l=\frac{2\mathcal{R}\tan^2(\pi s)}{1+\tan^2(\pi s)}. \tag{4.25}$$

This is a much more reliable way of determining the length of the cavity. The points on the right side of figure 4.7 show the calculated cavity length for a number of lengths measured with the microscope as before. At each point s is determined from a reflection spectrum like figure 4.5 by dividing the distance to the first radial mode by the distance between fundamental longitudinal modes. Again, the line is $y=x$. For our cavities $\mathcal{R}$ is $150\,\mu$m. This method has the advantage of only needing one cavity scan and not needed to shift the laser frequency. So, the cavity length can be measured using the reflectance spectrum from outside the cryostat using this second method. This is useful when aligning the cavities and during cooling as I show in the next section.

4.3 Cryogenic Cavity

One of the major challenges to this experiment is to develop a way of creating a cavity that is maintained while the setup is cooled to liquid He temperatures (ideally 2K). As was shown in the previous section the alignment of the fibre with respect to the mirror is sensitive to displacements of less than a micron in x and y. In order to minimise the potential misalignment due to movement when the cavity is cooled the cavity mount was

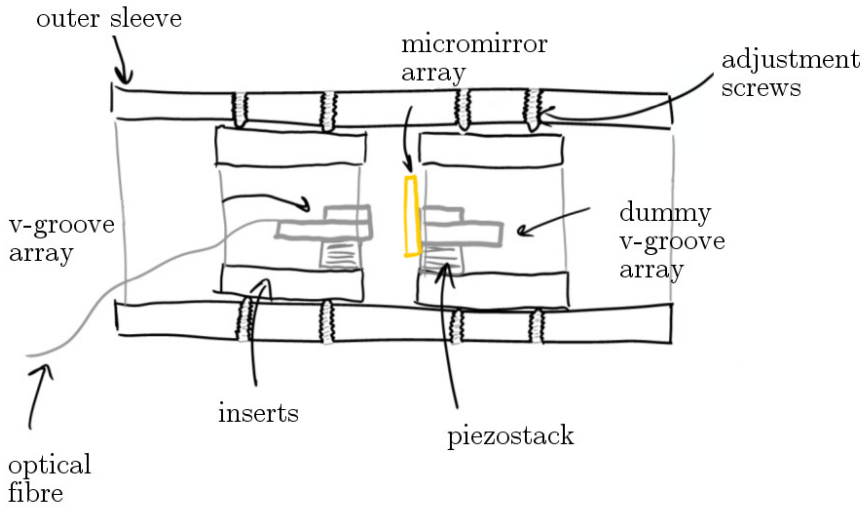


Figure 4.8: A simplified cavity design demonstrating the various components.

designed to be symmetric. The material of the mount was chosen to be Invar (FeNi36) due to its low coefficient of thermal expansion. The design concept is seen in figure 4.8 and consists of an outer sheath into which two assemblies are inserted one to hold the curved mirrors and one for the fibres. These inserts are held in place by the screws (also made of Invar) distributed around the outside, which can also adjust the position within the sheath. This design lets each insert be individually aligned but the whole cavity can be easily disassembled to run tests on the cavity and put DBT doped crystals inside the cavity. A CAD design is seen in figure 4.9, this shows the sheath and inserts assembled with a quarter section removed to show the interior of the inserts. The inset shows the detail of the v-groove array and round mirror array mounted on the shear piezo stacks and attached to each insert. The v-groove arrays are the transparent material and the gold coloured plate is the round mirror array. The cavity was machined from this CAD drawing using a combination of CNC (computer numerical control) machining and wire electrical discharge machining. The cavity design was first created in Nylon-12 using a selective laser sintering process. This was to test the cavity design and include any modification in the final invar design. The inserts had some material removed for the final design to improve optical access to the cavity and to ease alignment.

The optical fibres that form one side of the cavity are mounted into v-groove arrays. These are silicon blocks that have had multiple v shaped cuts scored into the block with an optical fibre laid inside each one. This block is then capped with a Pyrex block. The end face of this block was then polished and coated with a Bragg reflector, applied in one of two ways. The first method was to directly coat the mirror onto the v-groove array face. This coating was performed by O.I.B. GmbH. The coating itself is made of alternating

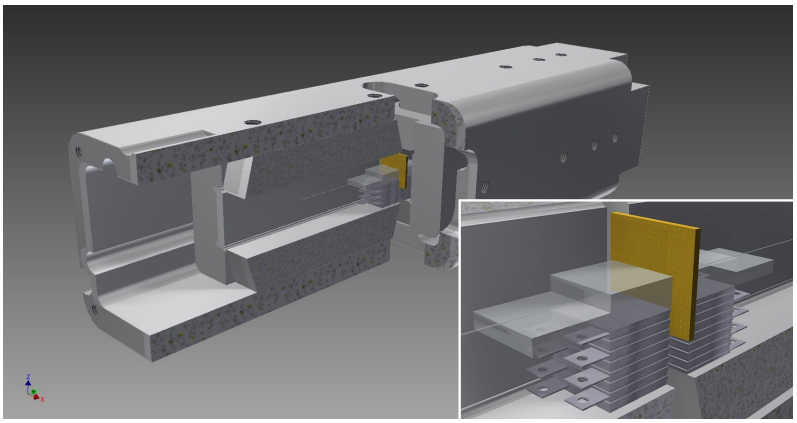


Figure 4.9: The insert design of the cavity showing removable inserts with adjustment threads. Inset: Detail of symmetrical v-groove arrays mounted on piezo stacks. The micromirror array is mounted to the face of one of the v-groove arrays.

layers of dielectric with refractive indices $n = 1.75$ and $n = 2.77$. Alternatively, this same coating was deposited onto glass plates which had first been coated with a layer of salt. The salt layer meant that the mirrors could be transferred to the v-groove array by first sticking the v-groove array to the mirror using a small quantity of UV curing adhesive (OG116, Epotek) and then pulling off the array with mirror attached. This removed a small section of the mirror from the plate, peeling off at the salt layer. The v-groove array was then washed in distilled water to remove the salt residue.

One insert holds the v-groove array which is glued onto a shear piezo stack to allow us to scan the length of the cavity. The piezo stack is then glued onto a channel running down the centre of the inserts, as illustrated in figure 4.8. Another similar insert is aligned on the other side where the v-groove array acts as a mount for the array of round mirrors. Two images of the round mirrors are shown in figure 4.10. As mentioned before, these are also made from silicon. The silicon wafers are coated with SiO_2 and then a photoresist. The photo resist is then exposed leaving circular apertures in the mask. A wet etch using a mixture of hydrofluoric, nitric, and acetic acid is applied while agitating the sample. This results in the closely spherical mirror seen in the image [139, 16]. The mirrors have a diameter of 110 μm. They also have a slightly flattened edges, as seen on the right of figure 4.10, giving the mirrors an asymmetry. The origin of this asymmetry is a slightly different etch rate for different crystallographic planes [140]. The radius of curvature is found by fitting a circle to the central part of the profile on the left of figure 4.10, which gives a value of approximately 150 μm. Because the centre of the mirrors is slightly flattened a fit to the whole section gives a larger radius of curvature of approximately 250 μm. The beam that falls on the mirror at a cavity length of 150 μm has a beam width of 15 μm, which covers a region where the central radius should be valid. Another method of determining the radius of curvature of the mirror in the cavity is to measure the radius using the higher order mode spacing mentioned before with a known cavity length. This gives a

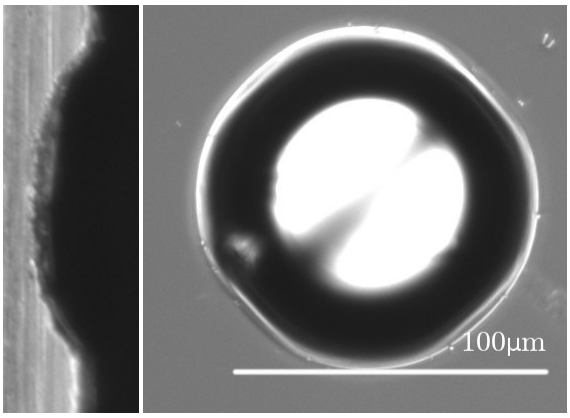


Figure 4.10: A single round mirror photographed from the top and in section.

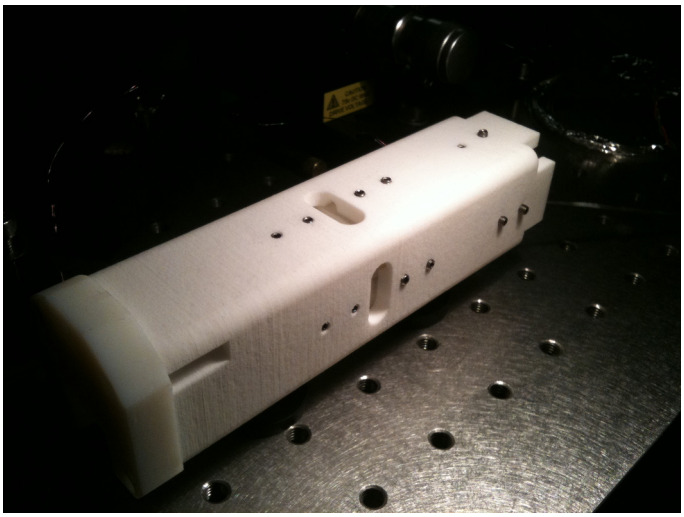


Figure 4.11: The assembled Nylon-12 prototype cavity mount.

radius of curvatue of $149 \pm 4\,\mu$m which agrees with the measured curvature of $150\,\mu$m by photographing the mirror.

Assembly started by first placing a bare v-groove array vertically and observing the end through a microscope. A small amount of UV curing adhesive (OG116-31, Epotek) was placed onto the face of the v-groove array and the micromirror array placed on top. The mirror array was aligned to the line of optical fibres beneath and cured using a UV lamp. The wire connections of the shear piezo stacks were then soldered using conductive epoxy (H21D, Epotek), baked for 1 hour, and one mounted onto a 3D translation stage. The 3D stage enabled me to position the piezo stack (P-121.03T, PI) accurately onto the base of the v-groove array to ensure the action of the shear piezo is parallel to the emission from the optical fibres. A collimated, level laser beam was reflected off of a polished part of the insert to make sure the insert was level. Then the same level beam was reflected off of the mirror surface and angled so that the laser returned to the same spot. This enabled the micromirror and v-groove arrays to be glued parallel to the two inserts, again using UV

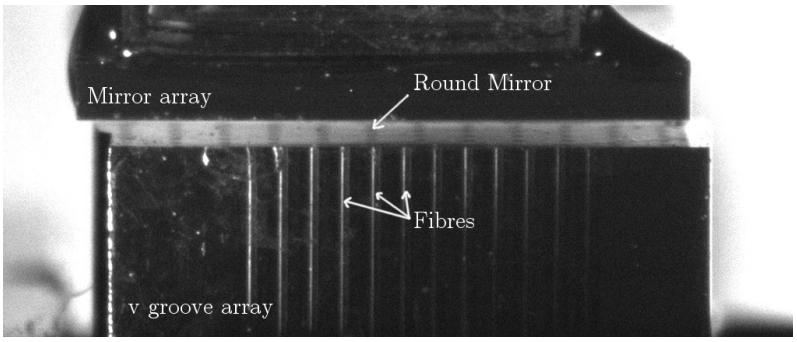


Figure 4.12: Top view of the aligned cavity. The top section of the photograph shows the dummy v-groove with mirror chip attached to the end face. The individual round mirrors are the dark circles on the mirror chip face. The lower section shows the v-groove array with 12 fibres seen as white lines running down the lower half of the image.

adhesive cured with a lamp. This eased alignment when the cavity was assembled. Once both piezo stacks were glued onto their respective inserts the cavity could be assembled.

The casing of the invar mount with one insert (round mirror side) secured inside was attached to an alignment stage theat allowed the tilt and yaw of the mount to be adjusted. This was placed on top of another 3D translation stage which allowed fine positioning of the mirror. Again, a collimated laser ensured the mirror was flat and straight. The second insert had an alignment rod bolted to the back with the other end attached to another tilt-yaw mount. This meant the angle of each section could be independently adjusted to ensure the fibres in the fibre array were perpendicular to the mirror chip. The cavity was observed through an optical microscope to coarsely align the fibre with one of the round mirrors on the chip. Figure 4.12 shows an example of the image seen.

Both piezo stacks were wired in parallel to a high voltage piezo driver (HVPZT E-507.36, PI). One fibre was spliced onto the optical setup (Section 6.2). This enabled the reflection spectrum of the cavity to be observed as the fibre and mirrors were being adjusted.

The two piezo stacks can then be dithered with a triangular ramp signal while monitoring the reflection of the cavity. The shear piezo stacks show a significant hysteresis at room temperature. This hysteresis can be measured by using the cavity reflection scans themselves. An example of the hysteresis is seen in figure 4.13. The scan shows points representing the reflection dips of the $m = n = 0$ modes of the cavity, like those in figure 4.5. These are separated by $\frac{\lambda}{2}$, the laser wavelength for this scan being $\lambda = 830\,\mathrm{nm}$. The piezo begins at $-236\,\mathrm{V}$ and is driven to $+236\,\mathrm{V}$ and back again. They are more widely spaced (in voltage) at the beginning of the scan in each direction and come closer together as the ramp progresses. This nonlinear behaviour must be accounted for when fitting the reflection spectrum to determine the finesse of the cavity. When the piezo stacks are cooled their travel reduces, as seen in the reduction of the slope of the hysteresis loops in figure 4.13. The nonlinearity also reduces and their response becomes more linear. The

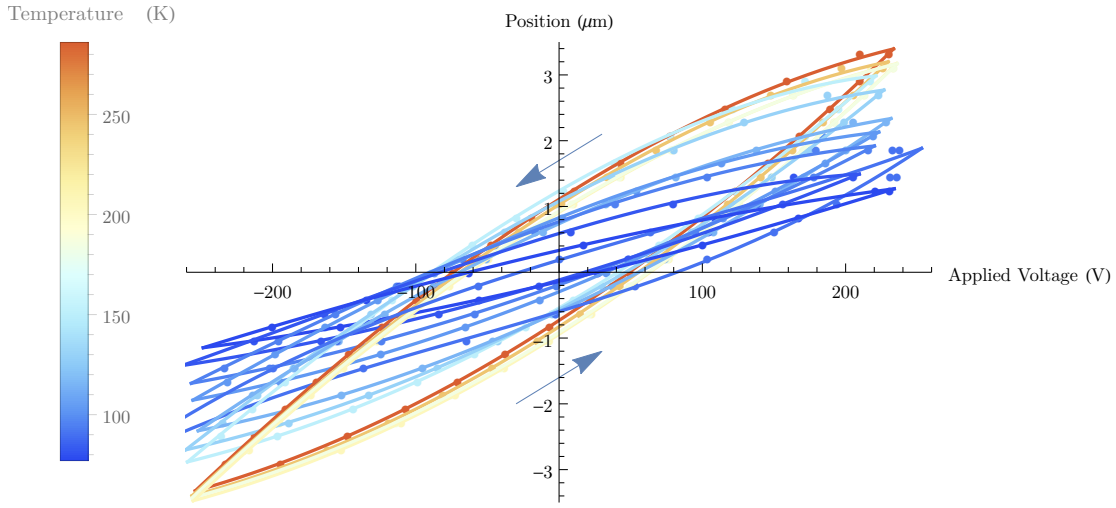


Figure 4.13: The hysteresis of the two piezo stacks measured using the transmission peaks of the cavity. This scan was taken with a triangular ramp with the direction of movement shown on the plot. Each dot represents the peak of a fundamental mode found during the scan. The fits are separate cubic polynomial functions for each direction. This is shown from room temperature down to liquid nitrogen temperatures.

cavity must be mounted on two, rather than a single, shear piezo stack to allow enough translation when the whole setup is cooled down. This is because the travel of the piezos is reduced to $\approx 10\,\%$ when at 2 K. At cryogenic temperatures it can only scan of the order $\frac{\lambda}{2}$, which is just enough to scan from one peak of the cavity to the next.

To align the cavity, I first bring a flat section of the mirror chip to within a few hundred microns of the v-groove array while scanning the piezo stacks. This produces a cavity of relatively low finesse (<10), confirming that the two mirror faces are parallel. Fine adjustment of the position of the fibre with respect to the mirror makes the low finesse cavity of the flat section firstly disappear (this is when the beam from the fibre is falling just within the boundary of the round mirror). More adjustment towards the centre of the mirror allows cavity reflection spectra like that of figure 4.5. Using the relative intensities and positions of the higher order modes of the cavity described above, the cavity can be adjusted to suppress transverse excitations and achieve the desired cavity length. Once the correct alignment is found, the screws are tightened to hold the cavity in place. When fixed, the cavity could withstand being moved around so it could then be placed into the bath cryostat with the cavity aligned.

The Nylon cavity was quite sensitive to temperature fluctuations due to Nylon's large coefficient of thermal expansion. This was found to be $1.4 - 1.7\%$ from 293 K to 77 K dependent on which direction it was measured in. The sintering process used to build the cavity is an additive layer process so the expansion parallel and perpendicular to the layers was different. This means that, once aligned to a length of 150 μm, the Nylon cavity could not be cooled without crashing the two mirrors into each other because of

the thermal contraction of the Nylon. The invar cavity mount was assembled in the same way as described above. The thermal expansion of invar is much less but the cavity length still shrinks by several microns. To insert the cavity mount into the bath cryostat it was attached to the end of the cryostat rod, which contains a number of electrical feedthroughs to connect the piezo stacks to the piezo drivers. The optical fibres from the cavity were fed through small holes drilled in Teflon ferrules mounted into Swagelock connectors.

The cryostat is a helium bath cryostat with a variable temperature chamber (Optibath UMC0063 SXM, Oxford Instruments). Inside, there is a liquid helium reservoir connected to the sample chamber by a needle valve. By opening this valve to admit a small flow of liquid helium and pumping on the sample chamber the temperature can be decreased down to 1.4 K. Down to 2 K is actively stabilised against fluctuations in the flow of the gas by a heater in the base of the cryostat which is controlled by the temperature sensor. To cool the cavity mount inside the cryostat, the helium reservoir is first precooled with liquid nitrogen. The nitrogen could also be directly fed into the variable temperature chamber and allowed us to conduct initial tests with the cavity at liquid nitrogen temperatures.

The initial cooldowns to liquid nitrogen temperatures were encouraging. The cavity sometimes remained aligned with high finesse (>100 at 77 K). However, this was not entirely repeatable, after dissembly and reassembly the cavity was sometimes not stable on cool down. This was because there was still enough distortion of the mount to misalign the cavity and the process of securing the insert using the grub screws was extremely sensitive. To secure the insert, each screw around the outer sleeve was very slowly tightened one by one, trying to keep the desired alignment. I found that tightening one screw inevitably led to translation in more than one direction at once, and even though the cavity could sometimes be aligned well, it was too difficult to ensure the v-groove array and the mirror chip remained parallel and well aligned simultaneously.

Initially, we also developed and built a flexure attachment for one mount of the cavity, shown in figure 4.14, which attaches to a different insert that slides into the outer casing. This was in case the alignment of the grub screws on the outer casing was not sensitive enough to optimise the cavity with the mount assembled. The flexure design used the inherent stiffness of the invar material to provide rigidity when aligning the cavity. It also prevented the coupling of the two directions which occured when all of the alignment was performed with just the grub screw on the outer casing. This flexure manages $\approx 11\,\mu$m travel along each axis but presents a significant hysteresis ($\approx 4\,\mu$m). The design has been modified and now has longer flexure hinges and grub screws on either side to allow a manual correction of the hysteresis. However, it still requires manual adjustment of the position of the central section. When the sample is inside the cryostat, this is not possible so the flexure design suffers the same drawback as the original mounts, namely that it moves when cooled.

Ideally, the cavity could be aligned actively and so be able to counteract any changes as the whole setup is cooling down. Thankfully, the cavity mount was also designed with

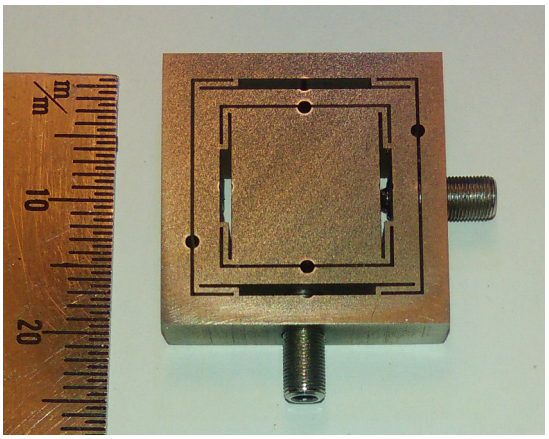


Figure 4.14: The flexure design which manages $\approx 11\mu m$ travel along each axis but presents a significant hysteresis ($\approx 4\mu m$).

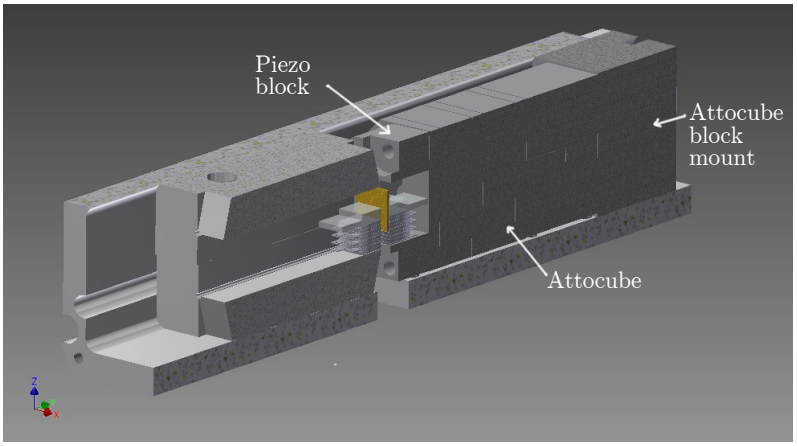


Figure 4.15: A cutaway of the cavity showing the attocube attached to the attocube block mount with piezo block on top.

just such an improvement in mind. The outer sleeve can also contain a block mount that holds an attocube 3D translation stage (3× ANPx101, Attocube), a slip-stick piezo driven translator with a resolution of 10 nm and a large scan range of 2 mm. The mirror chip and piezo stack were placed in another piezo block mount on top of the attocube. With this setup, it is now possible to realign the cavity as it is being cooled down. Figure 4.15 shows a cutaway of the cavity mount with the attocube placed inside the mount as opposed to the fixed insert seen in figure 4.9. The mount with attocube was coarsely aligned in the same way as above, but ensuring the v-groove array and mirror chip were parallel, then fine adjustment of the cavity was achieved using the attocube stack. When the cavity is assembled with the attocube stack the cavity lengthens during cooldown. This is because the attocube shrinks more than the outer casing. The length can be corrected using the attocubes as this is happening. We can now have an aligned cavity at 2 K due to the ability to realign the cavity during cooldown.

Although we were able to observe well aligned cryogenic cavities, the visibility and finesse of the cavity reduces as the cavity is cooled. This reduction of finesse and visibility ultimately meant that the cryogenic cavities were outside of the regime where we could observe the quantum mechanical effects we predict in chapter 5.

The origin of this reduction could either come from the cavity itself or from the effect of cooling on the crystal. To resolve these two possibilities, we cooled an empty cavity with no crystal to liquid nitrogen temperatures and still saw a reduction in the finesse and visibility, suggesting a change in the mirrors. The mirrors are made from dielectric coatings of Al_2O_3 and TiO_2 [1], whose thermal coefficients of expansion are $10.6\times10^{-6}\,\mathrm{K}^{-1}$ and $7.8\times10^{-6}\,\mathrm{K}^{-1}$ respectively[141, 142]. We have taken the larger value where there are different coefficients for different crystal directions. The dielectric mirror can be modelled using a ray transfer method (more on this in section 4.4) to find the reflection coefficient. This makes it possible to estimate the change in finesse due to the temperature variation of the mirrors. Assuming this coefficient is constant from room temperature to 2 K (in fact it decreases so this is an overestimate), we expect a change in the finesse due to thermal changes in the mirror to be and entirely negligible 0.04%. Even a length change in the mirror of 1% would change the finesse by $< 0.5\%$.

Eventually, I found that thermal cycling permanently damages the mirrors causing cracks and fissures in the coating and pulling it away from the surface. Figure 4.16 shows a photograph of the coated face of the v-groove array after several thermal cycles down to cryogenic temperatures and the same mirror surface after many ($>$12). Much of the coating has been removed from the v-groove array face. Mostly, from the lower half of the image which is the silicon block. The v-groove arrays were constructed from a silicon block with a pyrex lid. The silicon section of the v-groove array was more susceptible to cracking and flaking possibly due to the mismatch between the coefficients of thermal expansion. The thermal coefficient of silicon at room temperature is lower ($2.6\times10^{-6}\,\mathrm{K}^{-1}$) than pyrex at the same temperature ($4.8\times10^{-6}\,\mathrm{K}^{-1}$) and therefore further from that of Al_2O_3 and TiO_2. New, all pyrex v-groove arrays should stand up better to thermal cycling. However, this may not address the reduction in finesse seen during each cooldown, which is much greater than the slower degradation seen after many cooldown cycles. The same cavity will return to or near the finesse it showed before cooldown after it is warmed up again, and the cause of this reversible degredation is not clear.

The fact that the loss in finesse is also coupled with a reduction in the visibility suggests there could be an increase in the loss within the cavity which is causing the reduction. Residual gases in the cryostat could be forming ices on the surface of the mirrors which would increase scattering and introduce loss into the cavity. This idea needs to be tested with a more extensive purging procedure.

[1] The coatings are provided by O.I.B. GmbH with 15 alternating layers beginning and ending with a low refractive index layer. The layers are: 112.14 nm at $n = 1.75$ and 70.84 nm at $n = 2.77$. Herr Dr E. Schmidt reveals only these parameters. However, Al_2O_3 and TiO_2 are the most likely materials.

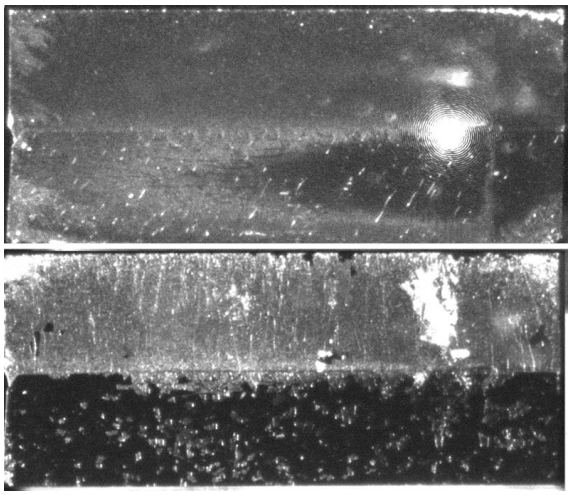


Figure 4.16: The effect of many thermal cycles on the state of the mirror coated on the v-groove array face. The top image is after only a few thermal cycles The laser spot is visible on the right side of the image. The lower image is after more than a dozen cycles. The flaking is seen predominantly on the lower silicon half of the assembly.

The reduction in finesse in turn reduces the coupling of a single molecule to the cavity and the reduction in visibility makes it difficult to detect the characteristic reduction in reflectance that would signal such a coupling. In order to be able to better observe this coupling we need to make several modifications to the cryogenic cavities.

4.4 Mirror Improvements

Once the current reversible degredation of the mirrors has been addressed and we have observed some coupling of single molecules to these microcavities, we would like to increase the reflectance of the mirrors in the cavity to drive the system into higher coupling regimes. So, I would like to present new mirror designs that will enable us to reach these regimes. The current experiment observes the interaction of the ZPL of single DBT molecule resonant with the cavity. For later experiments and single photon generation, the excitation of the molecule should be to a higher vibronic level to avoid background from the excitation laser. This means it would be beneficial to allow the v-groove array mirror to let the shorter (766 nm) light through the mirror to address the $S_{0,0} \rightarrow S_{1,3}$ transition.

The reflectance of the mirror can be calculated using a ray transfer matrix after Benisty *et al.* [143]. At an interface the reflectance for the s or p polarisations is given by the Fresnel coefficients

$$r = \frac{n_1 - n_2}{n_1 + n_2} \tag{4.26}$$

This is for a beam passing from a material of refractive index n_1 to a material of index

n_2. The reflected power is given by r^2 for both polarisations and the transmitted power is defined as $1 - r^2$.

At any interface there is a right-propagating field, $E_{\rightarrow}$, and a left propagating field, $E_{\leftarrow}$. We can define these quantities on the left side of the interface, $E_{l\leftrightarrow}$, and the right side of the interface, $E_{r\leftrightarrow}$. The left propagating field on the left side of the interface can be defined as the sum of the reflected field from the right propagating field on the left side and the transmission of the right propagating field from the right side of the interface

$$E_{l\leftarrow} = E_{l\rightarrow} r_{\leftarrow} + E_{r\leftarrow} t_{\rightarrow}, \tag{4.27}$$

where $r_{\leftarrow}$ is the reflection coefficient going right to left and $t_{\rightarrow}$ is the transmission coefficient from left to right. The other descriptions of the fields can be summarised by the matrix relation

$$\begin{pmatrix} E_{l\rightarrow} \\ E_{l\leftarrow} \end{pmatrix} = B_{\rightarrow} \begin{pmatrix} E_{r\rightarrow} \\ E_{r\leftarrow} \end{pmatrix}, \tag{4.28}$$

where the matrix $B_{\rightarrow}$ is

$$\begin{pmatrix} \frac{1}{t_{\rightarrow}} & -\frac{r_{\leftarrow}}{t_{\rightarrow}} \\ \frac{r_{\rightarrow}}{t_{\rightarrow}} & t_{\leftarrow} - \frac{r_{\rightarrow} r_{\leftarrow}}{t_{\rightarrow}} \end{pmatrix}. \tag{4.29}$$

There is also the matrix $B_{\leftarrow}$ which is the inverse of $B_{\rightarrow}$. Within one layer the field propagates according to the propagation matrix

$$D = \begin{pmatrix} e^{ikd} & 0 \\ 0 & e^{-ikd} \end{pmatrix}, \tag{4.30}$$

where k is the wavevector of the field propagating through distance d. The structure can then be built up of the product of matrices representing the interface and propagation through the layers,

$$\begin{pmatrix} E_{l\rightarrow} \\ E_{l\leftarrow} \end{pmatrix} = B_1 D_1 B_2 \ldots D_n B_n \begin{pmatrix} E_{r\rightarrow} \\ E_{r\leftarrow} \end{pmatrix}. \tag{4.31}$$

Assuming no incident field from the right, we can then solve for the reflectance and transmission for an incident field.

To describe the fibre end of the cavity with this method, we consider an initial region of refractive index 1 which is the air or vacuum in the cavity and then pairs of high and low index materials. Then finally there is a region of glass of index 1.45 which is the optical fibre. We can select a fixed number of pairs and then vary the thickness of the high and low index pairs until the reflectance at 784 nm is a high value and the reflectance at 766 nm is as low as possible. We choose these wavelengths because this is the wavelength of the

Reflectance (785 nm)	Reflectance (766 nm)	High Index (nm)	Low Index (nm)	Number of Pairs
98.5%	1.6%	88.48	114.3	13
99.8%	1.9%	111.57	67.31	21
99.95%	4.60%	106.34	77.93	22
99.99%	7.22%	246.13	75.48	21

Table 4.1: The new mirror designs that allow a high reflectance at the wavelength of the zero phonon line but permit transmission at the excitation wavelength.

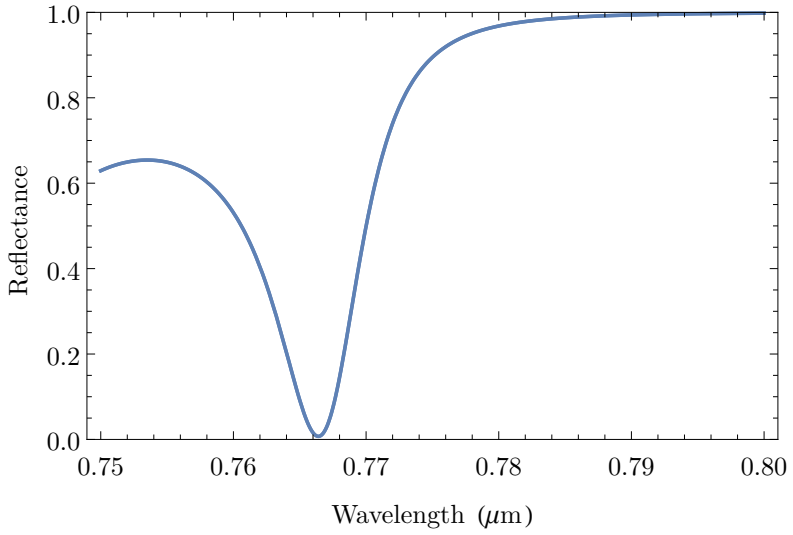


Figure 4.17: The reflectance spectrum of one of the new mirror designs over the relevant range. This has a reflectance of 98.5% at 785 nm and a reflectance of 1.6% at 766 nm.

transitions for molecules at the centre of the inhomogeneous distribution that we observe in our crystals.

By selecting a structure seen in table 4.1 we can have a mirror that has a reflectance spectrum like that seen in figure 4.17. This spectrum actually shows high reflectance out to 1 μm wavelengths and requires more pairs of high and low refractive index layers than we have currently on the v-groove arrays in order to have a high reflectance at 785 nm but also a sharp transition to low reflectance at 766 nm.

Eventually, we would like to build cavities with higher reflectances to move into the strong coupling regime. Incorporating the 766 nm pass band in the same way we can design mirrors for strong coupling cavities. In this regime the reflectance of the round mirrors must increase because the current value of 99.8% begins to limit the finesse of the cavity. Table 4.2 shows the predicted finesses and Purcell factors for particular mirror reflectance combinations. With this cavity geometry and higher mirror finesses, we can potentially enter the strong coupling regime, where the coupling between the molecule and the cavity is greater than the losses of both the cavity and the molecule. Cavity mirrors similar to ours have been used to support a reflectance of 99.998%, this is limited by the surface

Reflectance			
V-Groove Array Mirror	Round Mirror	Predicted Finesse	Purcell Factor
98.5%	99.8%	367	1.8
99.8%	99.99%	2989	14.3
99.95%	99.99%	10470	50

Table 4.2: A table of predicted finesse and Purcell factor for a single DBT molecule inside the cavity.

roughness of 2.2 Å[144]. Our mirrors would need to be subject to plasma smoothing as performed by Biedermann *et al.* to reduce the roughness from the 2 nm we currently see.

The current design of the cavity relies on excitation of the molecules by light in the cavity mode. Alternatively, we could consider exciting the molecule through the side of the cavity. Because the gap is small compared to the width of the v-groove array this is currently difficult. However, it is possible to remove material from the v-groove arrays so that the inside of the cavity is more accessible. For example, by polishing off the top corner of the v-groove array. There is also potential to excite from within the material of the v-groove array. This would mean shining light through the pyrex lid at an angle to the mirror face, so that the excitation beam is transmitted through the mirror though this would also benefit from modifying the reflectance spectrum of the v-groove array mirror as above.

With this next generation of the cryogenic cavities it will be possible to approach the strong coupling regime and make it easier to observe the cavity QED effects that the current cavities should have been able to observe.

CHAPTER 5

CAVITY QUANTUM ELECTRODYNAMICS

5.1 Introduction

In this chapter, I model the DBT molecule and the microcavity theoretically to simulate how the system behaves. Specifically, we can see how the reflection spectrum of the cavity is modified when it is resonant with a single molecule that is placed inside it. We can simplify the energy level structure of the DBT molecule, treating only the ZPL transition as a two level system and associate the $S_{0,0}$ state with the ground state $|g\rangle$ and the $S_{1,0}$ state with the excited state $|e\rangle$. This two level system interacts with just one mode of an idealised optical cavity. This field is expanded on the basis of Fock states, $|n\rangle$, where n is the number of photons in the cavity. This system is described by the well known Jaynes-Cummings model proposed in 1963 [64, 145]. This model is useful to gain an understanding of the molecule-cavity system. However, unlike the idealised system, the cavity is not perfect as the mirrors have limited reflectance. This means that the molecule is in fact coupled to a leaky cavity mode and the field will decay if it is not pumped. We include this in our model by a phenomenological damping of the field. The spontaneous emission of the molecule to modes outside the cavity is another decay channel for the molecule-cavity system. To account for this the molecule is also coupled to other modes of the electromagnetic field not in the cavity. We then obtain a modified master equation describing the dynamics with these two decay channels expressed by Lindbladian terms. This master equation allows the molecule-cavity system, complete with losses, to be simulated. We can therefore predict what the reflection spectrum of the cavity near the overlapping resonances of the cavity and molecule will be.

5.2 Jaynes-Cummings Hamiltonian

The Hamiltonian to describe a two level system interacting with a single mode of a cavity is the sum of the cavity field Hamiltonian, the free molecular Hamiltonian and the interaction

Hamiltonian [146],

$$\hat{H} = \hbar\omega_c \left(\hat{a}^\dagger \hat{a} + \frac{1}{2}\right) + \frac{1}{2}\hbar\omega_m \hat{\boldsymbol{\sigma}}_z + \hbar g \left(\hat{\boldsymbol{\sigma}}_- \hat{a}^\dagger + \hat{\boldsymbol{\sigma}}_+ \hat{a}\right). \tag{5.1}$$

where ω_c is the frequency of the resonant mode of the cavity, $\hbar\omega_m$ is the energy separation of the two level molecular system and g is the strength of the coupling between the two. $\hat{a}^\dagger$ and $\hat{a}$ are the creation and annihilation operator acting on the cavity mode. $\hat{\boldsymbol{\sigma}}_z$, $\hat{\boldsymbol{\sigma}}_+$ and $\hat{\boldsymbol{\sigma}}_-$ are Pauli operators acting on the two level system given by

$$\hat{\boldsymbol{\sigma}}_z = \begin{bmatrix} 1 & 0 \\ 0 & -1 \end{bmatrix}, \hat{\boldsymbol{\sigma}}_+ = \begin{bmatrix} 0 & 1 \\ 0 & 0 \end{bmatrix} \text{ and } \hat{\boldsymbol{\sigma}}_- = \begin{bmatrix} 0 & 0 \\ 1 & 0 \end{bmatrix} \tag{5.2}$$

when acting on $|\psi\rangle = \alpha|g\rangle + \beta|e\rangle$ expressed as a vector

$$|\psi\rangle = \begin{bmatrix} \beta \\ \alpha \end{bmatrix}. \tag{5.3}$$

The terms in this Hamiltonian correspond firstly to the energy of electric field, the energy of the molecule, and lastly the interaction potential between them. The interaction term then couples the molecule and the cavity,

$$\hat{H}_{int} = \hbar g \left(\hat{\boldsymbol{\sigma}}_- \hat{a}^\dagger + \hat{\boldsymbol{\sigma}}_+ \hat{a}\right). \tag{5.4}$$

The first term of the interaction Hamiltonian describes the de-excitation of the molecule and the creation of a photon in the cavity ($|e,0\rangle \rightarrow |g,1\rangle$). The second part corresponds to the excitation of the molecule and the annihilation of a photon ($|g,1\rangle \rightarrow |e,0\rangle$). This interaction term originates from the dipole interaction of the electric field with the molecule, expressed as

$$\hat{H}_{int} = -\hat{\mathbf{d}} \cdot \mathbf{E}. \tag{5.5}$$

The dipole of the molecule is $\hat{\mathbf{d}} = e\hat{\mathbf{r}}$, which (for simplicity) we take to be parallel to the field. Writing the dipole and the field as quantum mechanical operators [7], we have

$$\hat{H}_{int} = \langle e|e\hat{\mathbf{r}}|g\rangle \mathcal{E}(\hat{\boldsymbol{\sigma}}_+ - \hat{\boldsymbol{\sigma}}_-)(\hat{a} - \hat{a}^\dagger) \tag{5.6}$$

$$\hat{H}_{int} = \langle e|e\hat{\mathbf{r}}|g\rangle \mathcal{E}(\hat{\boldsymbol{\sigma}}_+ \hat{a} - \hat{\boldsymbol{\sigma}}_+ \hat{a}^\dagger - \hat{\boldsymbol{\sigma}}_- \hat{a} + \hat{\boldsymbol{\sigma}}_- \hat{a}^\dagger). \tag{5.7}$$

We neglect the highly off-resonant terms $\hat{\boldsymbol{\sigma}}_+ \hat{a}^\dagger$ and $\hat{\boldsymbol{\sigma}}_- \hat{a}$ that correspond to molecule excitation with photon production and to de-excitation with photon annihilation, to arrive at

$$\hat{H}_{int} = \langle e|e\hat{\mathbf{r}}|g\rangle \mathcal{E}(\hat{\boldsymbol{\sigma}}_- \hat{a}^\dagger + \hat{\boldsymbol{\sigma}}_+ \hat{a}). \tag{5.8}$$

The electric vacuum field, $\mathscr{E}$, energy integrated over the mode volume is equal to the energy of zero excitations,

$$\frac{1}{2}\hbar\omega_c = \int \epsilon_0 \mathscr{E}^2 dV, \tag{5.9}$$

which when rearranged gives an expression for the electric field amplitude,

$$\mathscr{E} = \sqrt{\frac{\hbar\omega_c}{2\epsilon_0 V}}. \tag{5.10}$$

Using the shorthand $d_{ge} = \langle e|e\hat{\mathbf{r}}|g\rangle$ we see, by comparing equation 5.4 and equation 5.8, and setting $\mathcal{E} = \mathscr{E}$, that the coupling strength, g, can be expressed as

$$g = \sqrt{\frac{d_{ge}^2\omega_c}{2\hbar\epsilon_0 V}}. \tag{5.11}$$

Here we note the inverse dependence on the mode volume of the cavity. That is, to encourage large coupling the mode volume of our cavity must be small.

The dipole moment, d_{ge}, of the molecule can be computed from the decay rate in free space that we worked out in section 1.4 in equation 1.13. This gives d_{ge} in terms of the observed decay rate as

$$d_{ge} = \sqrt{\frac{3\pi\epsilon_0\hbar c^3\Gamma_0}{\omega^3}}. \tag{5.12}$$

We need to employ a correction factor to get the radiation rate in a vacuum, Γ_0, which is modified in a medium to the value Γ according to [147]

$$\Gamma = n\left(\frac{n^2+2}{3}\right)^2\Gamma_0. \tag{5.13}$$

Γ is just the inverse of the measured lifetime of the molecule in section 3.6 which was $\tau_1 = 3.11\,\text{ns}$. Combining equations 5.12 and 5.13, yields a dipole moment of a single DBT molecule of 9.5 D in units of Debye (1 Debye $= {}^1\!/_{2.998\times10^8} \times 10^{-21}\,\text{C m}$).

The Hamiltonian given above acts on the state $|\Psi\rangle$. The state space is factorised into the tensor product of a two level state representing the molecule and a restricted number of cavity Fock states,

$$|\Psi\rangle \in \mathcal{H}_{molecule} \otimes \mathcal{H}_{cavity} \tag{5.14}$$

$$|\Psi\rangle = c_1|g,0\rangle + c_2|e,0\rangle + c_3|g,1\rangle + c_4|e,1\rangle. \tag{5.15}$$

When we expand this treatment to a leaky cavity and a decaying molecule we need to

express the molecule-cavity state as a density matrix,

$$\boldsymbol{\rho} = |\Psi\rangle\langle\Psi|. \tag{5.16}$$

The Hamiltonian evolution of our system is now expressed using the Heisenberg relation

$$\dot{\boldsymbol{\rho}} = -\frac{i}{\hbar}\left[\hat{H}, \boldsymbol{\rho}\right]. \tag{5.17}$$

This describes the excitation of the system exchanging energy, Rabi flopping, between the molecule and cavity field at a rate which is dependent on the detuning between the molecule and cavity resonances and also dependent on the strength of the coupling g. In reality, this exchange cannot continue indefinitely because the cavity mode is a leaky one and because the molecule can emit into external modes that are not in the cavity.

5.3 Decays

The cavity and the molecular excitations both have some finite lifetime for spontaneous decay to a continuum of states. This can be described by coupling each system to a large number of harmonic oscillators in a bath. Then after applying various approximations and tracing out the bath we can reveal the dynamics of the system [148]. This method is more rigorous but reveals the same dynamics as assuming the system evolves in non-unitary way. In practice, we do this by assuming the system undergoes evolution under an effective Hamiltonian.

The cavity starts with one photon inside represented by the state $|\Psi\rangle$. If the initial state emits a photon from the cavity, it will be in the state $|\Psi_{emit}\rangle$. Alternatively, it will undergo some evolution according to an effective Hamiltonian $\hat{H}'$ and be left in the state $|\Psi_{\cancel{emit}}\rangle$ [7]. This reasoning also applies for a molecule beginning in the excited state decaying to the ground state and emitting a photon to modes outside the cavity. Let us follow the decay of the cavity mode. After the cavity emits a photon to a leaky mode the new normalised state becomes

$$|\Psi_{emit}\rangle = \frac{\hat{a}|\Psi\rangle}{\langle\Psi|\hat{a}^\dagger\hat{a}|\Psi\rangle^{\frac{1}{2}}}. \tag{5.18}$$

When the state doesn't emit a photon it evolves for some short time, δt, and is expressed as

$$|\Psi_{\cancel{emit}}\rangle = \frac{e^{-\frac{i}{\hbar}\delta t\hat{H}'}|\Psi\rangle}{\langle\Psi|e^{\frac{i}{\hbar}\delta t\hat{H}'^\dagger}e^{-\frac{i}{\hbar}\delta t\hat{H}'}|\Psi\rangle^{\frac{1}{2}}}. \tag{5.19}$$

The effective Hamiltonian is

$$\hat{H}' = \hat{H} - i\hbar\frac{\kappa}{2}\hat{a}^\dagger\hat{a}, \tag{5.20}$$

where κ is the decay rate of the power in the cavity. The evolution then becomes

$$|\Psi_{\cancel{emit}}\rangle = \frac{\left(1 - \frac{i}{\hbar}\delta t\hat{H} - \frac{\kappa}{2}\delta t\hat{a}^\dagger\hat{a}\right)|\Psi\rangle}{(1 - \kappa\delta t\langle\Psi|\hat{a}^\dagger\hat{a}|\Psi\rangle)^{\frac{1}{2}}}. \tag{5.21}$$

This means that our, previously pure, state $|\Psi\rangle$ is now a mixed state best expressed using a density matrix. The probability of emitting a photon in the time interval δt is a product of this time, the cavity decay rate and the number of photons in the cavity $P = \kappa\delta t\langle\Psi|\hat{a}^\dagger\hat{a}|\Psi\rangle$. So the new state is expressed as

$$\boldsymbol{\rho}(t + \delta t) = P|\Psi_{emit}\rangle\langle\Psi_{emit}| + (1 - P)|\Psi_{\cancel{emit}}\rangle\langle\Psi_{\cancel{emit}}|. \tag{5.22}$$

using $\boldsymbol{\rho}(t) = |\Psi\rangle\langle\Psi|$ this becomes

$$\boldsymbol{\rho}(t + \delta t) = \boldsymbol{\rho} - \frac{i}{\hbar}\left[\hat{H}, \boldsymbol{\rho}\right]\delta t + \frac{\kappa}{2}\left(2\hat{a}\boldsymbol{\rho}\hat{a}^\dagger - \hat{a}^\dagger\boldsymbol{\rho}\hat{a} - \hat{a}\boldsymbol{\rho}\hat{a}^\dagger\right)\delta t. \tag{5.23}$$

For $\delta t \to 0$, this gives the master equation

$$\dot{\boldsymbol{\rho}} = -\frac{i}{\hbar}\left[\hat{H}, \boldsymbol{\rho}\right] + \frac{\kappa}{2}\left(2\hat{a}\boldsymbol{\rho}\hat{a}^\dagger - \hat{a}^\dagger\boldsymbol{\rho}\hat{a} - \hat{a}\boldsymbol{\rho}\hat{a}^\dagger\right). \tag{5.24}$$

where κ can be measured from the linewidth of the cavity fringes and so we can fully describe the evolution of the system.

This master equation acts on three possible states to give the dynamics of the system. The states are $|1\rangle = |g, 0\rangle$, $|2\rangle = |e, 0\rangle$ and $|3\rangle = |g, 1\rangle$. So we can write equation 5.24 as differential equations for the components of the density matrix $\boldsymbol{\rho}$ [149]:

$$\dot{\boldsymbol{\rho}}_{22} = ig(\boldsymbol{\rho}_{23} - \boldsymbol{\rho}_{32}), \tag{5.25}$$

$$\dot{\boldsymbol{\rho}}_{33} = -\kappa\boldsymbol{\rho}_{33} - ig(\boldsymbol{\rho}_{23} - \boldsymbol{\rho}_{32}), \tag{5.26}$$

$$\frac{d}{dt}(\boldsymbol{\rho}_{23} - \boldsymbol{\rho}_{32}) = -\frac{\kappa}{2}(\boldsymbol{\rho}_{23} - \boldsymbol{\rho}_{32}) + 2ig(\boldsymbol{\rho}_{22} - \boldsymbol{\rho}_{33},) \tag{5.27}$$

$$\dot{\boldsymbol{\rho}}_{11} = \kappa\boldsymbol{\rho}_{33}, \text{ and} \tag{5.28}$$

$$\boldsymbol{\rho}_{11} + \boldsymbol{\rho}_{22} + \boldsymbol{\rho}_{33} = 1. \tag{5.29}$$

These give the corresponding matrix equation

$$\frac{d}{dt}\begin{bmatrix} \boldsymbol{\rho}_{22} \\ \boldsymbol{\rho}_{33} \\ \boldsymbol{\rho}_{23} - \boldsymbol{\rho}_{32} \end{bmatrix} = \begin{bmatrix} 0 & 0 & ig \\ 0 & -\kappa & -ig \\ i2g & -i2g & i\kappa/2 \end{bmatrix} \begin{bmatrix} \boldsymbol{\rho}_{22} \\ \boldsymbol{\rho}_{33} \\ \boldsymbol{\rho}_{23} - \boldsymbol{\rho}_{32} \end{bmatrix}, \tag{5.30}$$

with eigenvalue solutions

$$\lambda_0 = -\frac{\kappa}{2} \tag{5.31}$$

$$\lambda_\pm = -\frac{\kappa}{2} \pm \frac{\kappa}{2}\sqrt{1 - \frac{16g^2}{\kappa^2}}. \tag{5.32}$$

Using Putzer's algorithm to find an analytical solution of the matrix equation 5.30 [150], the probability of finding the molecule in the excited state is

$$\boldsymbol{\rho}_{22}(t) = Ae^{-\lambda_0 t} + Be^{-\lambda_+ t} + De^{-\lambda_- t}. \tag{5.33}$$

The constants A, B and D are determined from the initial conditions. If we now assume what is known as the weak coupling regime where the decay rate of the cavity is larger than the coupling ($\kappa \gg g$) and that the system is originally in the excited state i.e. $\boldsymbol{\rho}_{22} = 1$. Then, after simplification, the state evolves like

$$\boldsymbol{\rho}_{22}(t) = e^{-\frac{4g^2}{\kappa}t}. \tag{5.34}$$

The excitation decays at a faster rate in the cavity than it would if the molecule was in free space,

$$\Gamma \to \Gamma' = \frac{4g^2}{\kappa}. \tag{5.35}$$

Now if we recall the definition of g from equation 5.11 and the quality factor of the resonance is $Q = \frac{\omega}{\kappa}$ then the decay rate becomes

$$\Gamma' = \frac{2d_{ge}^2 Q}{\epsilon_0 \hbar V}. \tag{5.36}$$

This is exactly what we got for the approach using Fermi's Golden Rule in Section 1.4 (Equation 1.19).

When the molecule and cavity are strongly coupled ($\kappa \ll g$) with the same initial condition the solution, again after simplification, becomes

$$\boldsymbol{\rho}_{22}(t) = e^{-\frac{\kappa}{2}t}\left(1 + \cos(2gt)\right). \tag{5.37}$$

This shows an oscillatory behaviour and demonstrates that the excited state undergoes

Rabi oscillations. The molecule emits a photon into the cavity but before the photon decays from the cavity it is reabsorbed by the molecule. The system then oscillates between the excited state of the molecule and a single photon in the cavity.

We want the presence of the cavity to enhance the emission of the molecule but do not want the system to be so strongly coupled that the system begins to show Rabi oscillations. It is desirable for our cavity to have a large coupling but still remain in the weak-coupling regime.

5.4 Simulations

We can simulate the behaviour of the molecule-cavity system without resorting to the simplifications of the weak and strong coupling regimes by numerically integrating the master equation. This will show the behaviour of the system at the boundary between weak and strong coupling where we intend to reside.

The spontaneous emission of the molecule to modes outside the cavity provides another term such that the full master equation has another term compared to equation 5.24,

$$\dot{\boldsymbol{\rho}} = -\frac{i}{\hbar}\left[\hat{H}, \boldsymbol{\rho}\right] + \frac{\kappa}{2}\left(2\hat{a}\boldsymbol{\rho}\hat{a}^\dagger - \hat{a}^\dagger\boldsymbol{\rho}\hat{a} - \hat{a}\boldsymbol{\rho}\hat{a}^\dagger\right) + \frac{\Gamma}{2}\left(2\hat{\boldsymbol{\sigma}}\boldsymbol{\rho}\hat{\boldsymbol{\sigma}}^\dagger - \hat{\boldsymbol{\sigma}}^\dagger\boldsymbol{\rho}\hat{\boldsymbol{\sigma}} - \hat{\boldsymbol{\sigma}}\boldsymbol{\rho}\hat{\boldsymbol{\sigma}}^\dagger\right) \tag{5.38}$$

where Γ is the free space decay rate of the molecule.

We will actually be observing the reflection from the cavity. So the system is being driven by a classical field. The Hamiltonian we actually use is the driven Jaynes-Cummings Hamiltonian. So, our familiar Jaynes-Cummings Hamiltonian has some additional terms which represent the external driving field of the laser,

$$\hat{H} = \hbar\omega_c\left(\hat{a}^\dagger\hat{a} + \frac{1}{2}\right) + \frac{1}{2}\hbar\omega_m\hat{\boldsymbol{\sigma}}_z + \hbar g\left(\hat{\boldsymbol{\sigma}}_-\hat{a}^\dagger + \hat{\boldsymbol{\sigma}}_+\hat{a}\right) + \mathcal{E}e^{i\omega t}\hat{a} + \mathcal{E}^* e^{-i\omega t}\hat{a}^\dagger. \tag{5.39}$$

It is the inclusion of these driving terms and the Lindbladian terms in the master equation which means it cannot be generally analytically solved [151].

This Hamiltonian can be expressed in the rotating wave approximation with some substitutions made to offset the total energy ($\Delta = \omega_m - \omega$, $\delta = \omega_c - \omega$) and choose a phase of the driving field to make the components of the master equation real ($\hat{a} = i\hat{a}$, $\hat{a}^\dagger = -i\hat{a}^\dagger$). We have also dropped any constant terms to give

$$\hat{H}^* = \hbar\delta\hat{a}^\dagger\hat{a} + \hbar\Delta\hat{\boldsymbol{\sigma}}_z + i\hbar g(-\hat{\boldsymbol{\sigma}}_- a^\dagger + \hat{\boldsymbol{\sigma}}_+\hat{a}) + i\mathcal{E}(\hat{a} - \hat{a}^\dagger). \tag{5.40}$$

This is now the Hamiltonian that is substituted into the equation 5.38. The value of κ is calculated from the measured finesse, $\mathcal{F}$, and free spectral range (FSR= $\frac{c}{2L}$) of the cavity

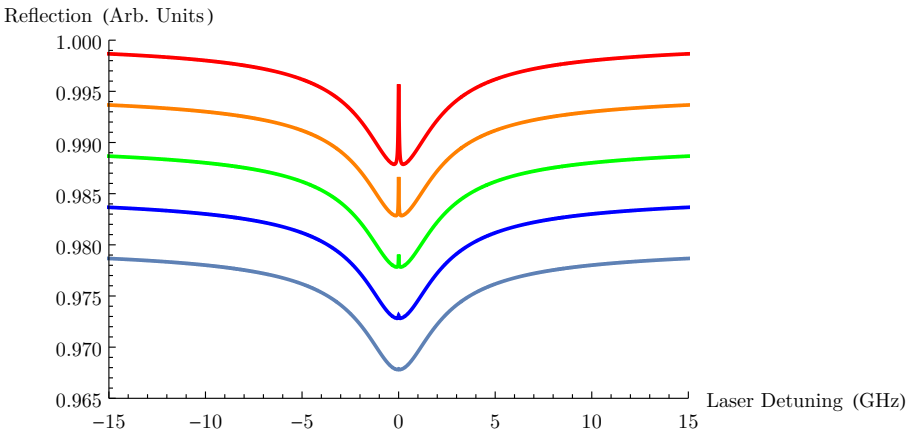


Figure 5.1: A graph showing the expected ratio of reflected power to that incident on the cavity as the laser is detuned across resonance of the cavity and molecule. The coupling factor is $2^s\, g_0$ where from top to bottom $s = 2, 1, 0, -1, -2$ (Plots are offset for clarity).

given as

$$\kappa = \frac{c}{2\mathcal{F}L}. \tag{5.41}$$

This gives a value of $\kappa = 2\pi \times 6.6\,\text{GHz}$. The value of Γ is given by the measured lifetime, $\tau_1 = 3.11\,\text{ns}$ from the $g^{(2)}(\tau)$ measurement such that

$$\Gamma = \frac{1}{\tau_1}, \tag{5.42}$$

meaning $\Gamma = 2\pi \times 51\,\text{MHz}$. We can estimate the coupling term by writing the volume of the cavity is the input mode area times its length $\pi w^2 L$. Recalling the coupling strength from equation 5.11, the expected coupling term is equal to $g_0 = 2\pi \times 98\,\text{MHz}$ for the cryogenic cavities described in section 4.3. The value of the driving field can be given by

$$\mathcal{E} = \sqrt{\dot{N}\frac{\kappa}{2}}, \tag{5.43}$$

where $\dot{N}$ is the rate of photons incident on the cavity. The master equation can be solved in the steady state by setting $\dot{\boldsymbol{\rho}} = 0$ and using matrix representation of the operators $\hat{a}$, $\hat{a}^\dagger$, $\hat{\boldsymbol{\sigma}}_+$ and $\hat{\boldsymbol{\sigma}}_-$ on a restricted Hilbert space given in equation . Each term of the density matrix can then be determined by solving the set of linear equations which are given. I did this using Mathematica and end up with a large expression for each term of the density matrix. The expected number of photons in the cavity is then $Tr[\boldsymbol{\rho}\hat{a}^\dagger\hat{a}]$. As the cavity has a decay rate of κ (assuming loss through the first mirror dominates) the transmission from the cavity is then $T = \kappa Tr[\boldsymbol{\rho}\hat{a}^\dagger\hat{a}]$. We then expect the normalised reflectance to be $(\mathcal{E} - T)/\mathcal{E}$. Figure 5.1 shows this normalised reflectance of the cavity as a function of the driving frequency for number of coupling strengths. We expect a strength of g_0 given

above and this would show a increase in the reflectance of 9.9% of the size of the cavity dip. Even with a coupling of half that expected the increase in reflectance will still be 2.6% of the depth of the cavity dip seen in reflection scans of the cavity. We note that the coupling of each molecule to the cavity depends on the orientation of the molecule and its position on the standing wave of the cavity mode. In order to simplify the analysis above, we let the molecule be parallel to the field and also ignored the standing wave pattern, coupling instead to the RMS field. These effects are easily taken into account.

CHAPTER 6

EXPERIMENTAL SETUP

6.1 Reflectance Measurements

As presented in the previous chapter, we can measure the strength of the coupling of the single molecule to the optical fibre microcavity by observing its reflection spectrum. This will exhibit a broad dip due to the cavity resonance, on which a narrow peak is superimposed. To stay within the regime simulated in Chapter 5, that is the restricted Hilbert space, we need to observe the spectrum at low light levels so that the number of photons in the cavity is never more than one. I will describe below the sources we have built and used to address various different transitions in the DBT molecule for the characterisation. Then I will describe the optical setup to carry out the reflection spectrum measurements. Finally, I describe the liquid helium crysostat and show a spectrum taken with a cold cavity.

6.2 Optical Setup

The experiment uses three lasers. A Coherent MBR-110 Ti:Sapphire laser excites the zero-phonon transition in the molecule, a homebuilt external-cavity diode laser (ECDL) at 830 nm lets us stablise the microcavity, and a diode laser at 767 nm drives the $S_{0,0} \rightarrow S_{1,3}$ excitation transition. I now descrive these in turn.

The Ti:Sapphire operates with the mid-range filter set, which gives it a tuning range of 769.5 nm-870 nm. An internal locking cavity stabilises the frequency and also allows us to scan the laser up to 40 GHz. Before passing to the rest of the experiment, the light from this laser is first passed through an acousto-optical modulator (AOM) (M080-2B/F-GHZ, Gooch and Housego). The AOM is driven by an 80 MHz rf signal and we used first order of the diffracted beam. This allows us to vary the intensity of the beam and stabilise it against power fluctuations. The amplitude of the rf signal is controlled by a PID controller (SIM960, Stanford Research Systems). The set point of the PID loop is given by a laser monitor photodiode further down the optical setup.

The external cavity diode laser (ECDL) at 830 nm uses a HL8338MG Diode (50mW)

from Opnext and a 1200 lines/mm grating in a Littrow configuration placed with 44.3° between its normal and the optic axis of the diode. The diode and grating are both mounted on a modified tip/tilt mount and on top of a TEC heater/cooler. A Pt100 thermistor placed near the diode provides feedback to the heater which is powered by a PID temperature controller (TED200C, Thorlabs). This has the integral gain disabled so it is acting as a simple proportional controller to prevent oscillations. This allows us to tune the wavelength between $820 - 831$ nm. The tip/tilt mount can be coarsely adjusted with thumbscrews. It also has a piezo to scan the angle of the grating, controlled with a single channel piezo driver (MDT694A, Thorlabs). The laser diode itself is driven by a LDC205C current source again from Thorlabs. Figure 6.1 shows how we control and monitor the light from this laser. The output beam is spatially filtered by a fibre and then split in two by a pellicle. The transmitted part goes to a scanning Fabry-Pérot (FP) cavity (SA210-B, Thorlabs). The free spectral range of this cavity is 10.6 GHz and it has a finesse of 123. The signal from detector 100A/EC is normalised by detector 100A/M to eliminate power fluctuations and then fed back to the diode laser (using a Stanford Instruments SIM900 PID controller) to lock its frequency on the side of the FP transmission fringe. The laser frequency is scanned by scanning the FP cavity. The light reflected at the pellicle goes through a fixed quartz cavity with a shorter free spectral range (1.49 GHz) and a lower finesse (1.7), which allows us to monitor the frequency of the laser during the scan. The voltage that is applied to the FP piezo is also attenuated and fed forward to the grating piezo of the ECDL laser. This prevents the ECDL from mode hopping and extends the scanning range of the laser to ≈ 10 GHz, which is just enough to cover one fringe of the cryogenic cavity.

The very first cavities we built before developing the cryogenic cavity mount, described earlier, were based on single fibres without any v-groove array. These did not present a very large area on which to place the DBT doped anthracene crystals and so we began using the v-groove arrays. These single fibres also suffered from some instability due to the shaking of the fibres. Therefore, we began building into the cavity experiment several locking loops to get around this cavity instability. When we moved to the fibre v-groove arrays, the cavities became much more stable and the complex locking became unnecessary. However, the slow temperature drifts and instabilities of the cavity inside the cryostat mean that the cavity will have to again be actively locked to be able to observe the cavity QED effects considered in chapter 5.

The 830 nm light provides a locking signal from the cryogenic microcavity which is still within the high reflectance band of the mirrors but is sufficiently far from the zero phonon line that the light can be filtered out from the reflection signal at 785 nm. The microcavity (locked to this laser) can then be scanned in a repeatable way by changing the length of the scanning FP cavity.

The diode laser at 767 nm is a distributed feedback (DFB) device LD-0767-0015-DFB-1 from Toptica. It does not need to be stabilised by an external cavity because the DFB

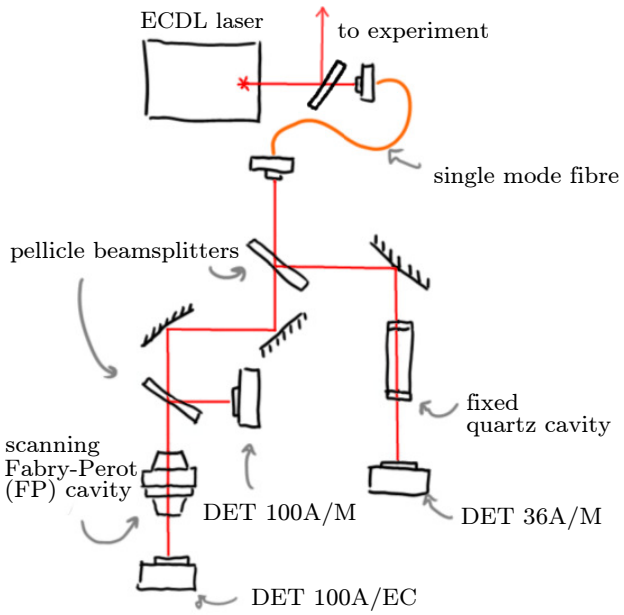


Figure 6.1: Laser locking setup with FP cavity for locking the ECDL laser with a normalisation detector (DET100A/M). The frequency of the ECDL laser can then be changed by scanning the length of the FP cavity. The fixed quartz cavity is for monitoring the frequency during the scan.

grating structure already provides sufficient stability for exciting the wide $S_{0,0} \rightarrow S_{1,3}$ transition. We cannot use the Ti:Sapphire laser for this incoherent pumping because 767 nm is outside its tuning range.

Each of these lasers, by a series of flip mirrors, can be coupled to a polarisation maintaining fibre, which connects to the optical setup of the cavity or the confocal microscopes. More than one laser can also be combined using a polarising beamsplitter so that, for example, the cavity can be locked to the 830nm light, while also being probed by the Ti:Sapphire around the zero phonon line of the molecules.

The original optical setup of the cavity reflection experiment, shown in figure 6.2, used fibre beamsplitters. The advantage of using fibre is that there are fewer coupling losses going to and from single mode fibres. The light from the laser in a PM fibre is butt-coupled to the first fibre beamsplitter, which sends 90% to a laser power monitor (PDA10A/M). This signal controls the rf for the AOM (not shown) that stabilises the power from the Ti:Sapphire. The remaining 10% goes on to the second fibre beamsplitter through a splice joint that minimises the junction loss. 90% of this light is lost to the calibration port and the remaining 10% goes on to the fibre polarisation controller. This consists of three paddles that have circular grooves in them, each having a number of turns of fibre inside (1 loop, 2 loops and 1 loop). The loops make the fibre birefringent by stressing it, so that it can act as a waveplate. By varying the orientation of the paddles, the angle of the induced

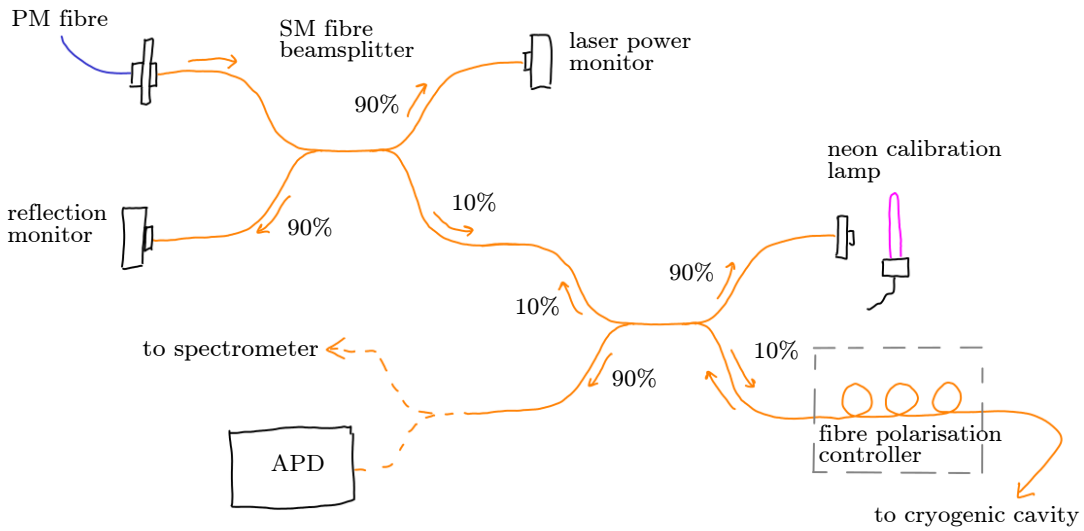


Figure 6.2: The fibre optic setup for observing the cavity reflection spectrum of the cryogenic cavity.

birefringence changes and the polarisation of light can be rotated. The fibre then goes to the cryogenic cavity. Upon reflection from the cavity the light passes back through the fibre polarisation controller and returns to the second beamsplitter, where 90% of the light is sent either to the APD or to the spectrometer. The other 10% enters the first fibre beamsplitter and 90% of that light is sent to the reflection monitor photodiode (PDA100A/M).

This optical setup was used to get many of the reflection spectra from the cavity setup while at room temperature and during several of the cooldowns. As mentioned before, the visibility and finesse of the cavity both deteriorated during cooling. This made the dip in the reflectance of the microcavity very small, and therefore particular hard to see against fluctuations in the laser power. The laser power was normalised to the laser power monitor but the cavity signal was still varying by 5%. This noise seems to come from the fibre couplers. The splitting ratio of the fibre is dependent on the polarisation of the incident light. When the cavity is inside the cryostat, the bare fibre running from the top of the cryostat insert to the cavity is subject to temperature fluctuations and shaking. This made the whole fibre act as a varying wave plate rotating the polarisation of light. The fact that the fibre beamsplitters have a polarisation dependence means this polarisation noise was transferred to intensity noise.

I solved this problem by switching to free space beamsplitters because they are less sensitive to the polarisation noise, and thus having less fibre to generate the noise in the first place, as shown in figure 6.3. The laser light in a polarisation maintaining fibre is coupled to free space and sent through a half-wave plate and then a polarising beamsplitter to clean up the polarisation. The light then falls on a beamsplitter and half of the light goes to the laser power monitor. The other path passes through a neutral density filter

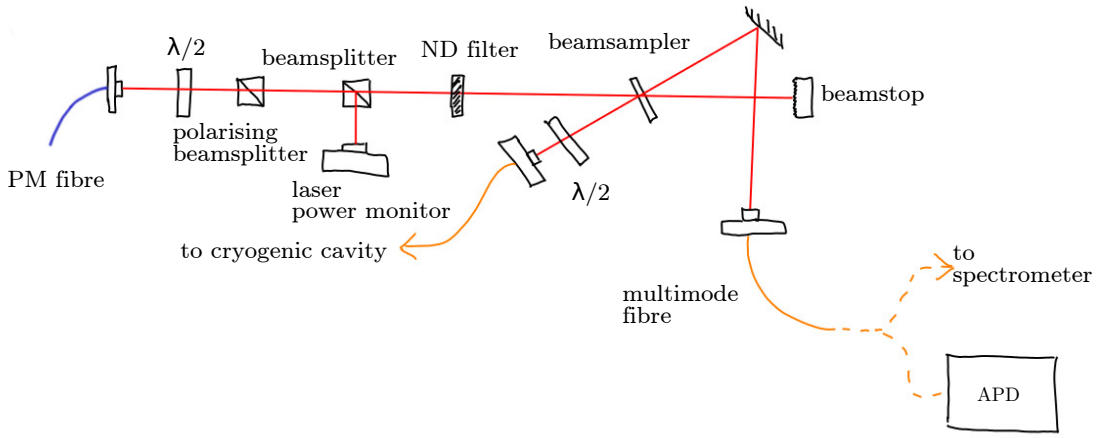


Figure 6.3: The free space setup for measuring the reflection spectrum of the cryogenic cavity.

and is reflected from a glass slide acting as a beamsampler. This light passes through a half-wave plate that adjusts the plane of the linear polarisation before coupling into a single mode fibre which is spliced onto the cryogenic cavity fibre. The light reflected from the cavity then passes through the beamsampler and is coupled into a multimode fibre that takes it to an APD or to the spectrometer.

We take reflection spectra of the cavity by scanning both the length of the cavity and the wavelength of the excitation laser in order to have a two dimensional view of the cavity resonance and the zero phonon line of a single DBT molecule. When we perform this scan on an empty cavity at room temperature, as shown in figure 6.4, we see just the cavity resonance shifting as the frequency of the laser is varied. When a molecule is coupled to the cavity, it will appear as a reduction in the reflection of the cavity for each scan of the cavity length as in figure 5.1 for just one laser frequency. This feature will be at a defined frequency and so appears as a horizontal line in the plot at the resonance frequency of the molecule.

A diagram of the cryostat is seen in figure 6.5. The helium syphon and the outer vacuum chamber (OVC) of the cryostat were first evacuated by a turbo pump (TurboV 81 M, Agilent), backed by a roughing pump (IDP-3, Agilent). The OVC was constantly pumped during the cooldown via the OVC port. The cavity was then transferred into the sample chamber, also called the variable temperature insert (VTI) chamber, on the end of its rod. Frequently, the mechanical disturbance of this was enough to misalign the cavity. For the first incarnation, this meant taking the cavity out of the cryostat, realigning it and then putting it back in (and repeating until the cavity stayed aligned). After the attocubes were added, realignment just required adjustments of the attocube. Then we evacuated the sample chamber through the VTI port.

The next step was to purge the cryostat with nitrogen in order to remove other condensible gases. Opening the needle valve to connect the helium reservoir and the VTI

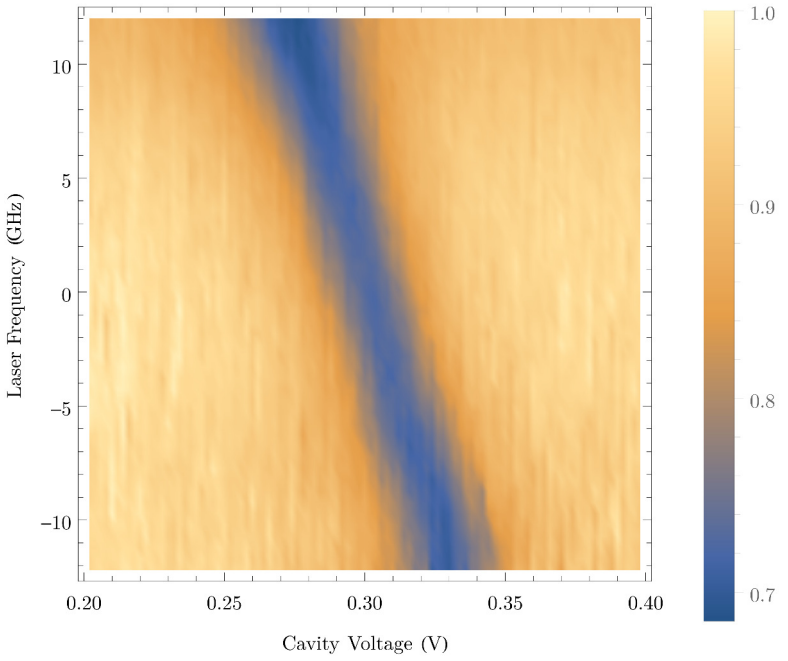


Figure 6.4: The reflection spectrum of a single peak of the microcavity varying both the microcavity length and the excitation laser frequency.

chamber, the two chambers were purged together by connecting the roughing pump (Sogevac SV100B, Oerlikon Leybold) to the helium reservoir gas port and evacuating. Then we purged both with nitrogen gas through the gas inlet port monitoring the pressure with the gas bladder. The VTI chamber port and helium reservoir fill port were closed off during the purge. The chamber was purged three times allowing at least 5 min for the gas to work its way through the needle valve. Then, the needle valve was closed to isolate the two chambers.

Once purged, a one way valve was connected to the helium reservoir gas port (CV-125B-.15, Generant) and then connected to an extraction system. We swapped the pump onto the VTI chamber port and evacuated the VTI chamber. We then filled the helium reservoir with liquid nitrogen. The helium reservoir fill port has an O-ring compression fitting for securing the helium siphon in place. The nitrogen filling siphon has a smaller diameter and, therefore gives a loose fit, which prevents the helium reservoir from over-pressuring. This means that the cold nitrogen gas leaves through this port as well as the helium reservoir gas port. The O-ring is liable to freeze and crack during this part of the fill. So, we heated the fill port with heat gun to stop that.

For the preliminary nitrogen cooldowns, we then closed the fill port and opened the needle valve to admit nitrogen into the VTI chamber. The resulting temperature changes could lead to misalignment. If this happened, it indicated that the fibre array and mirror were not parallel to each other or to the outer casing. So, the cavity would need to be

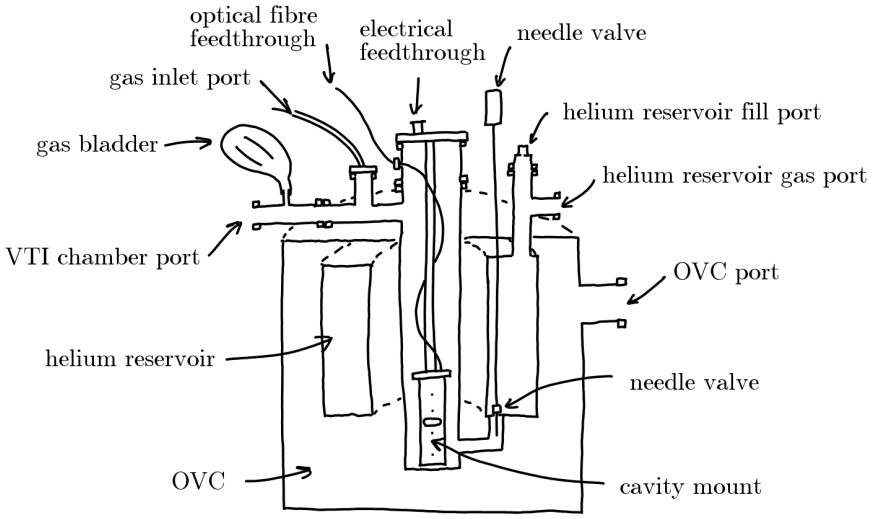


Figure 6.5: The connections and ports of the helium bath/flow cryostat. The two chambers, the helium reservoir and the VTI chamber, are housed inside the outer vacuum chamber (OVC). The two chambers are connected by a needle valve and both have several ports to admit gases and liquids.

removed and realigned. We monitored the temperature using two temperature sensors: one in the base of the VTI chamber and one on the insert rod. As the cavity cooled we could correct for small misalignment of the cavity by correcting the position of the attocubes. When the temperature approached 77K care had to be taken that the pressure in the VTI chamber did not drop too low. Pumping on the nitrogen too hard would freeze the liquid nitrogen in the VTI chamber and damage the cavity.

We next siphoned the remaining liquid nitrogen out of the helium reservoir and then left the cryostat for an hour to let all the remaining liquid evaporate. Before putting any helium into the cryostat, we again purged both chambers. This time with helium gas to remove all the remaining nitrogen. We did this in the same way as above by swapping the pump to the helium gas port and opening the needle valve, purging three times and then swapping the pump back. The chambers are best left slightly overpressured to stop gas getting into the chambers during the quick swaps.

The helium reservoir could then be filled from the liquid helium dewar using the evacuated siphon. The filling rate is critical to minimise helium loss: too slow and helium boils off too quickly to accumulate in the helium reservoir, too fast and the violent filling causes excessive boil off. The reservoir should take about half an hour to fill. Once full the VTI chamber was evacuated and the needle valve opened slightly. This begins the cooling of the cavity. Again speed is critical, $2-3\,\mathrm{K/min}$ is an ideal cooling speed.

At any point during the cooling procedure if the chambers are not well purged there is a risk of the needle valve clogging and freezing. This means that the needle valve will no

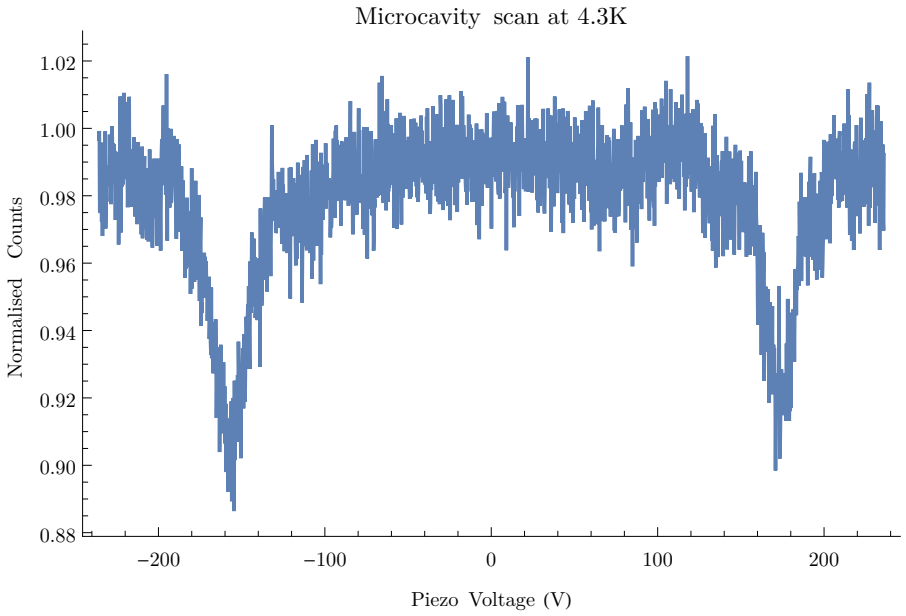


Figure 6.6: A scan of the microcavity at 4.3 K. The finesse of the cavity is 8.4 with a visibility of 7.7%.

longer turn and need to be unclogged. Sometimes this can be achieved by turning on the needle valve heater. A jumper cable rewires the heater power source to the needle valve heater. This can then be set to 12 V for a maximum time of 15 min. If this fails to unclog the valve the cryostat has to be left to warm up until the valve unclogs and then restart the cooling procedure. It can take up to a day.

When the cavity reached a low temperature, we engaged the VTI chamber heaters to stabilise the temperature. The heaters are connected to a PID loop which holds the temperature at $2\,K$. On short timescales this temperature is quite stable, however while there still exists some temperature gradients across the cavity there is a drift in the cavity length over timescale of several seconds. Though the temperature held for tens of minutes at a time occasionally there were very large jumps in the temperature of the VTI chamber sensor. This was accompanied by a increased flow through the one-way valve at the helium reservoir gas port. The would mean there is a decrease in pressure above the helium in the reservoir. This pressure decrease reduces the flow of helium into the VTI chamber. Therefore, the temperature increases.

Despite these instabilities it was possible to measure a reflection spectrum from the cryogenic cavity. The reflection spectrum is shown in figure 6.6. This scan was performed at 4.3 K with a incident laser power of 0.5 pW at a wavelength of 784.02 nm. The cavity fringes have a finesse of 8.4 with a visibility of 7.7%, much reduced from the room temperature scans presented in chapter 4. There are 2000 points in the scan, each one accumulated for 5 ms. This is a relatively short time to perform the scan in but longer scans were not possible due to the drift in cavity length. It is also possible that the peaks in

this scan are broadened by drift during the scan. It was this instability combined with the reduction in finesse of the cavity that meant it was not possible to observe the reflection spectrum of a single molecule inside the cavity and therefore measure the coupling.

Reinstating the previously used cavity locking combined with the modifications to the mirrors presented in section 4.4 mean these measurements can be carried out for longer times and reduce the noise seen in figure 6.6 and observe the features of the reflection spectrums from chapter 5. Despite the current shortcomings, I have successfully developed a cryogenic microcavity that remains aligned at the temperatures required to give narrow emission from DBT molecules.

CHAPTER 7

SUMMARY AND OUTLOOK

7.1 Summary

DBT doped anthracene crystals are an ideal system to use in single emitter experiments. I have developed a cosublimation method for growing DBT-doped anthracene crystals of good optical quality, that are suitable for use in single emitter cryogenic cavity experiments. A crystal growing oven with active control of both the two separate material crucibles and the collection plate allowed growth of DBT doped anthracene crystals at a controlled density over an order of magnitude. This density is ideal to enable the single DBT molecules to be used as a source of single photons. The crystals were extensively characterised. The density, orientation, saturation and second order correlation function were measured in a room temperature confocal setup. This confirmed the molecules are indeed single emitters well located in the anthracene crystal. The DBT spectra were also measured in a cold confocal setup, where we observed emission linewidths down to 55 MHz. The variation between molecules of the zero phonon line was such that, at the centre of the inhomogeneous broadening we expect one molecule to be in the mode of the cavity and be within the 40 GHz scanning range of the Ti:Sapphire laser.

I have succeeded in building cryogenically compatible fibre based microcavities that we will use to enhance the emission of single dye molecules. Cavities were first developed in a nylon material showing good stability of the fibre cavity. To enable them to be cooled to cryogenic temperatures the same design was made in Invar. Although the Invar was more stable, as the temperature was lowered, the strict alignment requirements meant that an attocube needed to be incorporated into the final design. The fibre cavities can now be aligned as they cool down and show reflection spectra at cryogenic temperatures.

The contrast and finesse of the cavity reduces as the cavity is cooled down. This may be due to ices forming in the cavity as it cools and a more thorough purging procedure can prevent the formation of ices. The optical setup for measuring the reflection spectra has been modified from its original all fibre conception to a free space setup due to the polarisation noise from the optical fibres. I have presented the designs of new microcavity mirrors with higher reflectances and pass bands. These will mean the finesse of the

microcavities can be increased, making it easier to see the cavity QED effects we expect.

The cavities also show a slow drift when they are cooled to cryogenic temperatures. This could be down to the temperature fluctuations within the cryostat. This drift is of the order of a few MHz/s. in future that drift will be removed by actively locking the cavity to another laser beam that would stabilise the slow drift, a scheme that has already been demonstrated at room temperature with the original cavities.

By observing the reflection spectrum of the coupled cavity-molecule system, we will measure the strength of the coupling between single DBT molecules and the cavity. The expected coupling should give a narrow peak in the reflectance of the cavity when the molecule is resonant with the cavity as I have shown with simulations of the molecule-cavity system. The coupling will be position dependent it is proportional to the local electric field. Even if the coupling is a factor of two weaker than the peak value, we should still see a signal in the cavity reflection spectrum with the current mirrors, once we overcome the current loss of finesse on cooling.

7.2 Outlook

Once the coupling has been measured we will alter the excitation scheme to use the cavity for single photon production. The new mirror design outlined in section 4.4 will allow a more efficient excitation scheme and will also permit higher reflectances of the mirrors around the zero phonon line, leading to higher Purcell factors. An important benefit of this would be a reduction of the mode density at the red-shifted frequencies of the vibronic transitions. This will help to improve the yield of photons on the zero phonon line.

Alternatively, we could excite the molecules without driving the cavity mode at all. This can be accomplished in a variety of ways. The v-groove arrays are made of pyrex, so a collimated excitation beam could be directed through the material of the array itself. Also, the high refractive index of the anthracene crystal may be exploited to guide the excitation light along it. This would mean focussing the light onto the edge of the anthracene crystal. Both of these approaches get around the current shape of the gap between the v-groove array and the mirror chip which provides little optical access. The v-groove array block can have some material removed from the corner of the pyrex top. This would open up the cavity meaning it would be possible to shine light onto the inside of the cavity from an optical fibre or lensed fibre.

In addition, it is possible to have two cavities aligned simultaneously on the same v-groove array. This would enable the locking of the cavity length to be done on an adjacent cavity and would mean none of the locking light would have to be inside the cavity that contains the molecule. Currently, the spacing of the round mirror arrays does not match the pitch of the v-groove arrays so this is not possible with the present cavity mirror set.

The current cavities are designed to be easily assembled and disassembled so that they could be tested with and without crystals to isolate any changes in the cavities when the

crystals are placed inside them. The unprotected anthracene crystals sublime away over time. So, the cavity must also be disassembled to put a new crystal inside. When the cavity is cold this is not a problem but at room temperature the crystal remains smooth for only around 48 hours, then begins to affect the finesse of the cavity. The encapsulated crystals mentioned in section 3.4 could provide a means of protecting the crystals so that they remain viable for longer. The PMMA films should be too thin to affect the finesse of the cavity too much and when spin coated can be very smooth as well.

With the same encapsulation technique we can produce thin films that contain DBT doped anthracene crystals. These crystals can be produced by spin coating [103] or by an overcoating method [152]. It is also possible to grow nanocrystals of anthracene [153]. These crystals may have DBT incorporated into them by adding DBT to the solution. Should the DBT be well located in these crystals then they can also be protected in PMMA films. These nanocrystals can get around the fact that the DBT is housed in a high index material. For the microcavity setup that we currently have this is not too much of an issue because the light is always propagating perpendicularly to the surface of the crystal. For some of the other photonic structures like waveguides [54], this is a bigger problem [152]. Large quantities of anthracene on top of the waveguide disrupts the waveguide mode and severely increases the loss. The various encapsulated crystals can reduce this effect.

More investigation into the DBT molecules themselves would lead to more insight into the origin of the inhomogeneous broadening. I have discussed in section 2.2 DFT simulations of the DBT molecules in free space, but their conformation in the anthracene crystals is slightly different. Classical force fields of anthracene have been developed and tested so the geometry of DBT in anthracene can be simulated, as it was by Nicolet *et al.* [154, 60]. By using this classical optimisation and performing DFT simulations on these geometries we could examine how the slightly different geometry changes the transitions in the DBT molecule. We could then examine how tightly bound the DBT molecules are in their surrounding environment.

We are interested in trying to locate the triplet state of the DBT molecule. The energy of the triplet state is not known and the low probability of intersystem crossing and possible nonradiative decay make this a difficult task. In addition, the DFT simulations of the excited states of such large molecules are notoriously unreliable. It is encouraging that the high emission rate of the DBT on the zero phonon line means that the detection of the state could be done using the method of shelving. The lifetime of the triplet state is much longer than that of the excited singlet. Therefore, driving the molecule into the triplet state optically would result in a large reduction in signal compensating for the low transition probability. Direct observation of the transitions from the S_1 state to the triplet and then from the triplet to S_0 are also possible. At high temperatures it may be difficult to observe these as the rate of nonradiative transitions scales exponentially with temperature [56], but it may be possible at cryogenic temperatures.

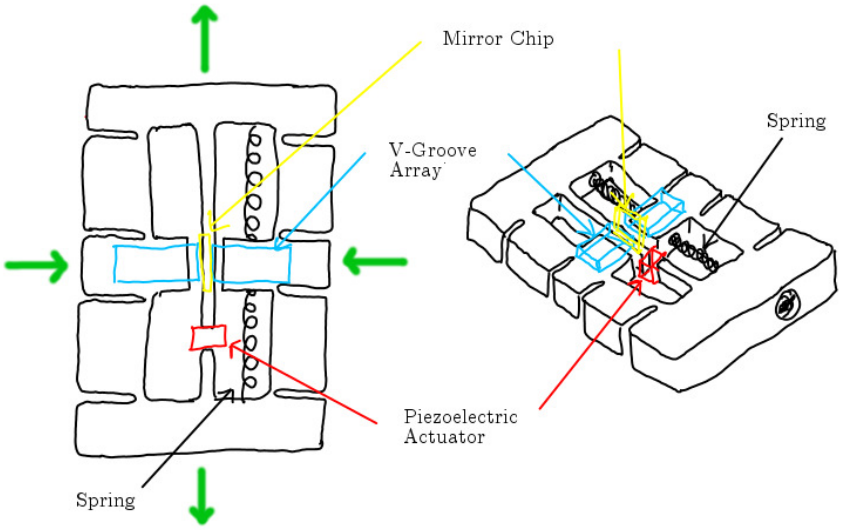


Figure 7.1: A flexure based design for a single cavity. The design uses the amplified motion of a single piezo actuator to scan the cavity length. Details in text.

Looking further forward, we would like eventually to couple different molecules to multiple cavities and be able to tune these multiple molecule-cavity systems into resonance. This will involve the construction of many independently tunable cavities and must also incorporate the ability to tune individual molecules. To this end, we have designed a set of interdigitated electrodes that can be deposited in gold onto the mirror substrates. These electrodes need testing and development so that they can be placed onto the mirror substrates. By applying a voltage to these electrodes we can take advantage of the quadratic Stark tuning coefficient of DBT in anthracene to tune multiple molecules to have the same emission wavelength.

It would be good to have a simpler cavity mounting scheme if we are to have many cavities simultaneously aligned. They must be stable against large temperature changes and should be stiff to suppress vibrations. Other requirements are a large scanning range at cryogenic temperatures and a relatively small size to be able to fit many such cavities into the volume of the cryostat.

A design that tries to fulfil these requirements is seen in figure 7.1. In the left hand figure, when the piezo, shown in red, expands vertically, the top and bottom are pushed apart while the sides come in together. This shortens the distance between the two v-groove arrays, thereby tuning the cavity. The movement is defined by flexures, which are positioned so as to amplify the length change, removing the need for two separate shear piezo stacks. A spring holds the piezo block in place, provides an initial shortening of the central section and removes the hysteresis of any plastic deformation of the material. If the total length of the flexures of the mount are 30 mm and the initial shortening of the spring is 100 μm the mount amplifies the action of the piezo by five times. The mount is

made of invar in order to mitigate against misalignment as the cavity is cooled, which is also helped by the monolithic aspect of the design. The v-groove arrays are fixed to the two lugs in the centre of the mount and aligned using the methods in section 4.3. The design of the flexure is such that the two v-groove arrays only move in a single direction and this simplifies each cavity mount. Because this mount is compact, many cavities could operate independently in the same cyrostat.

The encouraging properties of the DBT molecule, combined with these advances in manipulating their coupling to electromagnetic fields puts single DBT molecules in a strong position to become a practical source of single photons. With further development, we hope to see these molecules becoming a valuable addition to quantum photonic circuits.

Appendices

APPENDIX A

CAVITY OVERLAP INTEGRAL

The spatial overlap of a displaced Gaussian mode with a Hermite-Gaussian mode of order (n, m) is

$$\int_{y=-\infty}^{\infty}\int_{x=-\infty}^{\infty} \frac{2}{\pi}\frac{1}{{w_0}^2\sqrt{1+\frac{c^2}{\left(\frac{\pi {w_0}^2}{\lambda}\right)^2}}}\frac{1}{\sqrt{2^n n!}}H_n\left(\frac{\sqrt{2}x}{w_0}\right)\frac{1}{\sqrt{2^m m!}}H_m\left(\frac{\sqrt{2}y}{w_0}\right) e^{-\frac{x^2+y^2}{{w_0}^2}} e^{-\frac{(x-a)^2+(y-b)^2}{{w_0}^2\left(1+\frac{c^2}{\left(\frac{\pi {w_0}^2}{\lambda}\right)^2}\right)}} dxdy \tag{A.1}$$

the displaced Gaussian has been moved by in x, y and z by a, b and c. w is the beam width at the plane mirror. The integral can be separated

$$\frac{1}{\sqrt{{w_0}^2 c'}}\int_{x=-\infty}^{\infty}\sqrt{\frac{2}{\pi n! 2^n}}H_n\left(\frac{\sqrt{2}x}{w_0}\right)e^{\frac{-(1+c'^2)x^2+2ax-a^2}{{w_0}^2 c'^2}}dx$$
$$\times\frac{1}{\sqrt{{w_0}^2 c'}}\int_{y=-\infty}^{\infty}\sqrt{\frac{2}{\pi m! 2^m}}H_m\left(\frac{\sqrt{2}y}{w_0}\right)e^{\frac{-(1+c'^2)y^2+2by-b^2}{{w_0}^2 c'^2}}dy \tag{A.2}$$

where $c'^2 = 1+\frac{c^2}{\left(\frac{\pi {w_0}^2}{\lambda}\right)^2}$. These integrals can be solved analytically. We will follow the x direction though the same applies for y. A parametrised version of the integral is easier to follow.

$$\frac{1}{\sqrt{{w_0}^2 c'}}\int_{x=-\infty}^{\infty}\sqrt{\frac{2}{\pi n! 2^n}}H_n\left(\frac{\sqrt{2}x}{w_0}\right)e^{-\alpha x^2+\beta x+\gamma}dx \tag{A.3}$$

which can be expressed as

$$\frac{1}{\sqrt{{w_0}^2 c'}} e^{\frac{\beta^2}{4\alpha}+\gamma} \int_{x=-\infty}^{\infty} \sqrt{\frac{2}{\pi n! 2^n}} H_n\left(\frac{\sqrt{2}x}{w_0}\right) e^{-\left(\sqrt{\alpha}x - \frac{\beta}{2\sqrt{\alpha}}\right)^2} dx \tag{A.4}$$

with $\alpha = \frac{1+c'^2}{{w_0}^2 c'^2}$, $\beta = \frac{2a}{{w_0}^2 c'^2}$ and $\gamma = \frac{-a^2}{{w_0}^2 c'^2}$. We also make the substitution $x = \frac{z}{\sqrt{\alpha}} + \frac{\beta}{2\alpha}$ giving

$$= \frac{1}{\sqrt{\alpha {w_0}^2 c'}} e^{\frac{\beta^2}{4\alpha}+\gamma} \int_{z=-\infty}^{\infty} \sqrt{\frac{2}{\pi n! 2^n}} H_n\left(\frac{\sqrt{2}}{w_0}\left(\frac{z}{\sqrt{2\alpha}} + \frac{\beta}{2\alpha}\right)\right) e^{-z^2} dz \tag{A.5}$$

The explicit form of the Hermite polynomials is

$$H_p(\zeta) = p! \sum_{j=0}^{\lfloor p/2 \rfloor} \frac{(-1)^j}{j!(p-2j)!} (2\zeta)^{p-2j} \tag{A.6}$$

which we can use to express the integral as

$$\frac{1}{\sqrt{\alpha {w_0}^2 c'}} e^{\frac{\beta^2}{4\alpha}+\gamma} \int_{z=-\infty}^{\infty} \sqrt{\frac{2n!}{\pi 2^n}} \sum_{j=0}^{\lfloor n/2 \rfloor} \frac{(-1)^j}{j!(n-2j)!} \left(\frac{2\sqrt{2}}{w_0}\left(\frac{z}{\sqrt{\alpha}} + \frac{\beta}{2\alpha}\right)\right)^{n-2j} e^{-z^2} dz \tag{A.7}$$

Now using a binomial expansion to treat $\left(\frac{z}{\sqrt{\alpha}} + \frac{\beta}{2\alpha}\right)$ as a sum of expressions. Also using the fact that

$$\int_{z=-\infty}^{\infty} z^{2k} e^{-z^2} dz = \frac{\sqrt{\pi}(2k-1)!!}{2^k} \tag{A.8}$$

for each value of k, though the integral is only equal to a finite value when the polynomial is an even function. We can now perform the integral, giving the expression.

$$\frac{1}{\sqrt{\alpha {w_0}^2 c'}} e^{\frac{\beta^2}{4\alpha}+\gamma} \sqrt{\frac{2n!}{2^n}} \sum_{j=0}^{\lfloor n/2 \rfloor} \frac{(-1)^j}{j!(n-2j)!} \left(\frac{2\sqrt{2}}{w_0}\right)^{n-2j} \sum_{k=0}^{\lfloor n/2-j \rfloor} \frac{(n-2j)!}{2k!(n-2j-2k)!} \left(\frac{1}{\sqrt{2\alpha}}\right)^{2k} \left(\frac{\beta}{2\alpha}\right)^{n-2j-2k} (2k-1)!! \tag{A.9}$$

Subbing back in the parametrisations we obtain the expression for the value of the overlap integral of a displaced Gaussian with a higher mode of order n in one dimension.

$$\sqrt{\frac{2n!}{2^n}}\sqrt{\frac{c'}{1+c'^2}}e^{-\frac{a^2}{{w_0}^2(1+c'^2)}}\sum_{j=0}^{\lfloor n/2\rfloor}\frac{(-1)^j}{j!(n-2j)!}\left(\frac{2\sqrt{2}}{w_0}\right)^{n-2j}$$
$$\sum_{k=0}^{\lfloor n/2-j\rfloor}\frac{(n-2j)!}{2k!(n-2j-2k)!}\left(\frac{{w_0}^2c'}{2(1+c'^2)}\right)^k\left(\frac{a}{1+c'^2}\right)^{n-2j-2k}(2k-1)!! \tag{A.10}$$

BIBLIOGRAPHY

[1] P. Kok, S. L. Braunstein, and J. P. Dowling, J. Opt. B Quantum Semiclassical Opt **6**, S811 (2004).

[2] N. Gisin and R. Thew, Nat. Photonics **1**, 165 (2007).

[3] J. Y. Cheung, C. J. Chunnilall, E. R. Woolliams, N. P. Fox, J. R. Mountford, J. Wang, and P. J. Thomas, J. Mod. Opt. **54**, 373 (2007).

[4] M. Fox, *Quantum Optics* (Oxford University Press, 2006).

[5] M. Brune, S. Haroche, V. Lefevre, J. M. Raimond, and N. Zagury, Phys. Rev. Lett. **65**, 976 (1990).

[6] G. Nougues, A. Rauschenbeutel, S. Osnaghi, M. Brune, J. M. Raimond, and S. Haroche, Nature **400**, 239 (1999).

[7] C. C. Gerry and P. L. Knight, *Introductory Quantum Optics* (Cambridge University Press, 2005).

[8] H. J. Kimble, M. Dagenais, and L. Mandel, Phys. Rev. Lett. **39**, 691 (1977).

[9] F. Diedrich and H. Walther, Phys. Rev. Lett. **58**, 203 (1987).

[10] D. C. Burnham and D. L. Weinberg, Phys. Rev. Lett. **25**, 84 (1970).

[11] C. K. Hong and L. Mandel, Phys. Rev. Lett. **56**, 58 (1986).

[12] T. B. Pittman, B. C. Jacobs, and J. D. Franson, Phys. Rev. A **66**, 042303 (2002).

[13] F. Kaneda, B. G. Christensen, J. J. Wong, K. T. McCusker, H. S. Park, and P. G. Kwiat, "A time-multiplexed heralded single-photon source," (2015), arXiv.

[14] E. A. Goldschmidt, M. D. Eisaman, J. Fan, S. V. Polyakov, and A. Migdall, Phys. Rev. A **78**, 013844 (2008).

[15] A. S. Clark, C. Husko, M. J. Collins, G. Lehoucq, S. Xavier, A. D. R. S. Combrié, C. Xiong, and B. J. Eggleton, Opt. Lett. **38**, 649 (2013).

[16] M. Trupke, E. A. Hinds, S. Eriksson, E. A. Curtis, Z. Moktadir, E. Kukharenke, and M. Kraft, Appl. Phys. Lett. **87**, 211106 (2005).

[17] M. Trupke, J. Goldwin, and B. Darquié, Phys. Rev. Lett. **99**, 1 (2007).

[18] J. Goldwin, M. Trupke, J. Kenner, and A. Raptnapala, Nat. Commun. **2**, 418 (2011).

[19] M. Hijlkema, B. Weber, H. P. Specht, S. C. Webster, and A. Kuhn, Nature Physics **3**, 253 (2007).

[20] P. Michler, A. Kiraz, C. Becher, W. V. Schoenfeld, P. M. Petroff, L. Zhang, E. Hu, and A. Imamoglu, Science **290**, 2282 (2000).

[21] A. Laucht, S. Pütz, T. Günthner, N. Hauke, R. Saive, S. Frédérick, M. Bichler, M.-C. Amann, A. W. Holleitner, M. Kaniber, and J. J. Finley, Phys. Rev. X **2**, 011014 (2012).

[22] Z. Yuan, B. E. Kardynal, R. M. Stevenson, A. J. Shields, C. J. Lobo, K. Copper, N. S. Beattie, D. A. Ritchie, and M. Pepper, Science **295**, 102 (2002).

[23] C. Santori, D. Fatta, J. Vučković, G. S. Solomon, and Y. Yamamoto, Nature **419**, 594 (2002).

[24] Y.-M. He, Y. He, Y.-J. Wei, D. Wu, M. Atatüre, C. Schnieder, S. Höfling, M. Kamp, C.-Y. Lu, and J.-W. Pan, Nat. Nanotechnol. **8**, 213 (2013).

[25] N. Akopian, N. H. Lindner, E. Poem, Y. Berlatzky, J. Avron, D. Gershoni, B. D. Gerardot, and P. M. Petroff, Phys. Rev. Lett. **96**, 130501 (2006).

[26] A. J. Bennett, D. C. Unitt, D. A. Ritchie, and A. J. Shields, Opt. Express **13**, 50 (2005).

[27] A. Muller, E. B. Flagg, M. Metcalfe, J. Lawall, and G. S. Solomon, Appl. Phys. Lett. **95**, 1 (2009).

[28] R. Kolesov, K. Xia, R. Rueter, R. Stöhr, A. Zappe, J. Meijer, P. R. Hemmer, and J. Wrachtrup, Nat. Comm. **3**, 1029 (2012).

[29] A. Gruber, A. Dräbenstedt, C. Tietz, J. Wrachtrup, and C. von Borczyskowski, Science **276**, 2012 (1997).

[30] F. Jelezko, T. Gaebel, I. Popa, A. Gruber, and J. Wrachtrup, Phys. Rev. Lett. **92**, 7 (2004).

[31] M. W. Doherty, N. B. Manson, P. Delaney, F. Jelezko, J. Wrachtrup, and L. C. L. Hollenberg, Phys. Rep. **528**, 1 (2013).

[32] A. Faraon, P. E. Barclay, C. Santori, K.-M. Fu, and R. G. Beausoleil, Nature Photon. **5**, 301 (2011).

[33] K.-M. Fu, C. Santori, P. E. Barclay, L. J. Rogers, N. B. Manson, and R. G. Beausoleil, Phys. Rev. Lett. **103**, 256404 (2009).

[34] A. Beveratos, R. Brouri, T. Gacoin, J.-P. Poizat, and P. Grangier, Phys. Rev. A **64**, 061802 (2001).

[35] P. E. Barclay, K.-M. C. Fu, C. Santori, and R. G. Beausoleil, Appl. Phys. Lett. **95**, 1 (2009).

[36] R. Albrecht, A. Bommer, C. Deutsch, J. Reichel, and C. Becher, Phys. Rev. Lett. **110**, 1 (2013).

[37] E. Neu, D. Steinmetz, J. Reidrich-Möller, S. Gsell, M. Fischer, M. Schreck, and C. Becher, New J. Phys **13**, 025012 (2011).

[38] U. Jantzen, A. B. Kurz, D. S. Rudnicki, C. Schäfermeier, K. D. Jahnke, U. L. Andersen, V. A. Davydov, V. N. Agafonov, A. Kubanek, L. J. Rogers, and F. Jelezko, arXiv:1602.03391v1 , (2016).

[39] S. Castellettol, B. C. Johnson, V. Ivády, N. Stavrias, T. Umeda, A. Gali, and T. Ohshima, Nat. Mater. **13**, 151 (2013).

[40] W. E. Moerner and L. Kador, Phys. Rev. Lett. **62**, 2535 (1989).

[41] M. Orrit and J. Bernard, Phys. Rev. Lett. **65**, 2716 (1990).

[42] W. P. Ambrose, T. Basché, and W. E. Moerner, J. Chem. Phys. **95**, 7150 (1991).

[43] S. Kummer, T. Basché, and C. Bräuchle, Chem. Phys. Lett. **229**, 309 (1994).

[44] F. B. Zhelezko, I. M. Gulis, B. Lounis, and M. Orrit, J. Appl. Spectrosc. **66**, 344 (1999).

[45] F. Jelezko, P. Tamarat, B. Lounis, and M. Orrit, J. Phys. Chem. **100**, 13892 (1996).

[46] T. Plakhotnik, W. E. Moerner, V. Palm, and U. P. Wild, Opt. Commun. **114**, 83 (1995).

[47] S. Faez, N. R. Verhart, M. Markoulides, F. Buda, A. Gourdon, and M. Orrit, Faraday Discuss. , (2015).

[48] C. Brunel, B. Lounis, P. Tamarat, and M. Orrit, Phys. Rev. Lett. **83**, 2722 (1999).

[49] B. Lounis and W. E. Moerner, Nature **407**, 491 (2000).

[50] C. Toninelli, Y. Delley, T. Stöferle, A. Renn, S. Götzinger, and V. Sandoghdar, Appl. Phys. Lett. **97**, 021107 (2010).

[51] I. Gerhardt, G. Wrigge, P. Bushev, G. Zumofen, M. Agion, R. Pfab, and V. Sandhogdar, Phys. Rev. Lett. **98**, 033601 (2007).

[52] M. Pototschnig, Y. Cahssagnuex, J. Hwang, G. Zumofen, and A. R. adn V. Sandoghdar, Phys. Rev. Lett. **107**, 063001 (2011).

[53] S. Faez, P. Türschmann, H. R. Haakh, S. Götzinger, and V. Sandoghdar, Phys. Rev. Lett. **113**, 213601 (2014).

[54] J. Hwang and E. A. Hinds, New J. Phys. **13**, 085009 (2011).

[55] A. A. L. Nicolet, C. Hofmann, M. A. Kol'chenko, B. Kozankiewicz, and M. Orrit, Chem. Phys. Chem. **8**, 1215 (2007).

[56] A. Köhler and H. Bässler, Mater. Sci. Eng. **66**, 71 (2009).

[57] M. Nothaft, S. Höhla, F. Jelezko, J. Pflaum, and J. Wrachtrup, Phys. Status Solidi B **249**, 661 (2012).

[58] P. Siyshev, G. Stein, J. Wrachtrup, and I. Gerhardt, Nat. Lett. **509**, 66 (2014).

[59] C. Hofmann, A. Nicolet, M. A. Kol'chenko, and M. Orrit, Chem. Phys. **318**, 1 (2005).

[60] A. A. L. Nicolet, P. Bordat, C. Hofmann, M. A. Kol'chenko, B. Kozankiewicz, R. Brown, and M. Orrit, Chem. Phys. Chem. **8**, 1929 (2007).

[61] E. M. Purcell, Proc. Am. Phys. Soc. **69**, 681 (1946).

[62] J. P. G. adn H. J. Zeiger and C. H. Townes, Phys. Rev. **99**, 1264 (1955).

[63] T. H. Maiman, Nature **187**, 493 (1960).

[64] E. T. Jaynes and F. W. Cummings, Proc. of IEEE **51**, 89 (1963).

[65] P. Goy, J. M. Raimond, M. Gross, and S. Haroche, Phys. Rev. Lett. **50**, 1903 (1983).

[66] R. G. Hulet and E. S. H. adn Daniel Kleppner, Phys. Rev. Lett. **55**, 2137 (1985).

[67] W. Jhe, A. Anderson, E. A. Hinds, D. Meschede, and L. Moi, Phys. Rev. Lett. **58**, 666 (1987).

[68] E. A. Hinds, Adv. At. Mol. Opt. Phy. **28**, 237 (1990).

[69] K. J. Vahala, Nature **424**, 839 (2003).

[70] J. M. Gérard, B. Sermage, B. Gayral, B. Legrand, E. Costard, and V. Thierry-Mieg, Phys. Rev. Lett. **81**, 1110 (1998).

[71] E. Peter, P. Senellart, D. Martrou, A. Lemaître, J. Hours, J. M. Gé, and J. Bloch, Phys. Rev. Lett. **95**, 067401 (2005).

[72] H.-G. Franck and J. W. Stadelhofer, *Industrial Aromatic Chemistry* (Springer-Verlag, 1988).

[73] S. Portmann and H. P. Lüthi, CHIMIA International Journal for Chemistry **54**, 766 (2000).

[74] I. Deperasińska, E. Karpiuk, M. Banasiewicz, and B. Kozankiewicz, Chem. Phys. Lett. **492**, 93 (2010).

[75] F. Neese, Wiley Interdisciplinary Reviews: Computational Molecular Science **2**, 73 (2012).

[76] W. Koch and M. C. Holthausen, *A Chemist's Guide to Density Functional Theory* (Wiley-VCH, 2002).

[77] A. D. Becke, J. Chem. Phys. **98**, 5648 (1993).

[78] F. Neese, F. Wennmohs, A. Hansen, and U. Becker, Chem. Phys. **356**, 98 (2009).

[79] F. Weigend and R. Ahlrichs, Phys. Chem. Chem. Phys. **7**, 3297 (2005).

[80] J. R. Hill, E. L. Chronister, T.-C. Chang, H. Kim, J. C. Postlewaite, and D. D. Dlott, J. Chem. Phys. **88**, 949 (1988).

[81] A. Makarewicz, I. Deperasińska, E. Karpiuk, J. Nowacki, and B. Kosankiewicz, Chem. Phys. Lett. **535**, 140 (2012).

[82] J. B. Trebbia, H. Ruf, P. Tamarat, and B. Lounis, Opt. Ex. **17**, 23986 (2009).

[83] W. H. Hesselink and D. Wiersma, J. Chem. Phys. **73**, 648 (1980).

[84] T. Basché, W. E. Moerner, M. Orrit, and U. P. Wild, *Single-Molecule Optical Detection Imaging and Spectroscopy* (VCH, 1996).

[85] M. Schwoerer and H. C. Wolf, *Organic Molecular Solids* (Wiley-VCH, 2007).

[86] A. N. Aleshin, J. Y. Lee, S. W. Chu, J. S. Kim, and Y. W. Park, App. Phys. Lett. **84**, 5383 (2004).

[87] W. Peticolas, J. P. Goldsborough, and K. E. Rieckhoff, Phys. Rev. Lett. **10**, 43 (1963).

[88] G. C. Smith, Phys. Rev. **166**, 839 (1968).

[89] J. N. Sherwood and S. J. Thompson, J. Sci. Instrum. **37**, 242 (1960).

[90] R. B. Campbell, J. M. Robertson, and J. Trotter, Acta Crystallographica **15**, 289 (1962).

[91] R. F. P. Grimbergen, M. F. Reedijk, H. Meekes, and P. Bennema, J. Phys. Chem. B **102**, 2646 (1998).

[92] A. I. Kitaigorodsky and N. A. Ahmed, Acta Cryst. **28**, 207 (1972).

[93] I. Nakada, J. Phys. Soc. Jap. **17**, 113 (1961).

[94] A. R. Elsharkawi and K. C. Kao, J. Opt. Soc. Am. **65**, 1269 (1975).

[95] Y. Tian, P. Navarro, and M. Orrit, Phys. Rev. Lett. **113**, 135505 (2014).

[96] R. Lettow, Y. L. A. Rezus, A. Renn, G. Zumofen, E. Ikonen, S. Götzinger, and V. Sandoghdar, Phys. Rev. Lett. **104**, 1 (2010).

[97] T. Plakhtonik, E. A. Donley, and U. P. Wild, Annu. Rev. Phys. Chem. **48**, 181 (1997).

[98] A. Sumbusch, L. Fleury, R. Brown, J. Bernard, and M. Orrit, Phys. Rev. Lett. **70**, 3584 (1993).

[99] I. Sunagawa, *Crystal Growth* (Cambridge University Press, 2005).

[100] D. T. J. Hurle, *Handbook of Crystal Growth 1: Fundamentals* (North-Holland, 1993).

[101] R. F. Lipsett, Can. J. Phys. **35**, 284 (1957).

[102] P. W. Bridgman, Proceedings of the American Academy of Arts and Sciences **60**, 305 (1925).

[103] C. Toninelli, K. Early, J. Bremi, A. Renn, S. Götzinger, and V. Sandoghdar, Opt. Ex. **18**, 6577 (2010).

[104] R. L. Headrick, H. Zhou, B. Wang, Y. Wang, G. P. Carpenter, A. C. Mayer, M. Lloyd, and G. G. Malliaras, arXiv:1107.3277v1 [cond-mat.mtrl-sci] , (2011).

[105] N. Karl, *Crystal Growth, Properties and Applications* (Berlin: Springer-Verlag, 1980).

[106] R. A. Laudise, C. Kloc, P. G. Simpkins, and T. Siegrist, J. Cryst. Growth **187**, 449 (1998).

[107] A. R. McGhie, A. M. Voshchenkov, P. J. Reucroft, and M. M. Labes, J. Chem. Phys. **48**, 186 (1968).

[108] B. Marciniak and V. Pavlyuk, Molecular Crystals and Liquid Crystals **373**, 237 (2002).

[109] G. Sears and E. R. Hopke, J. Am. Chem. Soc. **71**, 1632 (1949).

[110] B. Stevens, J. Chem. Soc. , 2973 (1953).

[111] J. D. Kelley and F. O. Rice, J. Phys. Chem. **68**, 3794 (1964).

[112] B. F. Rordorf, Chemosphere **15**, 1325 (1986).

[113] P. C. Hansen and C. A. Eckert, J. Chem. Eng. Data **31**, 1 (1986).

[114] V. Oja and E. M. Suuberg, J. Chem. Eng. Data **43**, 486 (1998).

[115] X. Chen, V. Oja, W. G. Chan, and M. R. Hajaligol, J. Chem. Eng. Data **51**, 386 (2006).

[116] C. L. Yaws, *Yaws Handbook of Antoine Coefficients for Vapor Pressure 2nd Electronic Edition* (Knovel, 2009).

[117] C. J. Adkins, *Equilibrium Thermodynamics* (McGraw Hill Book Company, 1968).

[118] D. A. Hinckley, T. F. Bidleman, and W. T. Foreman, J. Chem. Eng. Data **35**, 232 (1990).

[119] M. Randić, J. Am. Chem. Soc. **97**, 6609 (1975).

[120] C. M. White, J. Chem. Eng. Data **31**, 198 (1986).

[121] M. V. Roux, M. Temprado, J. S. Chickos, and Y. Nagano, J. Chem. Ref. Data **37**, 1855 (2008).

[122] U. United States Environmental Protection Agency (Washington DC, "Estimation programs interface suite™for microsoft®windows, v 4.11," `http://www.epa.gov/oppt/exposure/pubs/episuitedl.htm` (2012).

[123] S. E. Stein and R. L. Brown, J. Chem. Inf. Comput. Sci. **34**, 581 (1994).

[124] M. M. Rauhut, B. G. Roberts, D. R. Maulding, W. Bergmark, and R. Coleman, J. Org. Chem. **40**, 330 (1974).

[125] B. Moller, J. Rarey, and D. Ramjugernath, J. Mol. Liq. **143**, 52 (2008).

[126] Y. Nannoolal, J. Rarey, D. Ramjugernath, and W. Cordes, Fluid Phase Equilibria **226**, 45 (2004).

[127] K. D. Major, Y.-H. Lien, C. Polisseni, S. Grandi, K. W. Kho, A. S. Clark, J. Hwang, and E. A. Hinds, Rev. Sci. Instrum. **86**, 083106 (2015).

[128] C. B. Walsh and E. I. Franses, Thin Solid Films **429**, 71 (2003).

[129] R. H. Stolen and C. Lee, J. Opt. Soc. Am. B **1**, 652 (1984).

[130] W. M. Haynes, D. R. Lide, and T. J. Bruno, eds., *CRC Handbook of Chemistry and Physics*, 93rd ed. (CRC Press, 2012).

[131] H. L. Bhat, *An Introduction Crystal Growth Principles and Practice* (CRC Press, 2015).

[132] S. Jo, hitoshi Yoshikawa, A. Fujii, and M. Takenaga, App. Surf. Sci. **252**, 3514 (2006).

[133] H. de Vries and D. A. Wiersma, J. Chem. Phys. **72**, 1851 (1980).

[134] H. de Vries and D. A., J. Chem. Phys. **70**, 5807 (1979).

[135] J. Bernard, L. Fleury, H. Talon, and M. Orrit, J. Chem Phys **98**, 850 (1993).

[136] S. Eriksson, M. Trupke, H. F. Powell, D. Sahagun, C. D. J. Sinclair, E. A. Curtis, B. E. Sauer, E. A. Hinds, Z. Moktadir, C. O. Gollasch, and M. Kraft, Eur. Phys. J. D. **35**, 135 (2005).

[137] M. Trupke, *Microcavities for atom chips*, Ph.D. thesis, Imperial College London (2007).

[138] A. E. Siegman, *Lasers* (University Science Books, 1986).

[139] Z. Moktadir, E. Koukharenka, M. Kraft, D. M. Bagnall, H. Powell, M. Jones, and E. A. Hinds, J. Micromech. Microeng. **14**, S82 (2004).

[140] K. E. Bean, IEEE Trans. Electron Dev. **25**, 1185 (1978).

[141] A. M. Huntz, L. Maréchal, B. Lesage, and R. Molins, Appl. Surf. Sci. **252**, 7781 (2006).

[142] K. V. K. Rao, S. V. N. Naidu, and L. Iyengar, J. Am. Ceram. Soc. **53**, 124 (1970).

[143] H. Benisty, R. Stanley, and M. Mayer, JOSA A **15**, 1192 (1998).

[144] G. Beidermann, F. M. Benito, K. M. Fortier, D. L. Stick, T. K. Lloyd, P. D. D. Schwindt, C. Y. Nakakura, J. R. L. Jarecki, and M. G. Blain, App. Phys. Lett. **97**, 1 (2010).

[145] A. B. Klimov and S. M. Chumakov, *A Group-Theoretical Approach to Quantum Optics* (Wiley-VCH, 2009).

[146] P. Lambropoulos and D. Petrosyan, *Fundamentals of Quantum Optics and Quantum Information* (Springer-Verlag Berlin Heildelberg, 2007).

[147] P. de Vries and A. Lagendijk, Phys. Rev. Lett. **81**, 1381 (1998).

[148] H. J. Carmichael, *Statistical Methods in Quantum Optics vol I: Master Equations and Fokker-Planck Equations* (Springer-Verlag Berlin Heidelberg, 2008).

[149] S. M. Dutra, *Cavity Quantum Electrodynamics* (Wiley-Interscience, 2005).

[150] E. J. Putzer, Amer. Math. Monthly **73**, 2 (1966).

[151] H. J. Carmichael, *Statistical Methods in Quantum Optics vol II: Non-Classical Fields* (Springer-Verlag Berlin Heidelberg, 2008).

[152] C. Polisseni, K. D. Major, S. Boissier, S. Grandi, A. S. Clark, and E. A. Hinds, arXiv:1602.01277v1 , (2015).

[153] E. Kwon, H. Oikawa, H. Kasai, and H. Nakanishi, Cryst. Growth Des. **7**, 600 (2007).

[154] P. Grančič, R. Bylsma, H. Meekes, and H. M. Cuppen, Cryst. Growth Des. **15**, 1625 (2015).